AGU ADVANCING EARTH AND SPACE SCIENCE

Tectonics

RESEARCH ARTICLE
10.1029/2020TC006503

Key Points:

- The western North China craton records at least three orogenies from the Paleoproterozoic to the early Paleozoic
- Mesoproterozoic strata in North China, Tarim, and the Qilian Shan are similar, suggesting continuity among these continents
- Gondwana was not affixed to the western margin of North China in the Neoproterozoic-early Paleozoic

Supporting Information:

- Supporting Information S1

Correspondence to:

C. Wu and A. V. Zuza,
wuchen@itpcas.ac.cn;
wuchenlovegeology@gmail.com;
azuza@unr.edu;
avz5818@gmail.com

Citation:

Wu, C., Zuza, A. V., Yin, A., Chen, X., Haproff, P. J., Li, J., et al. (2021). Punctuated orogeny during the assembly of Asia: Tectonostratigraphic evolution of the North China craton and the Qilian Shan from the Paleoproterozoic to early Paleozoic. *Tectonics*, *40*, e2020TC006503. https://doi.org/10.1029/2020TC006503

Received 29 AUG 2020
Accepted 1 FEB 2021

Punctuated Orogeny During the Assembly of Asia: Tectonostratigraphic Evolution of the North China Craton and the Qilian Shan From the Paleoproterozoic to Early Paleozoic

Chen Wu[1], Andrew V. Zuza[2], An Yin[3], Xuanhua Chen[4], Peter J. Haproff[5], Jie Li[6], Bing Li[2,4], and Lin Ding[1,7]

[1]Key Laboratory of Continental Collision and Plateau Uplift, Institute of Tibetan Plateau Research, and Center for Excellence in Tibetan Plateau Earth Sciences, Chinese Academy of Sciences, Beijing, China, [2]Nevada Bureau of Mines and Geology, University of Nevada, Reno, NV, USA, [3]Department of Earth, Planetary and Space Sciences, University of California, Los Angeles, CA, USA, [4]Chinese Academy of Geological Sciences, Beijing, China, [5]Department of Earth and Ocean Sciences, University of North Carolina, Wilmington, NC, USA, [6]School of Earth Sciences and Resources, China University of Geosciences (Beijing), Beijing, China, [7]University of Chinese Academy of Sciences, Beijing, China

Abstract The Proterozoic-Phanerozoic evolution of the Tarim and North China cratons is integral to the construction of the Eurasian continent. Throughout the Paleozoic, these continents were bound by the Paleo-Asian and Tethyan Oceans to the north and south, respectively, and, thus, their paleogeography is critical to reconstructions of the oceanic domains. Specifically, it remains uncertain whether the Tarim and North China cratons were contiguous during the Paleozoic. Geologic observations from the Qilian Shan and Longshou Shan of western China provide valuable information regarding the paleotectonic relationships of these continents. Here we present detailed field, geochronological, and geochemical observations from key locations in the Qilian Shan and Longshou Shan to decipher complex relationships between the Kunlun-Qaidam, North China, and Tarim continents. Paleoproterozoic deformation might have been associated with the northern North China orogen, whereas a Neoproterozoic collisional orogen occurred between the Kunlun-Qaidam-South Tarim and the North China-North Tarim. Subsequent late Neoproterozoic rifting led to the opening of the Qilian ocean as an embayed marginal sea, and the Paleo-Asian Ocean developed along the northern margin of the North China craton. South-dipping subduction, arc magmatism, slab rollback, and convergence between Kunlun-Qaidam and North China continued throughout the Early Silurian, which were recorded in the Qilian Shan and Longshou Shan regions. Our updated geotectonic framework requires reevaluation of previously published paleogeographic models, including ones that suggest the North China craton was affixed to Gondwana in the early Paleozoic. It is further considered a possible connection between the North China and southern Africa at ca. 2.05 Ga.

1. Introduction

The assembling of the Eurasian continent occurred from the Proterozoic to the Mesozoic over a time span of nearly one billion years (Scotese & McKerrow, 1990; Şengör & Natal'in, 1996; Sone & Metcalfe, 2008; Yin & Nie, 1996). It was accomplished primarily by the closure of the Paleo-Asian and Tethyan ocean systems, involving cratonal blocks separated from the supercontinents Columbia, Rodinia, and Pangea (e.g., Badarch et al., 2002; Biske & Seltmann, 2010; Heubeck, 2001; Kusky et al., 2007; S. Li et al., 2018; Rogers & Santosh, 2002; Şengör & Natal'in, 1996; Stampfli & Borel, 2002; C. Wu et al., 2016a; Yin & Nie, 1996; G. C. Zhao et al., 2018; Zonenshain et al., 1990; Zuza & Yin, 2017) (Figure 1). The Paleo-Asian and the Tethyan oceanic domains are separated by the Tarim and North China cratons whose geologic histories are critical for deciphering the interactions of the two orogenic systems to the north and south. A major obstacle for establishing the geologic history of Tarim and North China cratons is that the two tectonic entities are currently bounded by Cenozoic structures along the southern margin of the Tian Shan and the northern margin of the Tibetan plateau (Figure 1). These structures have either reactivated or strongly modified the earlier tectonic configurations of the region (e.g., Yin & Nie, 1996). For example, Cenozoic structures that bound the southern margin of Tarim and North China cratons overprinted Mesozoic extensional basins (X. Chen et al., 2003; Vincent & Allen, 1999), an early Paleozoic arc-continent collision system (e.g., S. Song

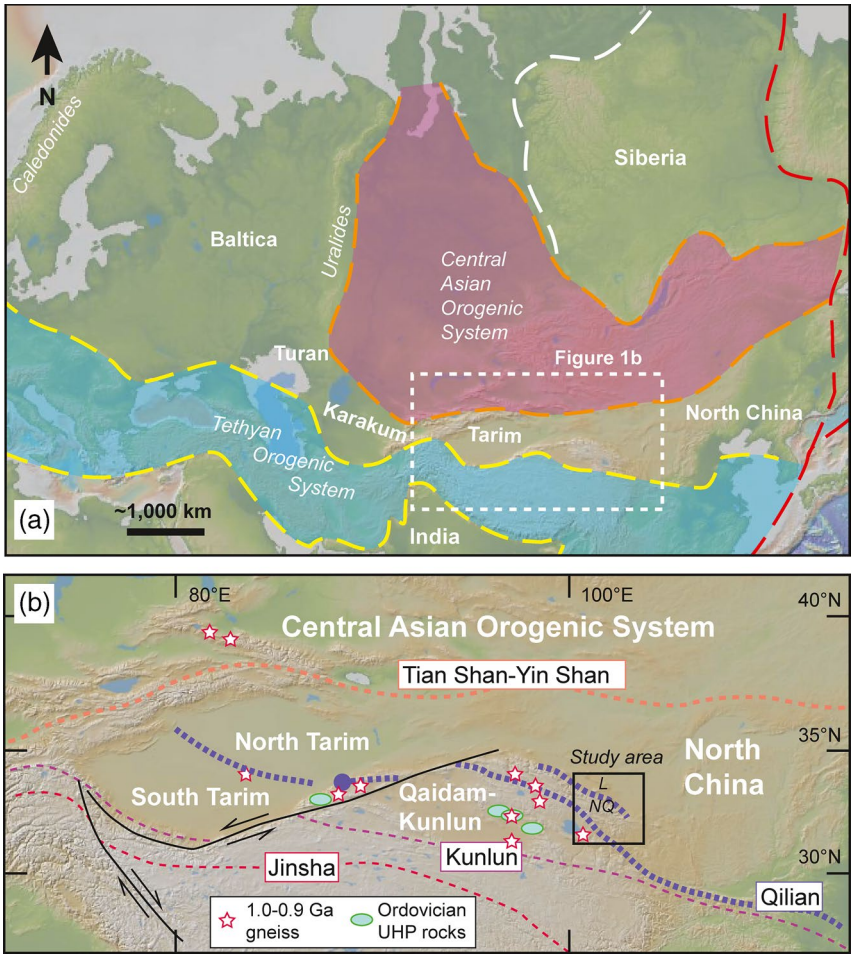

Figure 1. Overview of the Proterozoic-Paleozoic geology of northern Tibet and Central Asia. (a) Tectonic map of Eurasia showing cratons, orogenic systems, and the location of Figure 1b. (b) Configuration of the Jinsha, Kunlun, Qilian, and Tian Shan-Yin Shan suture zones, from north to south respectively, in northern Tibet and central Asia. Also shown are the locations of Neoproterozoic granitoid and gneiss rocks, and Ordovician UHP rocks (e.g., S. Song et al., 2014; C. Wu et al., 2016a). The study area of this work, Longshou Shan (*L*), and North Qilian Shan (*NQ*) are marked. Figures modified from Wu et al. (2016a).

et al., 2013; C. Wu et al., 2017; Xiao et al., 2009; Yin et al., 2007; A. V. Zuza et al., 2018), an enigmatic Neoproterozoic magmatic belt (e.g., Cowgill et al., 2003; G. E. Gehrels et al., 2003a, 2003b; Z. J. Guo et al., 2005; C. Wu et al., 2016a, 2017), and Archean-Proterozoic metamorphic basement rocks of North China craton and the Kunlun-Qaidam continent (Tseng et al., 2006; K. Tung et al., 2007; C. Wu et al., 2017).

Because of the complex geologic histories along the margins of Tarim and North China cratons and the nearby Kunlun-Qaidam continent, it remains unclear how the three ancient cratons, all having Neoproterozoic to Cambrian cover sequences, were related in the paleogeographic reconstructions prior to the appearance of the Paleo-Asian and Tethyan Ocean systems (Figure 2) (C. Wu et al., 2016a). This uncertainty is exemplified by the two competing models for the paleogeographic reconstruction of North China craton in the Cambrian. According to McKenzie et al. (2011) and updated publications (e.g., Y. Han et al., 2016; Myrow et al., 2015), the North China craton was positioned with its southern margin against Gondwana (i.e., contiguous Australia and India). In contrast, the predominant models for the tectonic evolution of the northern Tibetan plateau placed the current southern margin of North China craton against the Kunlun-Qaidam continent, which were separated by a Neoproterozoic-Cambrian ocean (i.e., the Qilian Ocean) that later closed in the Silurian (G. E. Gehrels et al., 2003a, 2003b; Sobel & Arnaud, 1999; S. Song et al., 2013; Yin & Nie, 1996).

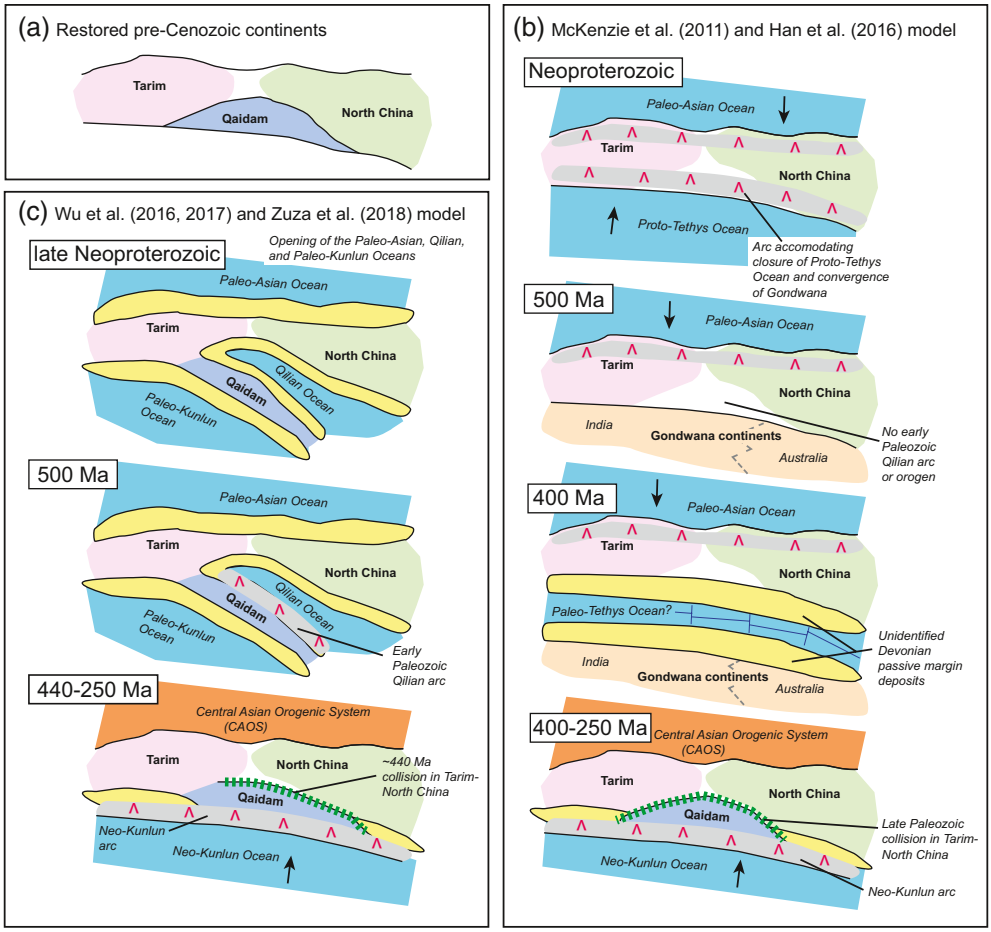

Figure 2. Major tectonic models for the Neoproterozoic-Paleozoic evolution of the Tarim-North China and Kunlun-Qaidam systems. (a) Schematic configuration of northern Tibet after restoring Cenozoic deformation in the Qilian Shan and Pamir thrust systems and left-slip faulting on the Altyn Tagh (e.g., Cowgill et al., 2003; Zuza et al., 2016). (b) Paleogeographic reconstruction of McKenzie et al. (2011) and Han et al. (2016) which positions Gondwana to the south of Tarim and North China in the Cambrian. Shortcomings of this model based on the observed regional geology include: (1) there is no space in the early Paleozoic for the Kunlun-Qaidam continent to collided against the southern margin of the Tarim and North China cratons. (2) Requires unidentified Devonian rifting to remove Gondwana and post-Devonian Qilian orogen, (3) suggests that the Paleo Asian ocean here was open north of North China prior to the Mesoproterozoic. What are our Neoproterozoic passive margin rocks representing? Note that there is no space in the early Paleozoic for the Kunlun-Qaidam continent to collide against the southern margin of the Tarim and North China cratons. This model also requires currently unidentified Devonian passive margins to develop as Gondwana rifts and separates from Tarim-North China. (c) Reconstruction envisioned by Wu et al. (2016a) and Zuza et al. (2017) where the Kunlun-Qaidam continent separates from the southern margin of North China in the Neoproterozoic as peninsular, still connected to Tarim. Counter-clockwise rotation of this continent in the Cambrian-Ordovician, accommodated by southward subduction along the northern margin of Kunlun-Qaidam, leads to the closure of the Qilian Ocean by ~445 Ma.

The Kunlun-Qaidam continent is truncated in the west by the Cenozoic Altyn Tagh fault that has accommodated >500-km left-slip motion (e.g., Cowgill et al., 2003; Peltzer & Tapponnier, 1988). The relationship implies that the microcontinent may have an extended portion to the west currently buried below the Taklimakan desert of Tarim (e.g., C. Wu, Yin et al., 2016; Wu, Zuza et al., 2017; Yin, Dang et al., 2007; Yin, Manning et al., 2007; Zuza et al., 2018). Except two reconnaissance studies (Z. J. Guo et al., 2005; A. Yin & Nie, 1996), the impact of the westward extent of the Kunlun-Qaidam continent west of the Altyn Tagh fault for reconstructions of the Tarim and North China cratons has yet been fully addressed. In this contribution, we explore this issue by examining the tectonostratigraphic relationship along the southern margin of North China craton and northern margin of the Kunlun-Qaidam continent in the Qilian Shan and

Longshou Shan regions (Figure 1). Our research involves geologic mapping, U-Pb magmatic-zircon and detrital-zircon geochronology, and whole-rock geochemistry. Due to the large extent of our study area, which has a north-south length of ~350 km and east-west length of ~250 km (Figure 1), we present site-specific geologic maps of critical areas, together with the details of our structural analysis and analytical results. Our findings contribute to a new understanding of the role of North China craton and Kunlun-Qaidam continent in the evolution of the Paleo-Asian oceans and their possible positions during supercontinent cycles in Earth's history.

2. Regional Geology

2.1. North China Craton

The North China craton is bounded to the southwest by the early Paleozoic Qilian and Qinling orogen, to the north by the late Paleozoic Central Asian Orogenic System (CAOS), and to the south by the Mesozoic Qinling-Dabie Shan orogen (Figure 1). The craton is composed of several Archean-Paleoproterozoic blocks (with predominately ca. 2.5 and 1.95–1.80 Ga ages), and the nature of these individual continents and how/when they coalesced is a fiercely debated topic (e.g., Faure et al., 2007; Kröner et al., 2005; Kusky & Li, 2003; Kusky et al., 2016; L. L. Xiao et al., 2011; Polat et al., 2005; Trap et al., 2007; J. P. Wang et al., 2017, 2019; C. Wu et al., 2018; G. C. Zhao & Cawood, 2012; G. C. Zhao et al., 2001, 2005 and many others). The Mesoproterozoic–Neoproterozoic history of North China craton is best recorded through the deposition of the Changcheng Group (1.80–1.60 Ga), Jixian Group (1.60–1.40 Ga), a currently unnamed unit at 1.40–1.0 Ga, and Qingbaikou Group (1.0–0.80 Ga) in the northern part of North China craton (e.g., J. F. Sun et al., 2012; Y. Wan et al., 2011). Although absent across most of North China craton, Neoproterozoic (i.e., 850–550 Ma) strata occur sporadically along its southern (S. Xiao et al., 2014) and southeastern (Chang, 1980; C. L. Zhang et al., 2006) margins. Neoproterozoic intrusive rocks have been reported across the North China craton, which are correlative in age with rift-related rocks in southern Qaidam (e.g., Dan et al., 2014; X. H. Li et al., 2005; S. Liu et al., 2012; P. Peng et al., 2011; X. L. Wang et al., 2011, 2012; C. Wu, Yin et al., 2016; Wu, Zuza et al., 2017; H. F. Zhang et al., 2009). North China craton was surrounded to the north and south by open oceans (i.e., the Paleo-Asian and Paleo-Tethys Oceans, respectively) and corresponding passive margins. The passive-margin and cratonal sequences were strongly deformed along the cratonal margins during the closure of the ocean systems to the north and south from the late Paleozoic to the early Mesozoic (e.g., Dong et al., 2013; Eizenhöfer et al., 2014; Hacker, Ratschbacher, & Liou, 2004; Hacker, Wallis, et al., 2006; Ratschbacher et al., 2003; W. Xiao et al., 2003; W. J. Xiao, Windley, Huang, et al., 2009b; W. Xiao, Windley et al., 2009c; Yin & Nie, , 1996; Wu, Liu et al., 2016, Wu, Zuza et al., 2017; Zhang, 1997; Zhao & Coe, 1987; cf. Jian et al., 2016).

2.2. Tarim Craton

The Tarim craton consists of the North Tarim and South Tarim blocks that were joined in the Proterozoic (e.g., Ge et al., 2014; Z. J. Guo et al., 2005; C. Wang et al., 2015; Z. Q. Xu et al., 2013; H. Yang et al., 2018; F. Q. Zhang et al., 2019; A. V. Zuza & Yin, 2017). The geometry and age of this collision is debated due to the poor exposure of this orogen under the 10+ km thick Mesozoic-Cenozoic sediments of the Tarim Basin (e.g., X. Chen et al., 2003; Z. J. Guo et al., 2005). Our preferred model involves a Neoproterozoic collision between the continents, which links this event with the widespread ca. 1.0–0.9 Ga arc plutons that are observed from the Qilian Shan northwest to the Tian Shan and the Neoproterozoic Aksu suture in the northwest Tarim Basin (e.g., Z. J. Guo et al., 2005; C. Wu et al., 2016a, 2017; A. V. Zuza & Yin, 2017). Other authors have suggested that this collision occurred in the Paleoproterozoic time (e.g., H. Yang et al., 2018). Accordingly, South Tarim should correlate with the Kunlun-Qaidam continent and North Tarim would have connected with North China craton.

In general, the Archean basement of the Tarim craton consists of orthogneiss, tonalite-trondhjemite-granodiorite (TTG) gneiss, and amphibolite enclaves with predominately ages of ca. 2.8–2.55 Ga (e.g., Z. X. Li et al., 2015; Lu, 1992; Lu & Yuan, 2003; S. N. Lu et al., 2006; Mei et al., 1998), the oldest ages of ca. 3.6 Ga were found in the Altyn Tagh Range (e.g., S. Lu et al., 2008) and ca.3.7 Ga TTGs by Ge et al. (2018, 2020). Paleoproterozoic metapelites unconformably overlie Archean basement, and early Paleoproterozoic mag-

matism occurred throughout Tarim craton with the ages ranging from 2.45 Ga to 2.35 Ga (Lu, 2002; Lu & Yuan, 2003; Lu et al., 2006, 2008). The ca. 1.95 Ga magmatic and ca. 1.92–1.91 Ga metamorphic events are similar to that of the Khondalite orogen in North China craton (e.g., R. Ge et al., 2015; S. N. Lu et al., 2006, 2008; G. C. Zhao et al., 2005; Santosh et al., 2006, 2007; Zhao, 2009). In the late Paleoproterozoic, the occurrence of 1.85–1.77 Ga mafic dikes and rapakivi granites suggests that the Tarim craton may have undergone extension (Lu et al., 2006, 2008; W. Xiao et al., 2003). Island arcs accreted to South Tarim in the Mesoproterozoic were subsequently intruded by ca. 1.4 Ga A-type granites, whereas North Tarim have been an undisturbed passive margin throughout the Mesoproterozoic (e.g., K. Y. Guo et al., 2004; A. G. Wang et al., 2004; Ye et al., 2016).

An early Neoproterozoic Tarim arc (ca. 970–890 Ga) created by a north-dipping subduction zone may have been developed prior to the collision between North Tarim and South Tarim along the inferred Aksu suture (e.g., Y. Chen et al., 2004; Cowgill et al., 2003; G. E. Gehrels et al., 2003a; Turner, 2010; Zheng et al., 2010; Zuza & Yin, 2017), and regional metamorphism occurred at ca. 830–790 Ma (e.g., Y. Chen et al., 2004; He et al., 2012; Ge et al., 2016). Tarim may have experienced rifting and the development of extensive passive margins in the middle and late Neoproterozoic, which was associated with the opening of the Tethys oceans (e.g., Turner, 2010; C. Wu, Yin et al., 2016; C. L. Zhang et al., 2016). The margins of the united Tarim craton were overlain by a succession of latest Neoproterozoic to Cambrian passive-margin strata (e.g., K. Y. Guo et al., 2004). Drill-hole and seismic reflection data suggest the existence of unconformities and an early Paleozoic thrust belt below Quaternary cover of the Tarim Basin (e.g., Carroll et al., 2001; Jia, 1997; Lin et al., 2012; P. Yang et al., 2020; Yin & Nie, 1996), which may correlate with the early Paleozoic Qilian orogen to the east (e.g., A. V. Zuza & Yin, 2017). Late Paleozoic-Mesozoic arc magmatism occurred along the southern margin of Tarim craton (Cowgill et al., 2003; W. J. Xiao et al., 2005), which represents the westward continuation of the Kunlun arc developed in the southeast of the Kunlun-Qaidam continent (e.g., Cowgill et al., 2003; Jiang et al., 1992; C. Wu, Yin et al., 2016; C. Wu, Zuza, Chen et al., 2019).

2.3. Kunlun-Qaidam Continent

The basement of the Kunlun-Qaidam continent consists of deformed Mesoproterozoic cover strata overlying Archean to Proterozoic crystalline basement rocks (G. E. Gehrels et al., 2003b; Pan et al., 2004; Qinghai BGMR, 1991; X. Yu et al., 2017). Precambrian basement in the Quanji massif consists of medium-to high-grade metamorphic rocks overlain by Mesoproterozoic and Neoproterozoic strata (e.g., L. Chen et al., 2013; J. Gong et al., 2012; Lu, 2002; Qinghai BGMR, 1991; J. P. Sun et al., 2019; Y. Wan et al., 2006; Q. Wang et al., 2008, 2009; L. Zhang et al., 2014). The Kunlun-Qaidam continent underwent progressive subduction, arc magmatism, and orogeny throughout the Neoproterozoic, Paleozoic, and Mesozoic (e.g., X. H. Chen et al., 2012, 2014; Y. Dong et al., 2018; G. E. Gehrels et al., 2003a, 2003b; G. Gehrels, Kapp et al., 2011; S. Song et al., 2013, 2014; C. Wu et al., 2016a, 2019a, 2020; W. Xiao et al., 2009c; Yin, Dang, et al., 2007, 2008a; A. V. Zuza et al., 2018), which were associated with collision of the Proto-, Paleo-, and Neo-Kunlun arcs, respectively (e.g., C. Wu et al., 2016a, 2019a, 2020). The region has been reactivated by the Cenozoic North Qaidam and Qilian Shan thrust belts, and Kunlun and Haiyuan left-slip transpressional systems (e.g., Clark et al., 2010; A. R. Duvall et al., 2011, 2013; Yin, Manning et al., 2007, 2008a, 2008b; A. V. Zuza et al., 2016, 2018, 2019; C. Wu, Zuza, Chen et al., 2019; C. Wu, Zuza, Zhou et al., 2019; C. Wu, Liu, Fan et al. 2020).

2.4. Early Paleozoic Qilian Orogen

The early Paleozoic Qilian orogen is the most dominant feature of northern Tibet, and most of the rock exposures here are related to the orogen and proceeding arc system (Figure 3). This collisional orogen records the closure of the Qilian Ocean as the Kunlun-Qaidam continent collided against the North China craton (G. E. Gehrels et al., 2003a, 2003b; Sengör & Natal'in, 1996; Sobel & Arnaud, 1999; S. Song et al., 2013, 2014; C. Wu et al., 2017; Xiao et al., 2009a, 2009b; Yin & Harrison, 2000; Yin, Dang et al., 2007; Yin & Nie, 1996; Yin, Manning et al., 2007; A. V. Zuza et al., 2018). Northwest-trending discontinuous belts of Cambrian-Ordovician ophiolite-mélange material, Ordovician-Silurian arc rocks (e.g., plutons and volcanic rocks), and ultra-high-pressure rocks are distributed throughout the Qilian Shan and northern Qaidam Basin (Figure 3) (Menold et al., 2009, 2016; S. Song et al., 2013, 2014, 2019; Yin & Harrison, 2000; Yin, Dang et al., 2007; Yin

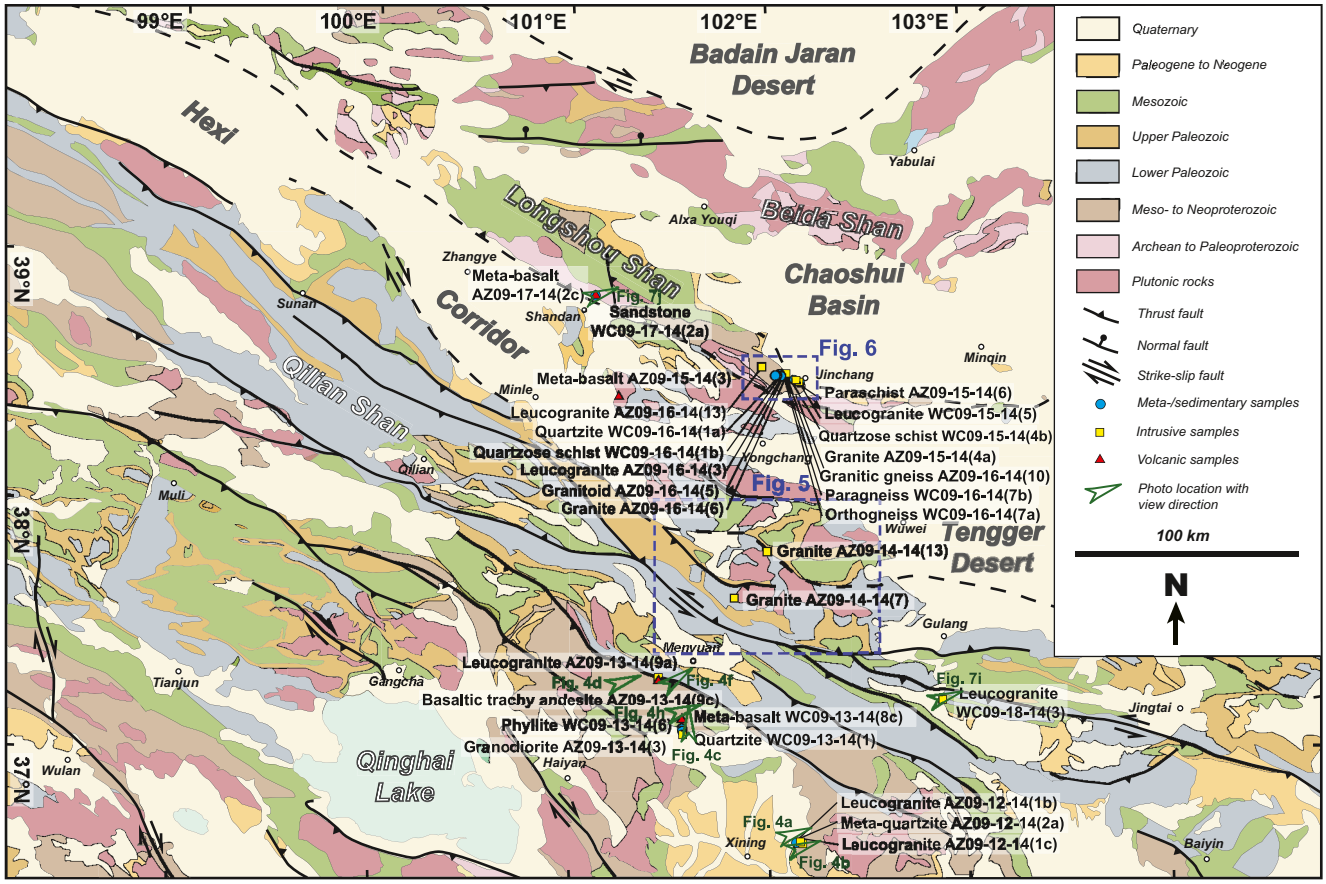

Figure 3. Simplified overview geologic map of the northeastern Tibetan Plateau and its northern foreland. Location shown in Figure 1b. The geology was compiled from Gansu Geological Bureau (1989), Qinghai BGMR (1991), Pan et al. (2004), Gong et al. (2013), and our own geologic mapping. Also shown are sample sites and the location of detailed geologic maps in Figures 4–6.

& Nie, 1996; Yin, Manning et al., 2007; S. Y. Yu et al., 2019; J. X. Zhang et al., 2005, 2008). Recent reviews of this orogen are provided in Song et al. (2013), Wu et al. (2017), and Zuza et al. (2018).

3. Field Mapping and Field Relationships

In this study, we examined several key areas across the Qilian Shan along the northeastern margin of the Tibetan plateau and the Longshou Shan in the foreland of the plateau along the southern margin of North China (e.g., the Hexi corridor) (Figure 1). Two of the field sites were relatively small (i.e., several important outcrops), and two involved larger regions (>500 km^2) where we synthesized existing geologic maps aided with our own mapping and more detailed field observations (Figure 4).

3.1. Datong Mountains North of Haidong

We examined the structural relationships and collected samples along a west-flowing Datong river drainage at ~36.63°N, ~102.15°E, just north of the town of Haidong (Figure 3). Here, relatively unmetamorphosed quartzite rocks are in fault contact with mylonitic schist/gneiss unit. Both units are assigned Proterozoic ages by Pan et al. (2004). The gneissic rocks are thrust over the quartzite unit along a 30° north-dipping fault (Figure 4a). The mylonitic gneiss, which includes lenses of schist, is intruded by leucogranite (Figure 4b).

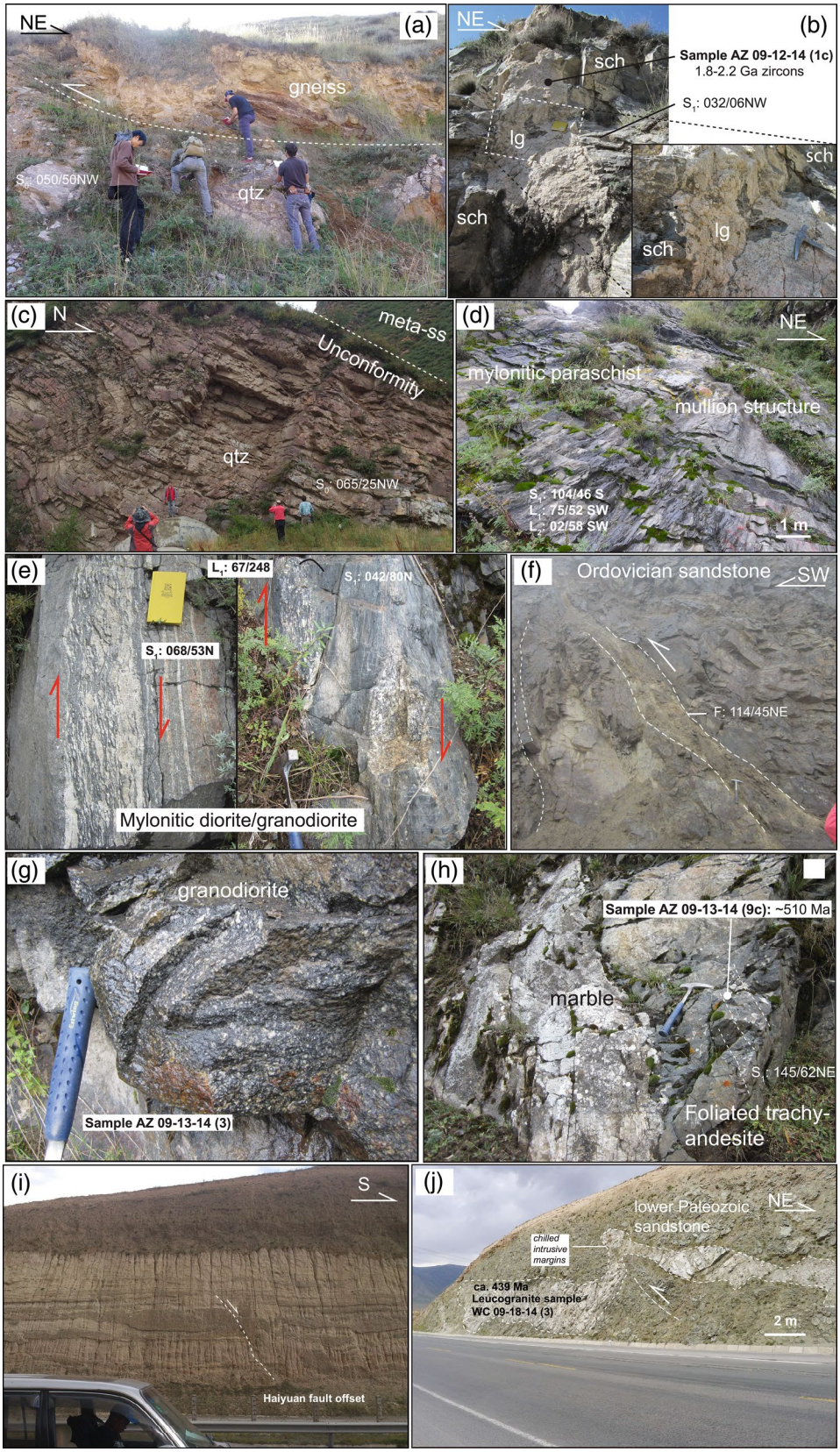
(a)
NE
gneiss
qtz
S_0: 050/50NW
(b)
NE
sch
Sample AZ 09-12-14 (1c)
1.8-2.2 Ga zircons
S_1: 032/06NW
lg
sch
sch
lg
sch
(c)
N
meta-ss
Unconformity
qtz
S_0: 065/25NW
(d)
NE
mylonitic paraschist
mullion structure
S_1: 104/46 S
L_1: 75/52 SW
L_2: 02/58 SW
1 m
(e)
L_1: 67/248
S_1: 042/80N
S_1: 068/53N
Mylonitic diorite/granodiorite
(f)
Ordovician sandstone
SW
F: 114/45NE
(g)
granodiorite
Sample AZ 09-13-14 (3)
(h)
Sample AZ 09-13-14 (9c): ~510 Ma
marble
S_1: 145/62NE
Foliated trachy-andesite
(i)
S
Haiyuan fault offset
(j)
lower Paleozoic sandstone
NE
chilled intrusive margins
ca. 439 Ma
Leucogranite sample
WC 09-18-14 (3)
2 m

3.2. Near Menyuan

We examined the structural relationships and collected samples along a southeast-flowing river drainage at ~37.1°N, ~101.5°E north of the city of Menyuan (Figure 3). Along this drainage, the Mesoproterozoic strata are composed of the meta-basalt, quartzite (Figure 4c), mylonitic paraschist with mullion structure (Figure 4d), phyllite, and mylonitic gneiss (Figure 4e), which are thrust over the Early Paleozoic slightly metamorphosed submarine sedimentary along a ~45° north-dipping Mesoproterozoic strata-parallel fault (Figures 3 and 4f). Metamorphic grade increases from south to north, and the mylonitic gneiss was intruded by an early Paleozoic-Neoproterozoic (dated in this study) granodiorite dike (Figure 4g). The unconformity between the quartzite and metasandstone is common at the northern margin of the Xining Basin (Pan et al., 2004) (Figure 4c). Here, coarse-grained marbles that have been assigned a Silurian age (Pan et al., 2004) are interbedded with slightly metamorphosed volcanic (intermediate to mafic) and volcaniclastic rocks, i.e., foliated trachy-andesite (Figure 4h), which were intruded by a small leucogranite dike.

3.3. Haiyuan Fault

At ~37.5°N, ~102°E, the Cenozoic left-slip Haiyuan fault makes a ~20-km right-step to produce a prominent restraining bend (Figures 3 and 4i–4j) (e.g., B. Li et al., 2019; Zuza et al., 2016). Shortening (left-slip oblique thrusting) across this restraining bends exposes early Paleozoic rocks (e.g., volcaniclastic rock, plutons, and conglomerates) related to the Qilian orogen, overlying conformable late Paleozoic-Mesozoic strata, and Cenozoic terrestrial deposits (Figure 5). Devonian-Carboniferous strata unconformably overlie a mingled package of Ordovician granites (U-Pb zircon age of ca. 462 Ma by Zuza et al., 2018), low-grade Ordovician metasedimentary rocks, and Silurian shales/mudstones (Figure 5). These rocks are variably thrust over Carboniferous-Cretaceous strata (Figure 5). Using apatite (U-Th)/He thermochronometry, Zuza et al. (2016) showed via that this restraining bend experienced rapid exhumation at ca. 15–8 Ma. Li et al. (2019) later found rapid exhumation across this bend at ca. 15 Ma via apatite fission track (AFT) dating, which they interpreted to represent the initiation of the left-slip Haiyuan fault. A cross section across this restraining bend requires a minimum of ~11 km northeast-southwest shortening, although this minimum estimate does not consider strike-slip offset (Figure 4i). Approximately 50 km to the east, Gaudemer et al. (1995) estimated a total of ~95 km left-lateral offset along the central Qilian Shan, which assuming a ca. 15 Ma initiation age equates to bulk left-lateral slip rates of ~6 mm/yr. To the southeast, a folded leucogranite dike was cut by a thrust, which intrudes into the Lower Paleozoic sandstone (Figure 4j). From this field locality, we conducted whole-rock geochemical analysis (results in Section 4.3), U-Pb zircon dating (presented in Zuza et al., 2018), and low-temperature thermochronology (e.g., B. Li et al., 2019; Zuza et al., 2016).

3.4. Longshou Shan

The northwest-trending ~30-km-wide Longshou Shan are a ~300-km-long range located in the Hexi Corridor, west of the city of Jinchang, that are separate from the higher elevation Tibetan Plateau to the south (Figure 1). The range primarily exposes Proterozoic strata and metamorphic rocks that are thought to represent the southern margin of the North China craton (e.g., Bai & Dai, 1996; J. H. Gong et al., 2013, 2016; Tang & Bai, 2000; J. X. Zhang et al., 2013) (Figure 6). The present-day range physiography and exposures are controlled by northwest-striking Cenozoic thrust faults. The northeastern range-bounding fault is active, and there is evidence for Cenozoic faulting throughout the Longshou Shan, including several east-striking left separation faults (Figure 6).

Our investigation was mainly focused around the easternmost Longshou Shan, near the city of Jinchang (Figures 3 and 6). The geologic map in Figure 6 was compiled from Pan et al. (2004), Tung et al. (2007),

Figure 4. Field photographs from the eastern Qilian Shan. (a) The gneissic rocks are thrust over the quartzite unit along a 30° north-dipping fault. (b) The leucogranite dike intrudes into the schist unit. (c) The syncline quartzite is in unconformable contact with the underlying meta-sandstone. (d) The A-type fold, i.e., mullion structure is developed in the mylonite. (e) Mylonitic gneiss shows the right shear stretching lineation. (f) Ordovician slightly metamorphosed sandstone thrust over the Mesoproterozoic schist. (g) Foliated granodiorite sample AZ 09-13-14 (3). (h) Proterozoic marble and foliated trachy-andesite unit, i.e., sample AZ 09-13-14 (9c). (i) a fault offset occurs within the Cenozoic coarse-grained sediments (j) Leucogranite dike intrudes into the Lower Paleozoic sandstone, which cut by a young thrust associated with the Haiyuan fault. The original filed pictures are shown in Figure S1.

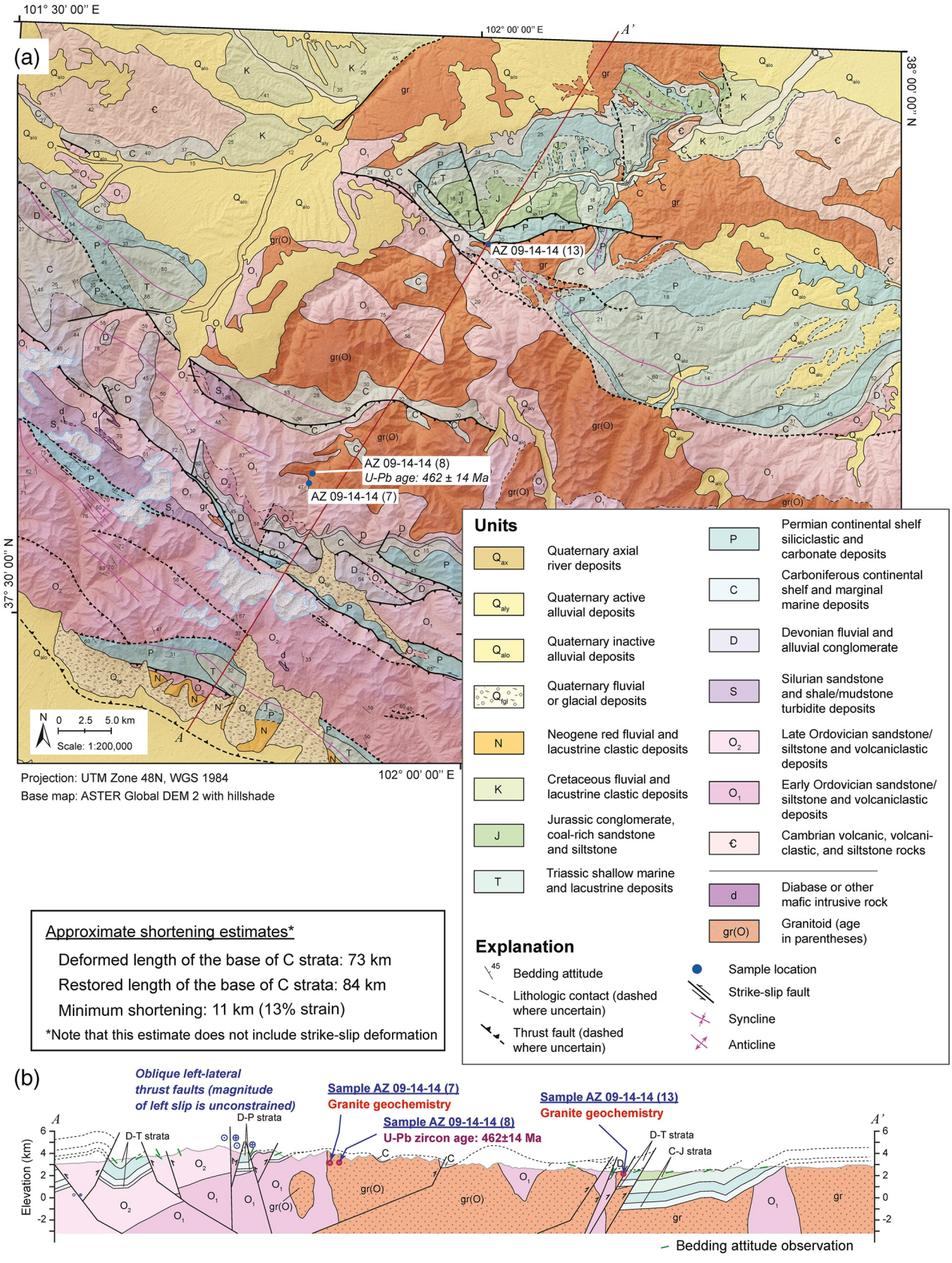
(a)
101° 30' 00" E
102° 00' 00" E
38° 00' 00" N
37° 30' 00" N
A
A'
AZ 09-14-14 (13)
AZ 09-14-14 (8)
U-Pb age: 462 ± 14 Ma
AZ 09-14-14 (7)
N 0 2.5 5.0 km
Scale: 1:200,000
Projection: UTM Zone 48N, WGS 1984
Base map: ASTER Global DEM 2 with hillshade
Units
Quaternary axial river deposits
Quaternary active alluvial deposits
Quaternary inactive alluvial deposits
Quaternary fluvial or glacial deposits
Neogene red fluvial and lacustrine clastic deposits
Cretaceous fluvial and lacustrine clastic deposits
Jurassic conglomerate, coal-rich sandstone and siltstone
Triassic shallow marine and lacustrine deposits
Permian continental shelf siliciclastic and carbonate deposits
Carboniferous continental shelf and marginal marine deposits
Devonian fluvial and alluvial conglomerate
Silurian sandstone and shale/mudstone turbidite deposits
Late Ordovician sandstone/ siltstone and volcaniclastic deposits
Early Ordovician sandstone/ siltstone and volcaniclastic deposits
Cambrian volcanic, volcaniclastic, and siltstone rocks
Diabase or other mafic intrusive rock
Granitoid (age in parentheses)
Explanation
Bedding attitude
Lithologic contact (dashed where uncertain)
Thrust fault (dashed where uncertain)
Sample location
Strike-slip fault
Syncline
Anticline
Approximate shortening estimates*
Deformed length of the base of C strata: 73 km
Restored length of the base of C strata: 84 km
Minimum shortening: 11 km (13% strain)
*Note that this estimate does not include strike-slip deformation
(b)
Oblique left-lateral thrust faults (magnitude of left slip is unconstrained)
Sample AZ 09-14-14 (7)
Granite geochemistry
Sample AZ 09-14-14 (8)
U-Pb zircon age: 462±14 Ma
Sample AZ 09-14-14 (13)
Granite geochemistry
D-P strata
D-T strata
C-J strata
Elevation (km)
Bedding attitude observation

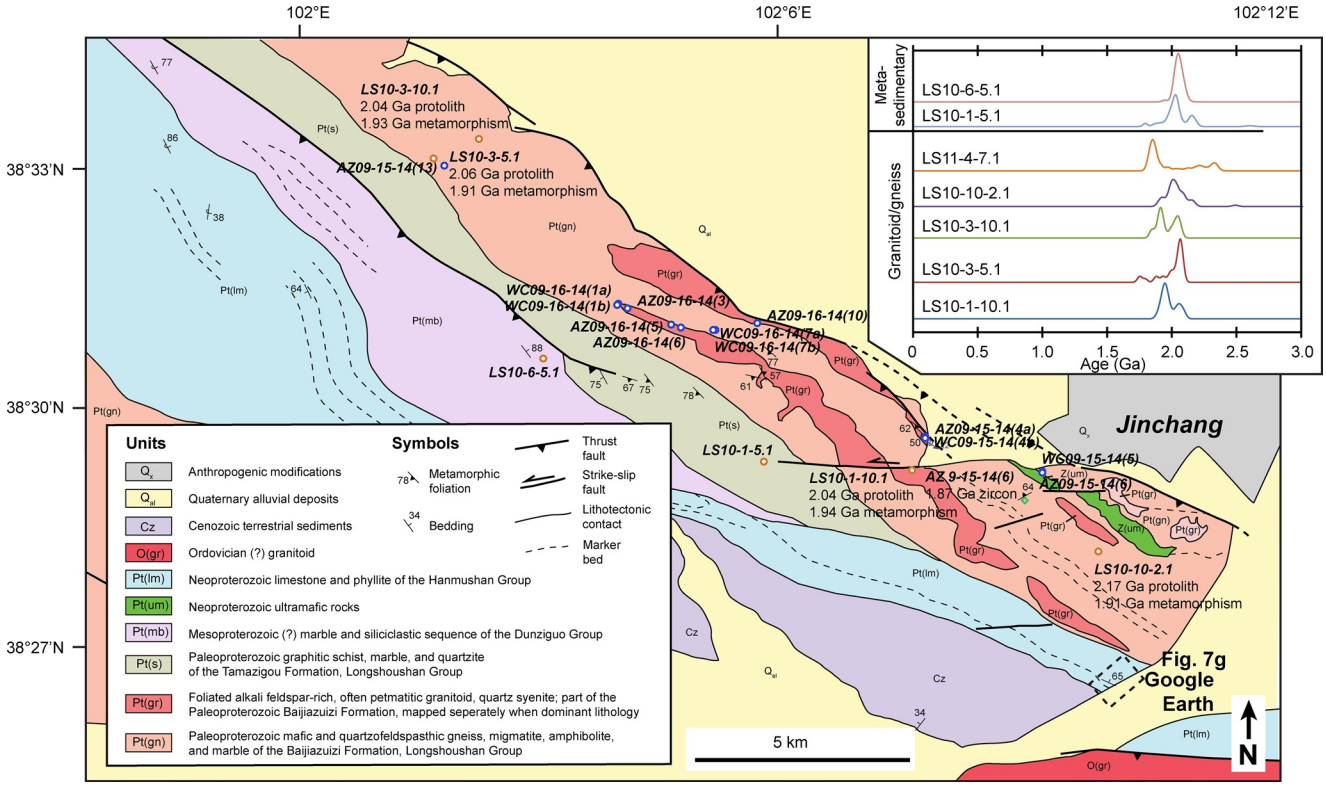

Figure 6. Geologic map of the eastern Longshou Shan, near the Jinchuan intrusion in Jinchang (e.g., Lehmann et al., 2007). This map is based on our new observations, and previous mapping presented in Pan et al. (2004), Tung et al. (2007), and Gong et al. (2013, 2016). Samples from this study are shown, and the inset shows zircon ages of Gong et al. (2016).

Gong et al. (2013, 2016), and our new observations. Recent U-Pb zircon geochronology data from this study and Gong et al. (2016) are also included on this map (Figure 6). In the northeastern Longshou Shan, the most prominent rocks are part of the Paleoproterozoic Longshou Shan "Group" or "Complex" (J. Gong et al., 2016; J. H. Gong et al., 2013; Lehmann et al., 2007; K. Tung et al., 2007). These rocks consist of variably metamorphosed (amphibolite -grade) and folded marble, schist, amphibolite, quartzite and orthogneiss intruded by younger granitoids, leucogranites, and (ultra)mafic intrusions (Figures 7a–7d) (e.g., J. Gong et al., 2016; Lehmann et al., 2007). A key observation on a leucogranite intrusion help us better constrain the depositional age of the Longshou Shan Group in this study (Figures 7c and 7d).

Slightly metamorphosed Mesoproterozoic strata (i.e., siliciclastic and carbonate rocks) unconformably overlie the relatively higher-grade Longshou Shan Group rocks (Figure 6). These rocks are referred to as the Dunzigou Group (e.g., J. Gong et al., 2016), and in the eastern Longshou Shan they primarily consist of massive blue limestones with quartzite and minor paraschist (Figure 7e). Although these rocks are less deformed than the underlying Longshou Shan Group, they are locally isoclinally folded (bedding often transposed) and intruded by leucogranite sills and dikes (Figures 7f and 7g). The Neoproterozoic Hanmushan Group consists of siliciclastic, limestone, diamictite (interpreted as glacial deposits), phyllite, schist, and basalt (Figure 7h). The Cambrian Dahuangshan Group is mainly exposed at the central Longshou Shan near the city of Shandan, which is consist of the quartz sandstone, slate, and slightly metamorphic volcanic rocks intruded by younger granitoids (Figure 7i). The Upper Silurian-Devonian strata unconformity over the Lower Paleozoic strata (i.e., Cambrian), which is consistent with the field observations from C. L. Zhang et al. (2016).

Figure 5. Geologic map and cross section across the Cenozoic left-slip Haiyuan fault, where it makes a ~20 km right-step to produce a prominent restraining bend. See Figure 3 for location.

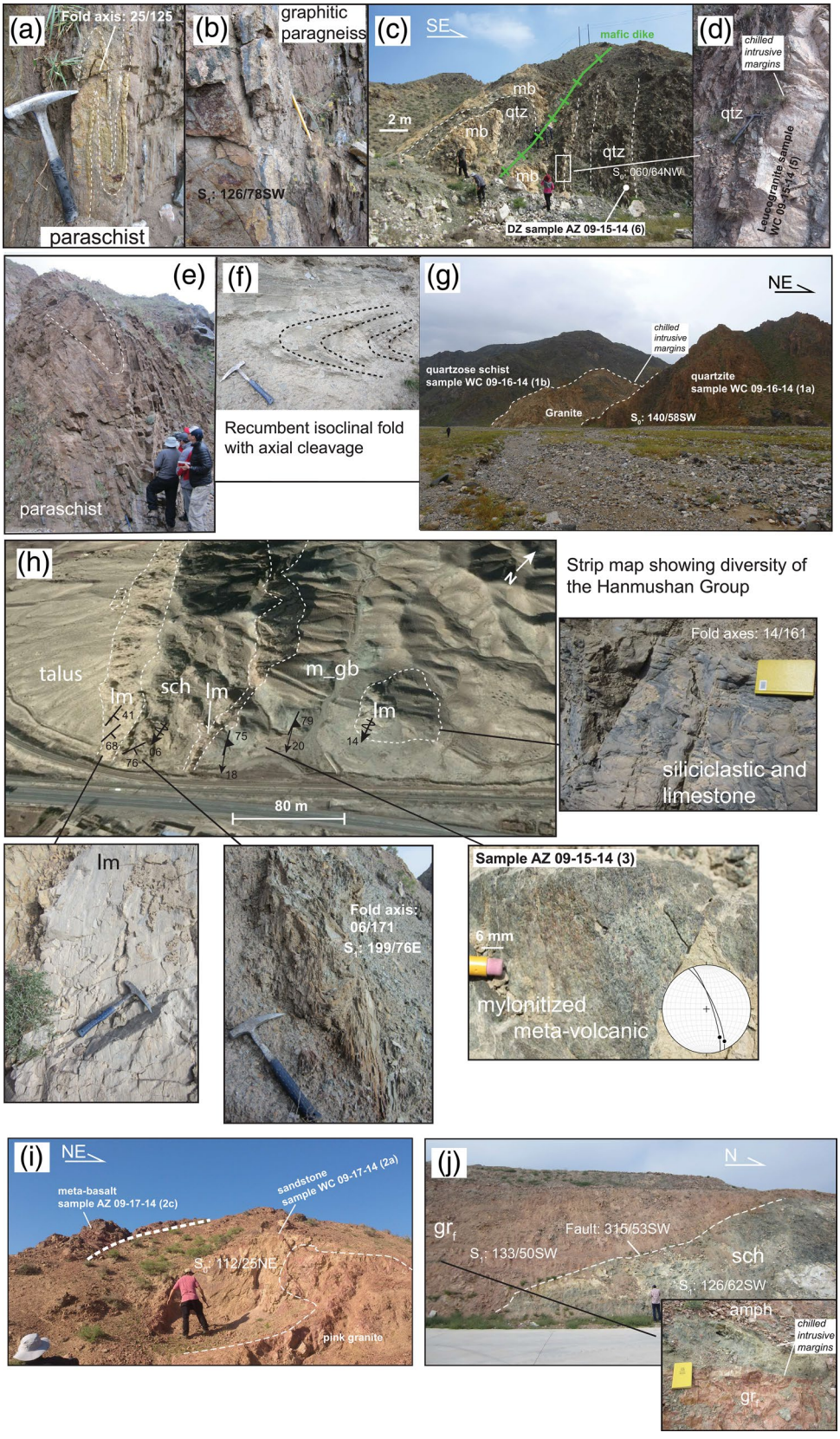
(a)
Fold axis: 25/125
paraschist
(b)
graphitic paragneiss
S1: 126/78SW
(c)
SE
mafic dike
mb
qtz
2 m
mb
qtz
mb
S0: 060/64NW
DZ sample AZ 09-15-14 (6)
(d)
chilled intrusive margins
qtz
Leucogranite sample WC 09-15-14 (5)
(e)
paraschist
(f)
Recumbent isoclinal fold with axial cleavage
(g)
NE
chilled intrusive margins
quartzose schist sample WC 09-16-14 (1b)
quartzite sample WC 09-16-14 (1a)
Granite
S0: 140/58SW
(h)
N
talus
lm
sch
lm
m_gb
lm
41
68
76
06
75
79
20
14
18
80 m
Strip map showing diversity of the Hanmushan Group
Fold axes: 14/161
siliciclastic and limestone
lm
Fold axis: 06/171
S1: 199/76E
Sample AZ 09-15-14 (3)
6 mm
mylonitized meta-volcanic
(i)
NE
meta-basalt sample AZ 09-17-14 (2c)
sandstone sample WC 09-17-14 (2a)
S0: 112/25NE
pink granite
(j)
N
gr
Fault: 315/53SW
S1: 133/50SW
sch
S1: 126/62SW
amph
chilled intrusive margins
gr

The easternmost segment of the Longshou Shan host the Neoproterozoic ultramafic Jinchuan intrusion (e.g., Lehmann et al., 2007; X. H. Li et al., 2004; X. Y. Song et al., 2006; M. Zhang et al., 2010), which is the third largest Ni-Cu deposit in the world. The intrusion has a U-Pb TIMS zircon age of 831 ± 0.6 Ma (M. Zhang et al., 2010), reported U-Pb SHRIMP zircon ages are ca. 827 Ma (X. H. Li et al., 2004, 2005), and inherited zircon ages are ca. 890 Ma and ca. 1840 Ma (X. H. Li et al., 2004). The intrusion has previously been related to Neoproterozoic continental rifting (Li & Ripley, 2011; Z. X. Li et al., 2005; Porter, 2016; Tang et al., 2014). We note that ca. 820 Ma extension related intrusions in the Longshou Shan may correlate with ca. 825 Ma A-type granitoids in the central Qilian Shan (C. Wu et al., 2017). We also observed the pink granite intrudes into the Longshou Shan Group schist and amphibolite unit near the Jinchuan Ni-Cu ore district (Figure 7j).

4. Geochronology and Geochemistry

4.1. Sample Descriptions

Samples for zircon geochronology and whole-rock geochemistry were collected during summer fieldwork in 2014, the detailed information is shown in the Table 1. North of Haidong, leucogranite (samples AZ 09-12-14 [1b] and AZ09-12-14 [1c]) (see location in Figure 3) crosscuts a Proterozoic mylonitic schist unit (Figure 4b). Field and map relationships suggest that this unit is thrust over an adjacent meta-quartzite assigned a Paleoproterozoic age (sample AZ 09-12-14 [2a]). Samples AZ 09-13-14 (1), AZ 09-13-14 (6), and WC 09-13-14 (8c) were collected from the quartzite, phyllite, and meta-basalt layers from Meso-to Neoproterozoic strata along the northern margin of the Xining Basin, which is the basement of the eastern Qilian Shan intruded by the Neoproterozoic granodiorite (sample AZ 09-13-14 [3]). West of the town of Menyuan, interbedded Silurian marble and meta-volcanic rocks are intruded by leucogranites. Samples AZ 09-13-14 (9a) and AZ 09-13-14 (9c) were collected from the leucogranite and meta-volcanic (basaltic trachy andesite) rocks, respectively. An early Paleozoic granite pluton yielding 462 ± 14 Ma reported by Zuza et al. (2018) was sampled from the central Haiyuan fault restraining bend (Figures 3 and 5) for geochemical analyses (samples AZ 09-14-14 [7] and AZ 09-14-14 [13]). Sample WC 09-18-14 (3) was collected from the leucogranite dike intruded into the Lower Paleozoic sandstone in the Central Haiyuan fault restraining bend (Figure 4j).

One early Paleozoic basaltic trachy andesite sample AZ 09-15-14 (3) was collected from the Hexi Corridor for geochemistry (Figure 7h). Metamorphic basement rocks in the eastern Longshou Shan near Jinchang were intruded by weakly foliated granitoids and leucogranites. We collected the two quartz schist samples WC 09-15-14 (4b) and WC 09-16-14 (1b), schist sample AZ 09-15-14 (6), quartzite sample WC 09-16-14 (1a), and orthogneiss sample WC 09-16-14 (7a) for the detrital zircon U-Pb analysis. Leucogranite samples WC 09-15-14 (5), AZ 09-16-14 (10), AZ 09-16-14 (13), WC 09-16-14 (7b), slightly foliated granitoid samples WC 09-15-14 (4a), granitoid samples AZ 09-16-14 (3), AZ 09-16-14 (5), and AZ 09-16-14 (6) were collected for the zircon U-Pb dating and/or geochemistry analysis. We collected one sample AZ 09-17-2014 (2c) from the meta-volcanic layer of the Lower Paleozoic strata (i.e., Cambrian) and one slightly metamorphic sandstone sample WC 09-17-14 (2a) from slightly deformed Devonian rocks (Figure 7j).

4.2. U-Pb Zircon Geochronology

Zircon grains for U-Pb dating were separated from 11 igneous rocks and 9 metasedimentary samples by traditional methods involving crushing, sieving, and magnetic and density separations, and mounted in epoxy with standard zircons (e.g., G. E. Gehrels et al., 2006, 2003a; Pullen et al., 2018). Individual zircon grains were picked under a binocular microscope. To identify the internal structure and texture of the zircon grains

Figure 7. (a-b) Filed photographs from the Longshou Shan Group, folded paraschist, foliated graphitic paragneiss. (c) Folded marble and quartzite unit is intruded by the mafic dike. (d) A leucogranite dike intrudes into the Longshou Shan Group quartzite. (e) Folded paraschist of the Dunzigou Group. (f) Isoclinal fold is developed within the Dunzigou Group meta-sandstone unit. (g) Granite sill intrudes into the Dunzigou quartzite and quartzschist units. (h) Strip map showing diversity of the Hanmushan Group. (i) Paleozoic sandstone intruded by a pink granite sill unconformity over the Cambrian meta-basalt unit in the central Longshou Shan. (j) Neoproterozoic pink granite intrudes into the amphibolite unit and thrust over the Longshou Shan Group schist unit. The original filed pictures are shown in Figure S2.

Table 1
Summary of Sample Locations in the Eastern Qilian Shan and Longshou Shan

Sample number	Description	Latitude (°N)	Longitude (°E)	Elevation (m)	Method
Samples of igneous rocks					
AZ09-17-14 (2c)	Meta-volcanic rock	38°51′1.26″	101°5′48.06″	2,000	Geochemistry
AZ09-16-14 (13)	Leucogranite	38°33′15.54″	101°58′21.84″	2,330	U-Pb Zircon/Geochemistry
AZ09-16-14 (10)	Leucogranite	38°30′41.22″	102°5′53.70″	1,770	U-Pb Zircon/Geochemistry
AZ09-16-14 (3)	Granitoid	38°30′35.58″	102°3′4.14″	2,025	Geochemistry
AZ09-16-14 (5)	Granitoid	38°30′22.32″	102°4′6.42″	1,944	U-Pb Zircon/Geochemistry
AZ09-16-14 (6)	Granitoid	38°30′20.64″	102°4′22.08″	1,923	Geochemistry
WC09-16-14 (7a)	Orthogneiss	38°30′12.90″	102°4′58.44″	1,870	U-Pb Zircon
AZ09-15-14 (4a)	Foliated granitoid	38°29′45.06″	102°7′47.22″	1,660	Geochemistry
WC09-15-14 (5)	Leucogranite	38°28′54.12″	102°9′5.40″	1,675	U-Pb Zircon
AZ09-15-14 (3)	Meta-volcanic rock	38°26′34.32″	101°10′16.14″	2,348	Geochemistry
AZ09-14-14 (13)	Granite	37°49′35.10″	102°0′39.18″	2,369	Geochemistry
AZ09-14-14 (7)	Granite	37°37′9.06″	101°49′42.78″	3,241	Geochemistry
AZ09-13-14 (9a)	Leucogranite	37°18′0.42″	101°25′11.34″	3,287	U-Pb Zircon/Geochemistry
AZ09-13-14 (9c)	Basaltic trachy andesite	37°18′0.42″	101°25′11.34″	3,287	U-Pb Zircon/Geochemistry
WC09-18-14 (3)	Leucogranite	37°13′27.90″	102°50′08.98″	2,849	U-Pb Zircon
WC09-13-14 (8c)	Meta-basalt	37°8′8.70″	101°34′12.06″	2,688	U-Pb Zircon/Geochemistry
AZ09-13-14 (3)	Granodiorite	37° 5′ 23.92″	101°33′58.68″	2,121	U-Pb Zircon/Geochemistry
AZ09-12-14 (1b)	Granitoid	36°37′51.78″	102° 8′9.66″	1,588	Geochemistry
AZ09-12-14 (1c)	Leucogranite	36°37′51.78″	102° 8′9.66″	1,588	U-Pb Zircon
Metasedimentary samples					
WC09-17-14 (2a)	sandstone	38°51′1.26″	101°5′48.06″	2,000	U-Pb Zircon
WC09-16-14 (1a)	Quartzite	38°30′41.52″	102°2′49.26″	2,062	U-Pb Zircon
WC09-16-14 (1b)	Quartzose schist	38°30′41.52″	102°2′49.26″	2,062	U-Pb Zircon
WC09-16-14 (7b)	Paragneiss	38°30′12.90″	102°4′58.44″	1,870	U-Pb Zircon
WC09-15-14 (4b)	Quartzose schist	38°29′45.06″	102°7′47.22″	1,660	U-Pb Zircon
AZ09-15-14 (6)	Paraschist	38°28′54.12″	102°9′5.52″	1,689	U-Pb Zircon
WC09-13-14 (6)	Phyllite	37°5′49.80″	101°33′58.98″	2,645	U-Pb Zircon
WC09-13-14 (1)	Quartzite	37°4′26.64″	101°34′9.42″	2,614	U-Pb Zircon
AZ09-12-14 (2a)	Meta-quartzite	36°37′48.90″	102° 8′58.62″	1562	U-Pb Zircon

and to select potential positions for U-Pb analysis, cathodoluminescence (CL) images of zircons were taken on a JXA-880 electron microscope and an image analysis software was used under operating conditions of 20 kV and 20 nA, at the Institute of Mineral Resources, Chinese Academy of Geological Sciences, Beijing, China. Zircons of each sample were randomly selected, mounted in epoxy resin and polished, in order to conduct U-Pb laser ablation inductively coupled plasma mass spectrometer (LA-ICP-MS) dating. Most zircons were analyzed using an Agilent 7500a ICP-MS coupled with a New Wave Research UP193FX Excimer at the Key Laboratory of Continental Collision and Plateau Uplift, Institute of Tibetan Plateau Research, Chinese Academy of Sciences, Beijing. The LA-MC-ICP-MS analytical procedures employed for polished and depth-profile analyses are described in detail in G. Gehrels et al. (2011), and briefly summarized here. Common Pb corrections were made by using the measured ^{204}Pb and assuming an initial Pb composition from Stacey and Kramers (1975). The primary standard used was GJ1 (Jackson et al., 2004). The secondary standards were 91,500 (^{238}U/^{206}Pb age of 1,065 Ma; Wiedenbeck et al., 1995), and Plesovice (^{238}U/^{206}Pb age of 337 Ma; Sláma et al., 2008).

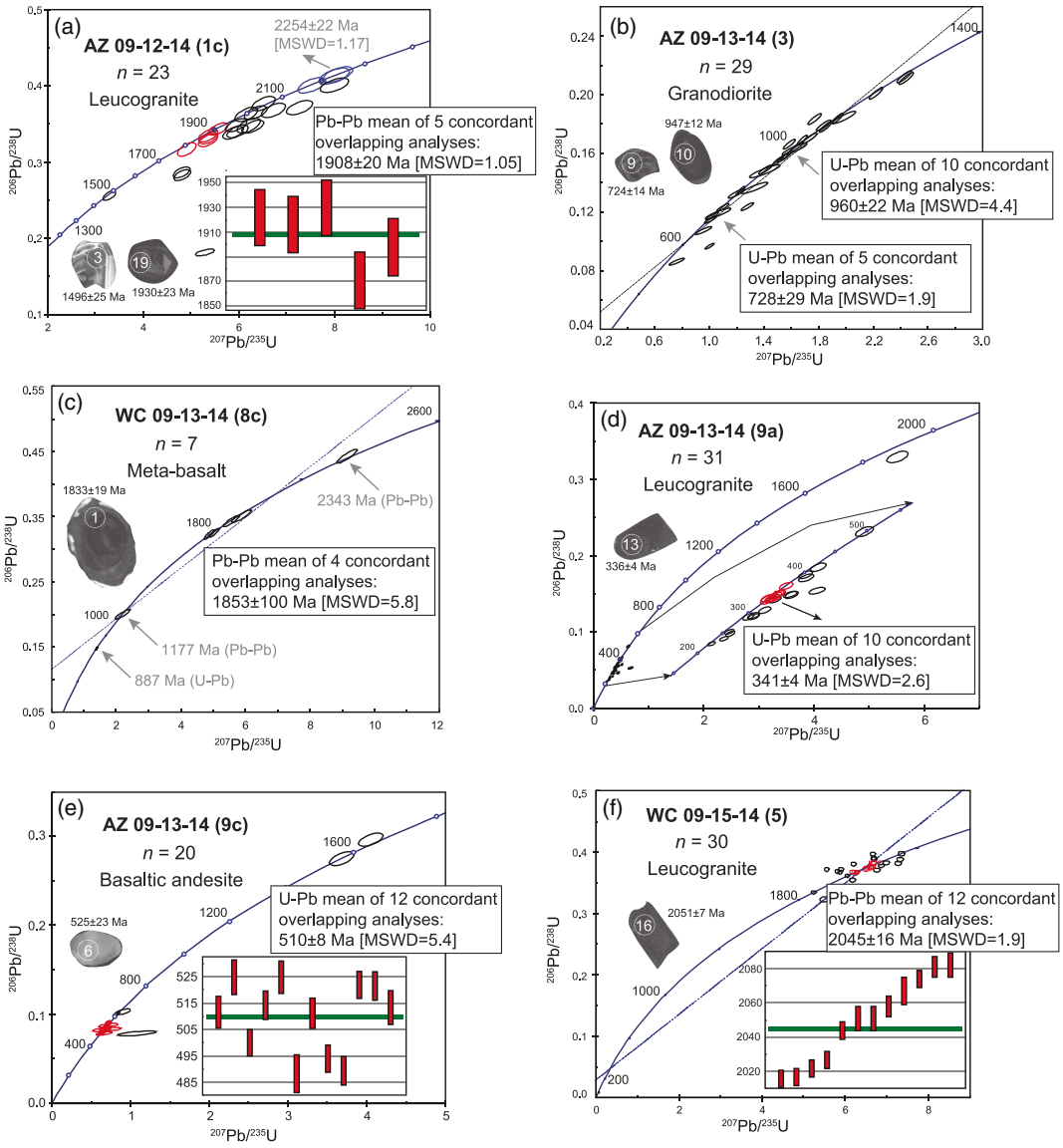

Figure 8. U-Pb concordia diagrams showing results of single shot zircon analyses and relative probability plots of zircon ages for each sample. Error ellipses are 2σ and red ellipses show individual analyses were included in the weighted mean age calculation.

The goal of our U-Pb zircon geochronology was to determine the crystallization age of the igneous samples and for the sedimentary samples, we examined the zircon-age spectrum to constrain the depositional age of the sample and constrain its provenance. The complete isotopic information for these analyses can be found in Table S1 and concise age results are presented in Table 1. The analytical data are presented in Figures 8 and 9.

For igneous samples, we aimed to analyze 20–35 zircon grains from each sample with the exception of samples AZ 09-16-14 (13) and WC 09-13-14 (8C). If multiple zircon-age populations existed, we interpreted the weighted mean age of the youngest population of concordant zircon ages to represent the crystallization age of the sample. We ascribe distinctly older zircon-age populations to inheritance and younger zircon ages to the results of Pb loss due to a younger metamorphic event. For zircon grains with Neoproterozoic-Paleozoic (or younger) ages, we use their $^{206}Pb/^{238}U$ ages, and for Mesoproterozoic and older zircon grains, we use their $^{206}Pb/^{207}Pb$ ages. For the detrital zircon samples, we considered analyses that were <30% discordant or <5% reversely discordant (e.g., G. Gehrels et al., 2011).

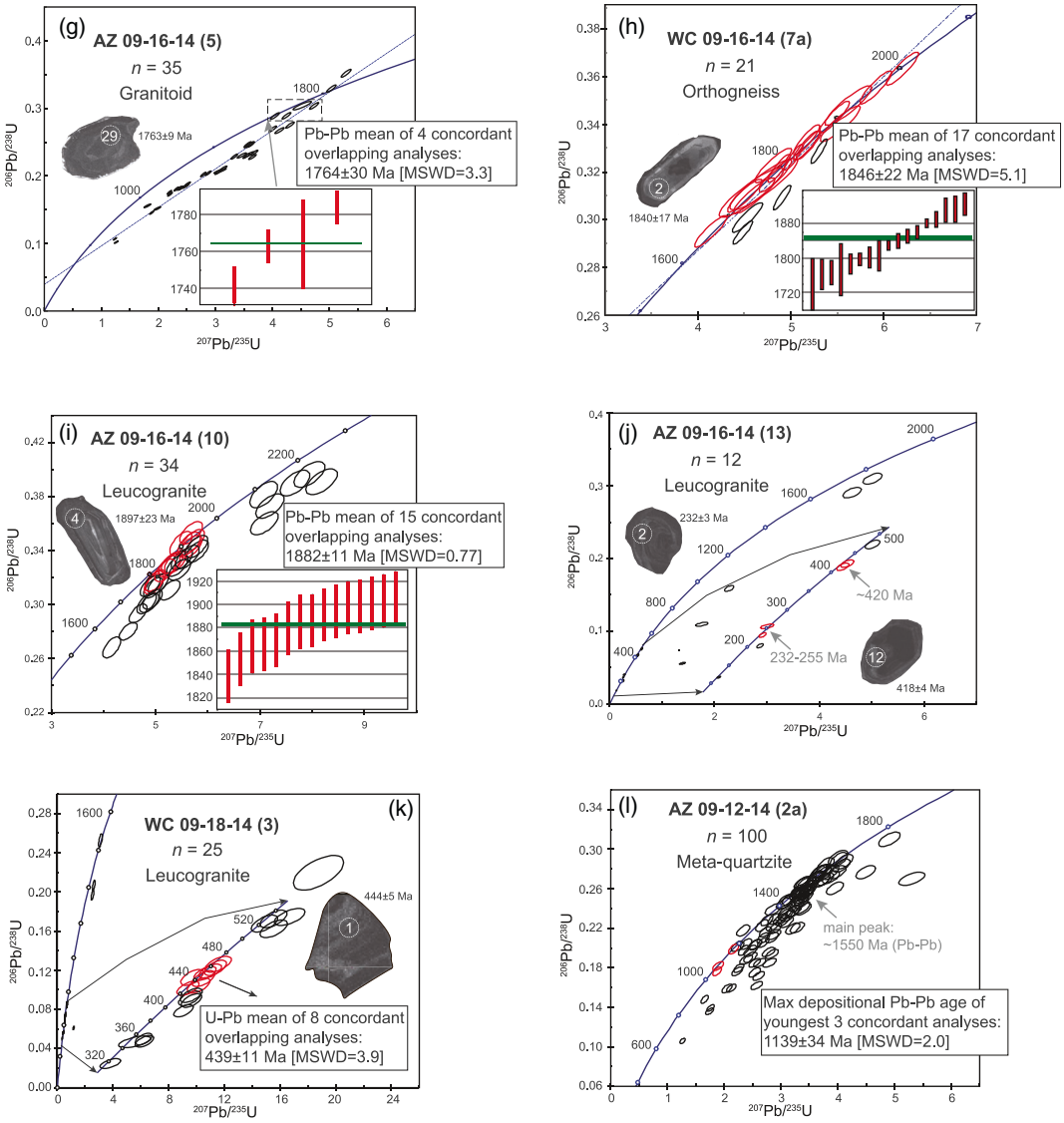

Figure 8. Continued

4.2.1. Leucogranite Sample AZ 09-12-14 (1c)

We analyzed 23 grains, of which 20 yield concordant ages ranging from 1.5 Ga to 2.3 Ga (Figure 8a). The youngest population of concordant analyses are clustered around ca. 1,900 Ma with a weighted mean age of 1,908 ± 20 Ma (MSWD = 1.05; n = 5) (Figure 8a; Table 1), and the youngest single concordant zircon yields an age of 1,496 ± 25 Ma (Table S1; Figure 8a). Because of the range of zircon ages in this leucogranite sample, we do not attempt to assign a crystallization age to this sample but note that it may record Paleo-to Mesoproterozoic crustal melting.

4.2.2. Granodiorite Sample AZ 09-13-14 (3)

We analyzed 29 zircon grains from this granodiorite sample, of which 24 yielded concordant ages ranging from 657 Ma to 1,290 Ma (Table S1; Figure 8b). The largest population of concordant analyses are clustered around ca. 950 Ma with a weighted mean age of 960 ± 22 Ma (MSWD = 4.4; n = 10) (Figure 8b; Table 1), and the youngest population of concordant zircon grains (n = 5) yields a weighted mean age of 728 ± 29 Ma (MSWD = 1.9) (Table S1; Figure 8b). We interpret the youngest population as the crystallization age of this granodiorite sample.

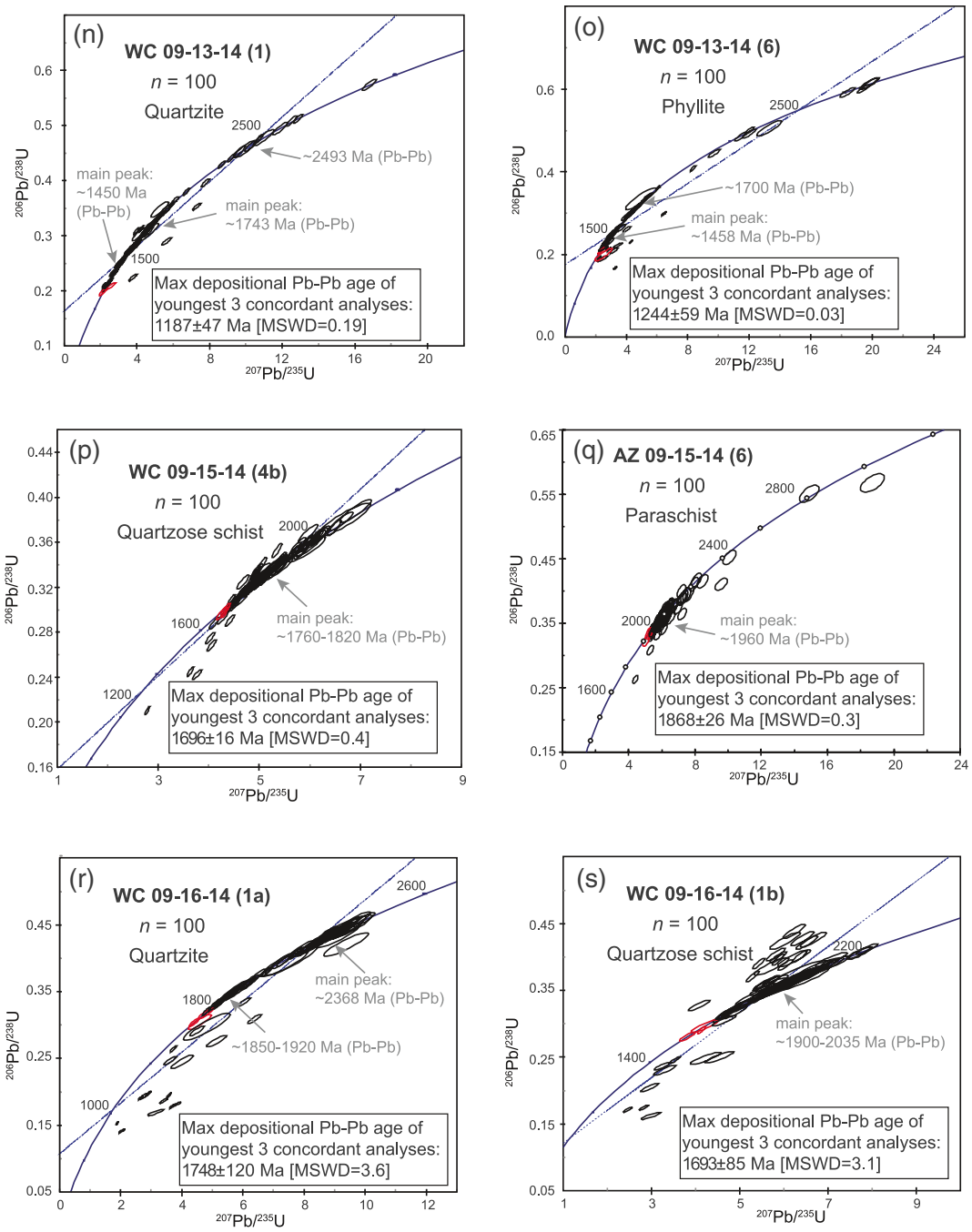

Figure 8. Continued

4.2.3. Meta-basalt Sample WC 09-13-14 (8c)

We analyzed 7 zircon grains and all yielded concordant ages ranging from 887 Ma to 2343 Ma (Table S1; Figure 8c). The largest population of concordant analyses are clustered around ca. 1,900 Ma with a weighted mean age of 1,853 ± 100 Ma (MSWD = 5.8; n = 4) (Figure 8c; Table 1), and the youngest single concordant zircon yields an age of 887 ± 12 Ma (Table S1; Figure 8c). In additional, there is a ~1,177 Ma age cluster, we also note the oldest single concordant zircon yields an age of 2,343 ± 20 Ma (Table S1; Figure 8c)

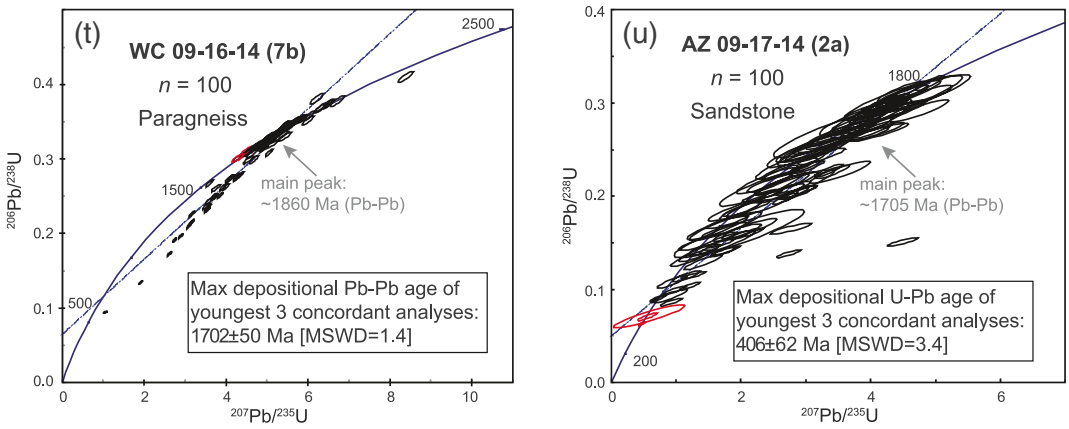

Figure 8. Continued

4.2.4. Leucogranite Sample AZ 09-13-14 (9a)

Thirty-one zircon grains were analyzed from this leucogranite sample, of which only 11 yielded concordant ages ranging from 225 Ma to 1,977 Ma (Table S1; Figure 8d). The weighted mean age of 6 concordant analyses is 341 ± 7 Ma (MSWD = 2.8) (Figure 8d; Table 1). However, minor populations of slightly discordant ca. 250 and ca. 300 Ma $^{206}Pb/^{238}U$ ages were also observed (Figure 8d).

4.2.5. Basaltic Trachy Andesite Sample AZ 09-13-14 (9c)

We analyzed 20 zircon grains and 14 yielded concordant ages ranging from 494 Ma to 1,608 Ma (Table S1; Figure 8e). The youngest population of concordant zircon grains (n = 8) yield a weighted mean age of 512 ± 10 Ma (MSWD = 4.2) (Figure 8e; Table 1), which we interpret as the crystallization age of this volcanic basaltic andesite. Two concordant zircon analyses yielded ca. 1.6 Ga ages, which may indicate that the Cambrian volcanic rocks passed through Mesoproterozoic crust prior to being erupted.

4.2.6. Leucogranite Sample WC 09-15-14 (5)

Thirty zircon grains were analyzed from this leucogranite sample, of which 28 yielded concordant ages ranging from 1,856 Ma to 2,221 Ma (Table S1; Figure 8f). The weighted mean age of 12 concordant analyses is 2,045 ± 16 Ma (MSWD = 1.9) (Figure 8f; Table 1), which we interpret as the crystallization age of this leucogranite sample.

4.2.7. Granitoid Sample AZ 09-16-14 (5)

Thirty-five zircon grains were analyzed from this granitoid sample, of which 8 yielded concordant ages ranging from 1,655 Ma to 1,848 Ma (Table S1; Figure 8g). The weighted mean age of 4 concordant analyses is 1,764 ± 30 Ma (MSWD = 3.3) (Figure 8g; Table 1), which we interpret as the crystallization age of this granitoid sample. A discordia line defined by the discordant grains projects toward ca. 1.8 Ga, which broadly supports the weighted mean age of ca. 1,764 Ga.

4.2.8. Orthogneiss Sample WC 09-16-14 (7a)

We analyzed 21 zircon grains from this orthogneiss sample, and all yielded concordant ages (Figure 8h). $^{207}Pb/^{206}Pb$ ages ranged from 1,657 Ma to 2,011 Ma (Table S1), and the weighted mean age of 17 concordant analyses is 1,846 ± 22 Ma (MSWD = 5.1) (Figure 8h), which we interpret as the crystallization age of this orthogneiss sample (Figure 8h).

4.2.9. Granitic Gneiss Sample AZ 09-16-14 (10)

We analyzed 34 zircon grains from this granitic gneiss sample, and all yielded concordant ages (Figure 8i). $^{207}Pb/^{206}Pb$ ages ranged from 1,838 Ma to 2,365 Ma (Table S1), and the weighted mean age of 15 concordant analyses is 1,882 ± 11 Ma (MSWD = 0.77) (Figure 8i), which we interpret as the crystallization age of this granit-

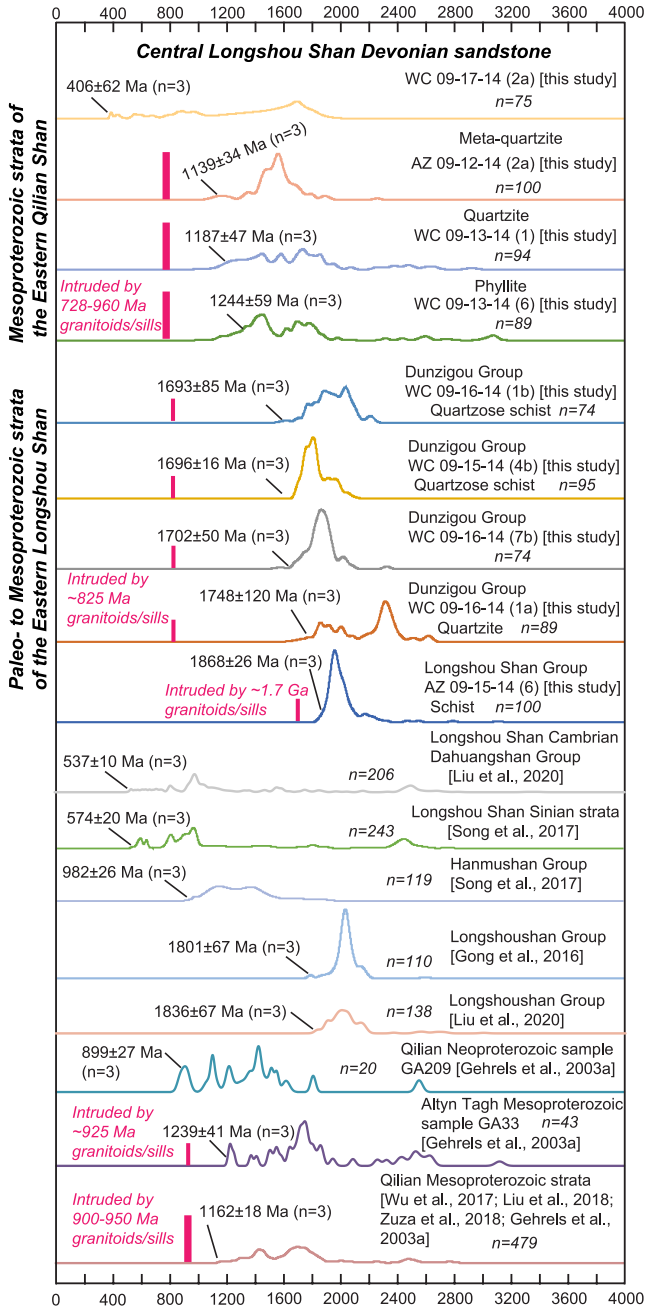

Figure 9. Mesoproterozoic-Neoproterozoic relative probability plot of detrital zircon data from around the northern Tibetan Plateau, detrital zircon samples from this study, Gehrels et al. (2003a), Zuza et al. (2018), Wu et al. (2017), Liu et al. (2018), Song et al. (2017), Gong et al. (2016), and Liu et al. (2020).

ic gneiss sample (Table 1). Note that six zircon grains had older $^{207}Pb/^{206}Pb$ ages of ca. 2.15–2.35 Ga (Table S1).

4.2.10. Leucogranite Sample AZ 09-16-14 (13)

We analyzed 12 zircon grains from this leucogranite sample, of which 10 yielded concordant ages ranging from 117 Ma to 1,912 Ma (Table S1; Figure 8j). Because of the range of zircon ages in this leucogranite sample, we do not attempt to assign a crystallization age to this sample but note that minor populations of slightly discordant 232–255 Ma and ca. 420 Ma $^{206}Pb/^{238}U$ ages (Figure 8j).

4.2.11. Leucogranite Sample WC 09-18-14 (3)

Twenty-five zircon grains were analyzed from this leucogranite sample, of which 22 yielded concordant ages ranging from 317 Ma to 1,479 Ma (Table S1; Figure 8k). The weighted mean age of 8 concordant analyses is 439 ± 11 Ma (MSWD = 3.9) (Figure 8k; Table 1), which we interpret as the crystallization age of this leucogranite sample. However, minor populations of slightly discordant ca. 317 and 350 Ma $^{206}Pb/^{238}U$ ages are also observed (Figure 8k).

4.2.12. Meta-quartzite Sample AZ 09-12-14 (2a)

We analyzed 100 grains and 14 grains yielded discordant ages (Figure 8l). Concordant ages ranged from 1,086 Ma to 1,924 Ma (Figure 9), and the weighted mean of the three youngest concordant zircon grains was 1,139 ± 34 Ma (mean square of weighted deviates, MSWD = 2.0) (Figure 8l; Table 1). We interpret this age to represent the maximum depositional age of this meta-quartzite sample. We also note the large population of 1.55 Ga zircon grains, and discordant zircons appear to define a discordia line that intercepts the concordia line at ca. 1.55 Ga (Figure 8l). This sample has a major zircon population of 1,400–1,700 Ma with prominent peak at 1,565 Ma (Figure 9).

4.2.13. Quartzite Sample WC 09-13-14 (1)

One hundred detrital zircon grains were analyzed from this sample (Figures 8n) and six grains yielded discordant ages (Figure 8n). Concordant ages ranged from 1,146 Ma to 2,925 Ma (Figure 9), and the weighted mean of the three youngest concordant zircon grains was 1,187 ± 47 Ma (mean square of weighted deviates, MSWD = 0.19) (Figure 8n; Table 1). We interpret this age to represent the maximum depositional age of this quartzite sample. This sample has two major zircon populations of 1,300–1,500 and 1,600–1,860 Ma, with two prominent peaks at ca. 1.45 and ca. 1.74 Ga, respectively (Figure 9). We noted a minor age population also occur at ca. 2.49-Ga (Figure 9).

4.2.14. Phyllite Sample WC 09-13-14 (6)

One hundred detrital zircon grains were analyzed from this sample (Figures 8o) and 11 grains yielded discordant ages (Figure 8o). Concordant ages ranged from 1,157 Ma to 3,083 Ma (Figure 9), and the weighted mean of the three youngest concordant zircon grains was 1,244 ± 59 Ma (mean square of weighted deviates, MSWD = 0.03) (Figure 8o; Table 1). We interpret this age to represent the maximum depositional age of this phyllite sample. This sample has two major zircon populations of 1,300–1,500 and 1,620–1,820 Ma, with two prominent peaks at ca. 1.46 and ca. 1.70 Ga, respectively (Figure 9). We noted a minor age population also occur at ca. 3.80-Ga (Figure 9).

4.2.15. Quartzose Schist Sample WC 09-15-14 (4b)

One hundred detrital zircon grains were analyzed from this sample (Figure 8p) and five grains yielded discordant ages (Figure 8p). Concordant ages ranged from 1,687 Ma to 2,085 Ma (Figure 9), and the weighted mean of the three youngest concordant zircon grains was 1,696 ± 16 Ma (mean square of weighted deviates, MSWD = 0.4) (Figure 8p; Table 1). We interpret this age to represent the maximum depositional age of this quartzose schist sample. This sample has a major zircon population of 1,700–2,000 Ma, with two prominent peaks at ca. 1.82 and ca. 1.91 Ga (Figure 9).

4.2.16. Schist Sample AZ 09-15-14 (6)

One hundred detrital zircon grains were analyzed from this sample (Figure 8q), and all analyses yielded concordant ages spanning from 1,860 Ma to 3,114 Ma (Table S1; Figure 9). The three youngest overlapping ages have a weighted mean age of 1,868 ± 26 Ma (MSWD = 0.3) (Figure 8q; Table 1), which represents the maximum depositional age of the meta-sedimentary rock. This sample has a major zircon population of 1.87–2.10 Ga with prominent peak at 1.96 Ga (Figure 9). The oldest two zircon grains have ages of 2,794 ± 21 and 3,114 ± 20 Ma.

4.2.17. Quartzite Sample WC 09-16-14 (1a)

One hundred detrital zircon grains were analyzed from this sample (Figure 8r) and 17 grains yielded discordant ages (Figure 8r). Concordant ages ranged from 1,665 Ma to 2,474 Ma (Figure 9), and the weighted mean of the three youngest concordant zircon grains was 1,748 ± 120 Ma (mean square of weighted deviates, MSWD = 3.6) (Figure 8r; Table 1). We interpret this age to represent the maximum depositional age of this quartzite sample. This sample has two major zircon populations of 1,830–2,080 and 2,200–2,390 Ma, with three prominent peaks at ca. 1.86, ca. 1.92, and ca. 2.33 Ga, respectively (Figure 9).

4.2.18. Quartzose Schist Sample WC 09-16-14 (1b)

One hundred detrital zircon grains were analyzed from this sample (Figure 8s) and 26 grains yielded discordant ages (Figure 8s). Concordant ages ranged from 1,611 Ma to 2,231 Ma (Figure 9), and the weighted mean of the three youngest concordant zircon grains was 1,693 ± 85 Ma (mean square of weighted deviates, MSWD = 3.1) (Figure 8s; Table 1). We interpret this age to represent the maximum depositional age of this quartzose schist sample. This sample has a major zircon population of 1,810–2,050 Ma, with two prominent peaks at ca. 1.87 and ca. 2.03 Ga (Figure 9). We note that a minor age population also occur at ca. 1.77-Ga (Figure 9).

4.2.19. Paragneiss Sample WC 09-16-14 (7b)

One hundred detrital zircon grains were analyzed from this sample (Figure 8t) and 26 grains yielded discordant ages (Figure 8t). Concordant ages ranged from 1,579 Ma to 2,328 Ma (Figure 9), and the weighted mean of the three youngest concordant zircon grains was 1,670 ± 100 Ma (mean square of weighted deviates, MSWD = 3.1) (Figure 8t; Table 1). We interpret this age to represent the maximum depositional age of this paragneiss sample. This sample has a major zircon population of 1,740–1,940 Ma, with two prominent peaks at ca. 1.86 Ga and ca. 1.90 Ga, respectively (Figure 9).

4.2.20. Sandstone Sample WC 09-17-14 (2a)

One hundred detrital zircon grains were analyzed from this sample (Figures 8u) and 25 grains yielded discordant ages (Figure 8u). Concordant ages ranged from 394 Ma to 1,831 Ma (Figure 9), and the weighted mean of the three youngest concordant zircon grains was 406 ± 62 Ma (mean square of weighted deviates, MSWD = 3.4) (Figure 8u; Table 1). We interpret this age to represent the maximum depositional age of this sandstone sample. This sample has a major zircon population of 1,500–1,830 Ma, with a prominent peak at ca. 1.70 Ga (Figure 9). We noted two minor age populations also occur at ca. 900 and ca. 500 Ma, respectively (Figure 9).

4.3. Whole-Rock Geochemistry

Granitoid and volcanic rock samples were analyzed for major and trace elements at the Chinese Academy of Geologic Sciences in Beijing, China. Major elements were analyzed using an X-ray fluorescence spectrom-

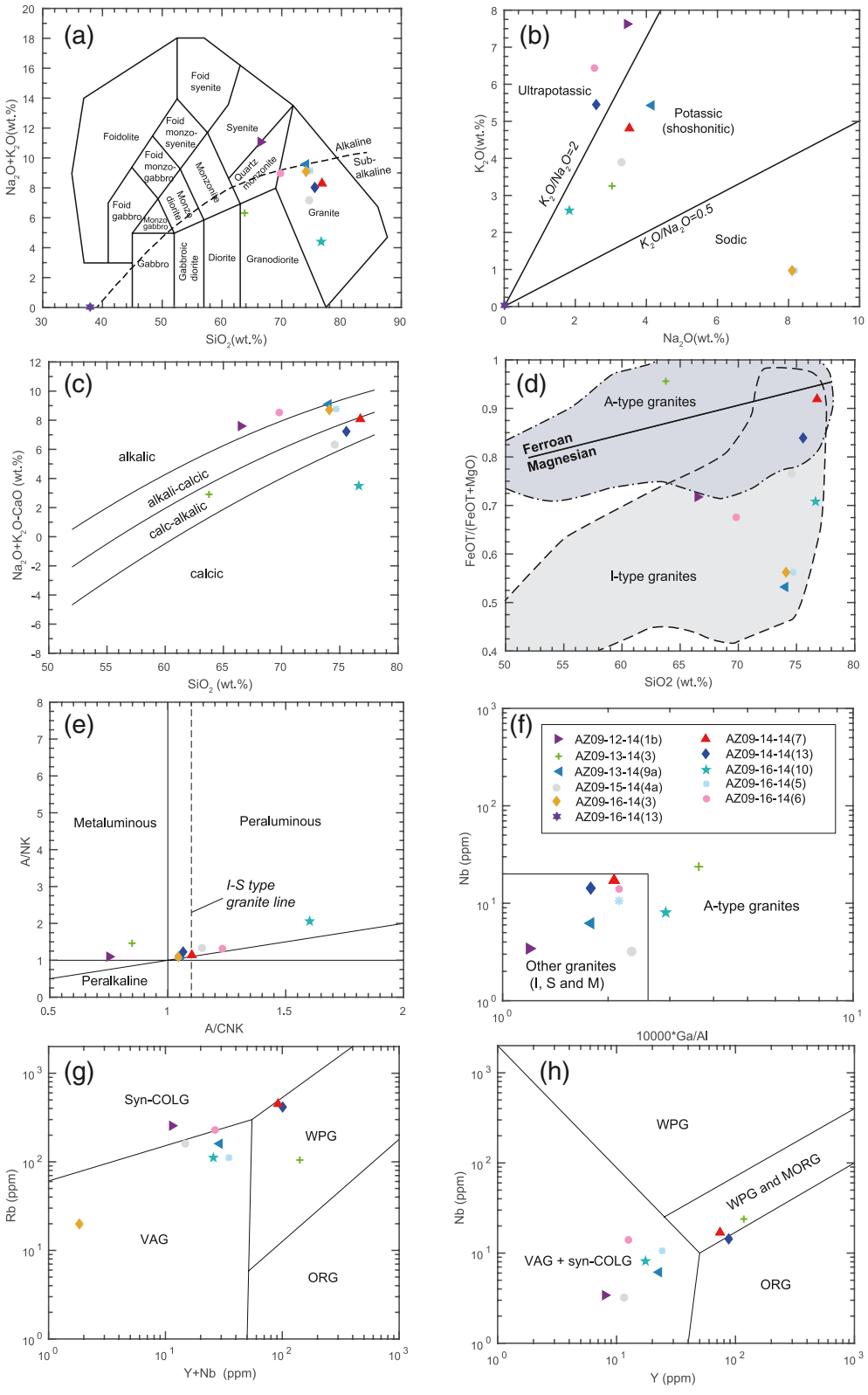
(a)
Foid syenite
Foidolite
Foid monzo-syenite
Syenite
Foid monzo-gabbro
Monzonite
Quartz monzonite
Alkaline
Sub-alkaline
Foid gabbro
Monzo diorite
Monzo gabbro
Granite
Gabbro
Gabbroic diorite
Diorite
Granodiorite
Na2O+K2O(wt.%)
SiO2(wt.%)
(b)
Ultrapotassic
Potassic (shoshonitic)
K2O/Na2O=2
K2O/Na2O=0.5
Sodic
K2O(wt.%)
Na2O(wt.%)
(c)
alkalic
alkali-calcic
calc-alkalic
calcic
Na2O+K2O-CaO (wt.%)
SiO2 (wt.%)
(d)
A-type granites
Ferroan
Magnesian
I-type granites
FeOT/(FeOT+MgO)
SiO2 (wt.%)
(e)
Metaluminous
Peraluminous
I-S type granite line
Peralkaline
A/NK
A/CNK
(f)
AZ09-12-14(1b)
AZ09-13-14(3)
AZ09-13-14(9a)
AZ09-15-14(4a)
AZ09-16-14(3)
AZ09-16-14(13)
AZ09-14-14(7)
AZ09-14-14(13)
AZ09-16-14(10)
AZ09-16-14(5)
AZ09-16-14(6)
A-type granites
Other granites (I, S and M)
Nb (ppm)
10000*Ga/Al
(g)
Syn-COLG
WPG
VAG
ORG
Rb (ppm)
Y+Nb (ppm)
(h)
WPG
WPG and MORG
VAG + syn-COLG
ORG
Nb (ppm)
Y (ppm)

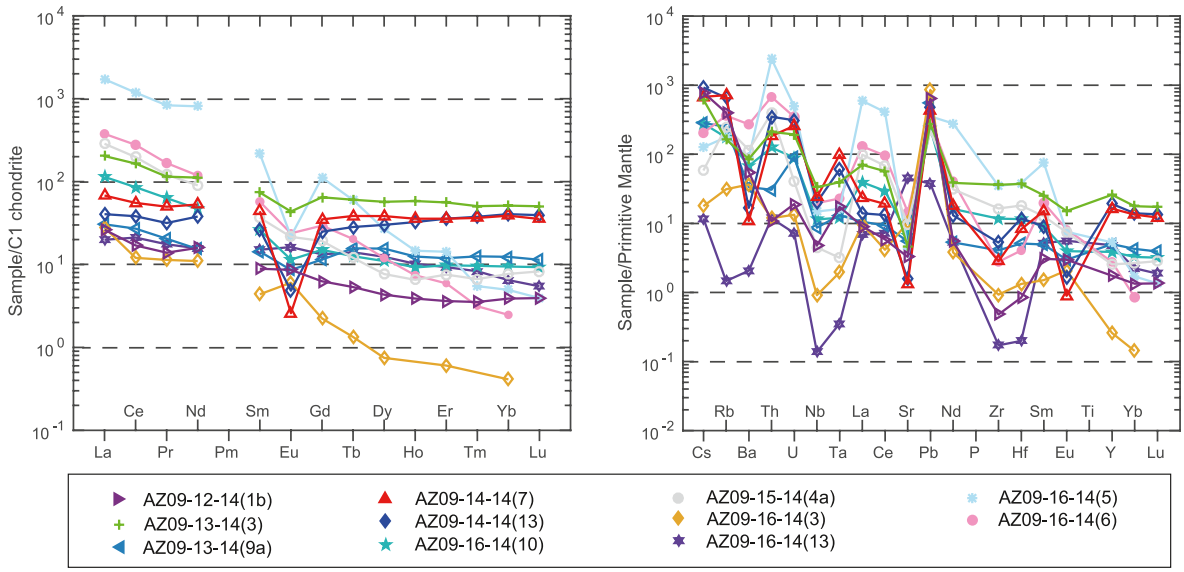

Figure 11. (a) Primitive mantle-normalized trace element variation diagram for the analyzed granitoids (Sun & McDonough, 1989). (b) Chondrite-normalized rare earth element diagram for the analyzed granitoids (Boynton, 1984).

eter using the methods of Norrish and Chappel (1977); analysis precision is estimated to be ~0.5% for SiO_2 and 3%–7% for other oxides. Trace elements were measured on an inductively coupled plasma-mass spectrometry (ICP-MS) following procedures outlined in Dulski (1994); uncertainties were estimated to be better than 5%. Complete detailed methods can be found in the supporting information. All geochemical data is presented in Table S2, and is plotted in Figures 10–12. We use discrimination diagrams to evaluate the tectonic setting our own igneous samples (e.g., Eby, 1990, 1992; Pearce, 1996; Pearce et al., 1984; S. P. Turner et al., 1992; Whalen et al., 1987), but note that these classifications schemes can be problematic (Snow, 2006). Thus, the tectonic interpretations based on our geochemistry results are tentative, and we further consider the samples' ages and geologic setting when incorporating this data into our final tectonic model.

We analyzed a total of 15 samples for their geochemistry, including 11 plutonic and meta-plutonic samples and 4 volcanic and meta-volcanic samples. All plutonic samples have relatively high silica concentrations (SiO_2 > ~65 wt%) and are classified on a Na_2O + K_2O versus SiO_2 total alkali-silica (TAS) plot as quartz monzonite, granodiorite, and granite (Figure 10a) (Middlemost, 1994), and generally belong to the subalkaline series in the total alkalis versus silica (TAS) diagram (Figure 10a) with the exception of sample AZ09-12-14 (1b). Most samples span the potassium and ultrapotassic series, with the exception of sodic samples AZ 09-16-14 (3) and AZ 09-16-14 (5) (Figure 10b) (Le Maitre et al., 1989; Rickwood, 1989), whereas all the samples fall in calc-alkalic to alkalic series in the alkali-lime index plot (Figure 10c) with the exception of sample AZ09-16-2014 (10). The rocks show variable, but generally high, $Mg^{\#}$ values (28.9–62.3) (Figure 10d; Table S2), with an exception of sample AZ09-13-14 (3) showing a ferroan-rich character ($Mg^{\#}$ value of 9.8) (Figure 10d; Table S2). Almost all samples are peraluminous with A/CNK values varying from 1.4 to 1.7, whereas samples AZ 09-12-14 (1b) and AZ 09-13-14 (3) are metaluminous with A/CNK values varying from 1.0 to 1.3 (Figure 10e; Table S2).

All plutonic rocks plot in the I- and S-type granite fields, associated with arc magmatism and/or crustal anataxis, in the (10,000×Ga/Al)-Nb discrimination diagram, with the exception of samples AZ 09-13-14 (3) and AZ 09-16-14 (10) (Eby, 1990, 1992; Pearce, 1996; Pearce et al., 1984; S. P. Turner et al., 1992; Whalen

Figure 10. (a) SiO_2-(K_2O + Na_2O) (TAS, total alkali vs. silica) diagram for plutonic samples. Normalization values are from Middlemost (1994). (b) K_2O versus Na_2O diagram with fields from Peccerillo and Taylor (1976). (c) (b) Na_2O + K_2O – CaO versus SiO_2 diagram, showing the approximate ranges for alkalic, alkalic-calcic, calcic-alkalic and calcic rock series after Frost et al. (2001). (d) TFeO/(TFeO + MgO) versus SiO_2 diagram, showing the approximate ranges for ferroan and magnesian series. The general fields for I- and A-type granites are from the compilations of Frost et al. (2001). (e) Chemical compositions of the samples in terms of Al saturation of Frost et al. (2001). (f) 1,000*Ga/Al versus Nb diagram to distinguish A-type from S- and I-type granitoids (Whalen et al., 1987). (g)-(h) Plutonic rock discrimination diagrams of Pearce et al. (1984).

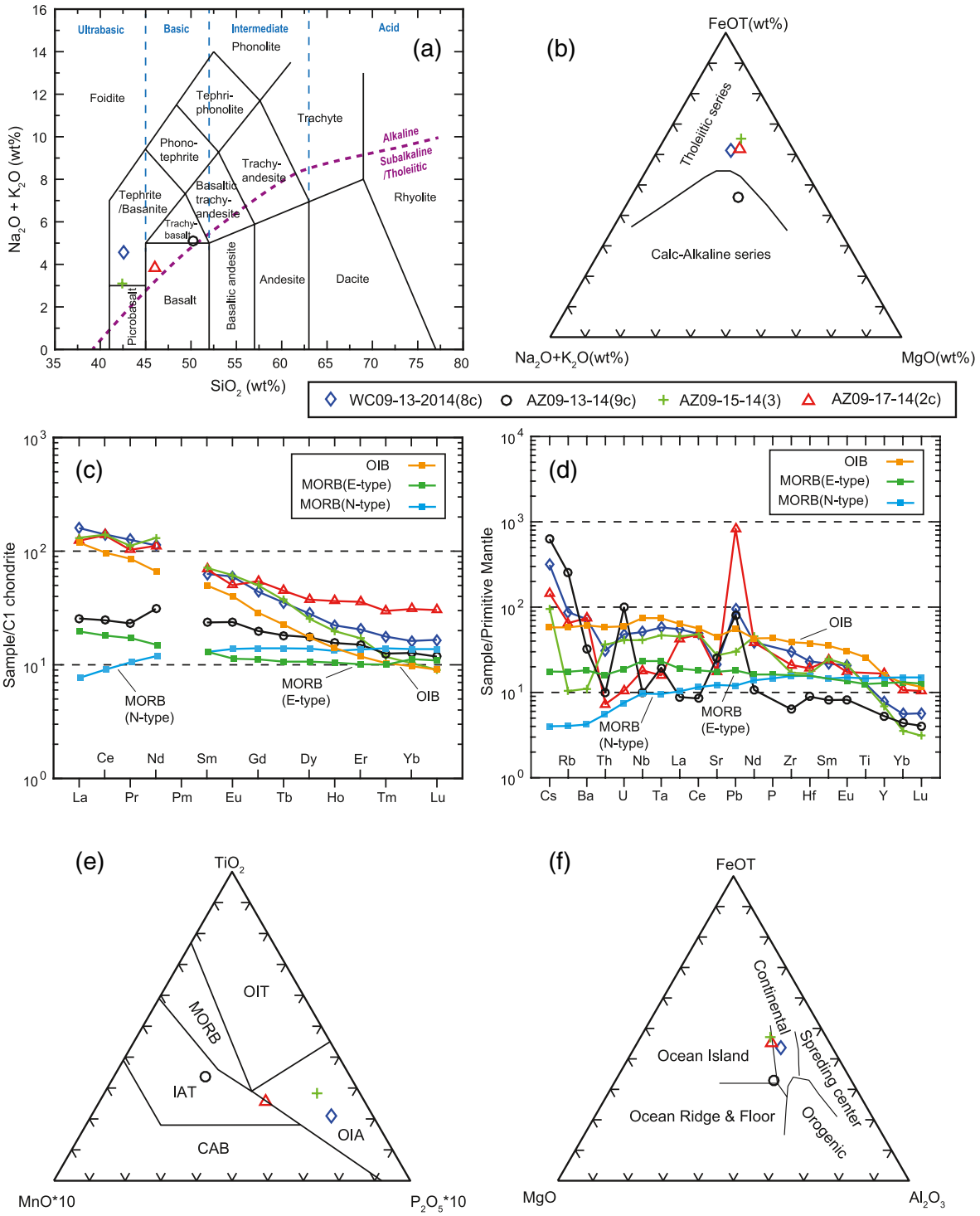

Figure 12. (a) SiO_2-(K_2O + Na_2O) (TAS, total alkali vs. silica) diagram for the volcanic samples. Normalization values are from Le Bas et al. (1986). (b) AFM diagram for the volcanic samples; A = K_2O + Na_2O; F = Fe_2O_3 + FeO; M = MgO. Curve for calc-alkaline and thoeliitic division is from Kuno (1968). (c) Chondrite-normalized rare earth element (REE) diagram for the volcanic samples (Boynton, 1984). (d) Primitive mantle-normalized spider diagram for the volcanic samples (Sun & McDonough, 1989).

et al., 1987) (Figure 10f). These two samples plot in the A-type granite field (Figure 10f), which is generally associated with extension regardless of the origin of the magma source (e.g., Eby, 1990, 1992; S. P. Turner et al., 1992; Whalen et al., 1987). Samples AZ 09-14-14 (7) and AZ 09-14-14 (13) straddle the A-type

and I-type boundaries (Figures 10d and 10f). Additional discrimination diagrams (Pearce, 1996; Pearce et al., 1984) allow for further classification of the analyzed plutonic rocks (Figures 10g and 10h). Most samples plot in the syn-collisional and volcanic arc fields, samples AZ 09-14-14 (7) and AZ 09-14-14 (13) straddle the syn-collisional and within-plate boundaries, and sample AZ 09-13-14 (3) (i.e., the A-type granodiorite) plots entirely within the within-plate granite fields (Figures 10g and 10h). Of note, leucogranite sample AZ 09-12-14 (1b) is the only sample that distinctly plots in the syn-collisional field on the Rb versus Y + Nb discrimination diagram (Figure 10g).

In a multielement diagram normalized to primitive-mantle compositions (Sun & McDonough, 1989), all samples show strong negative Nb anomalies, positive Pb anomalies, and negative Ti anomalies (Figure 11a). The samples generally show enrichment in large ion lithophile elements (LILEs) and depletion in high field strength elements (HFSEs) (Figure 11a). The rare earth element (REE) abundances normalized by chondrite values (Sun & McDonough, 1989) reveal that all samples are generally enriched in light rare-earth element (LREE) and flat heavy rare-earth element (HREE) profiles without distinct Ce anomalies (Figure 11b). Most samples display a prominent negative Eu anomaly, with the exception of samples AZ 09-13-14 (3) and AZ 09-12-14 (1b) (Figure 11b). This anomaly is commonly associated with removal of plagioclase from felsic melts during crystal fractionation (e.g., Rollinson, 2014).

Four volcanic samples with SiO_2, MgO, and Al_2O_3 contents of 42.5–50.3 wt%, 5.2–6.6 wt%, and 12.1–14.8 wt%, respectively, can be classified as basaltic trachy-andesite (AZ 09-13-14 [9c]), basalt (AZ 09-17-14 [2c]), and tephrite basanites (AZ 09-15-14 [3] and WC 09-13-2014 [8c]) on a $Na_2O + K_2O$ versus SiO_2 TAS plot (Figure 12a) (Le Maitre et al., 1989). All four samples follow a calc-alkaline trend (Figure 12b) (Arculus, 2003; Irvine & Baragar, 1971; Kuno, 1968; Le Maitre et al., 1989). The more mafic samples (i.e., AZ 09-15-14 [3], WC 09-13-2014 [8c], and AZ 09-17-14 [2c]) have relatively high total REE concentrations, especially are enriched in light rare earth elements (LREE), similar with OIB type (Figure 12c). The intermediate sample AZ 09-13-14 (9c) has a relatively flat REE chondrite-normalized profile (Figure 12c), whereas the E-MORB rock display slight to significant LREE depletion, similar with N-MORB (Figure 12c). All these samples show very slight to no Eu negative anomalies ($\delta Eu = 0.27–0.37$; Figures 12c and 12d, and Table S2). On a Primitive Mantle-normalized diagram, these more mafic three samples generally display enrichment in LILE and Pb, and show no Nb and Ta anomalies (Figure 12d). Similarly, the intermediate sample AZ 09-13-14 (9c) also shows LILE enrichment and Pb, but relatively enriched in U and slightly negative Nb and Ta anomalies (Figure 12d). The more mafic samples are plotted into the field of OIA, whereas the intermediate sample AZ 09-13-14 (9c) is plotted into the field of IAT in the TiO_2-MnO*10-P_2O_5*10 diagram (Figure 12e). All these samples follow an "Ocean Island" trend with an exception of the intermediate sample AZ 09-13-14 (9c) placing between the "Ocean Island" and "Ocean Ridge & Floor" fields in the FeO^T-MgO-Al_2O_3 diagram (Figure 12f).

5. Discussion

5.1. Construction of a Tectonostratigraphic Framework

Our geochronological studies, together with the field observations, focused on the U-Pb zircon ages of the Paleoproterozoic-Paleozoic metamorphic sedimentary and volcanic rocks, key leucogranites and intrusions, and the structural contacts among these units between the North China and Kunlun-Qaidam continents. New geochemistry analyses helped better constrain the tectonic setting and arc-continent evolution of this region. Below we describe the important structural, geochemical, and geochronological observations and their correlation with existing knowledge in the literature allow us to construct a tectonostratigraphic section that constrains the evolution of the southwestern margin of North China craton and northern margin of Kunlun-Qaidam continent (Figure 13a).

5.1.1. Proterozoic Rocks

We observed at least two distinct units of Proterozoic strata across the regional study area. The youngest single concordant zircon from leucogranite sample AZ 09-12-14 (1c) yielded an age of 1,496 ± 25 Ma (Figure 8a), which provides a minimum age for the Proterozoic gneissic rocks that the leucogranite cuts. We note that this single zircon age is not robust, and alternatively the 1.8–1.9 Ga (i.e., concordant age of

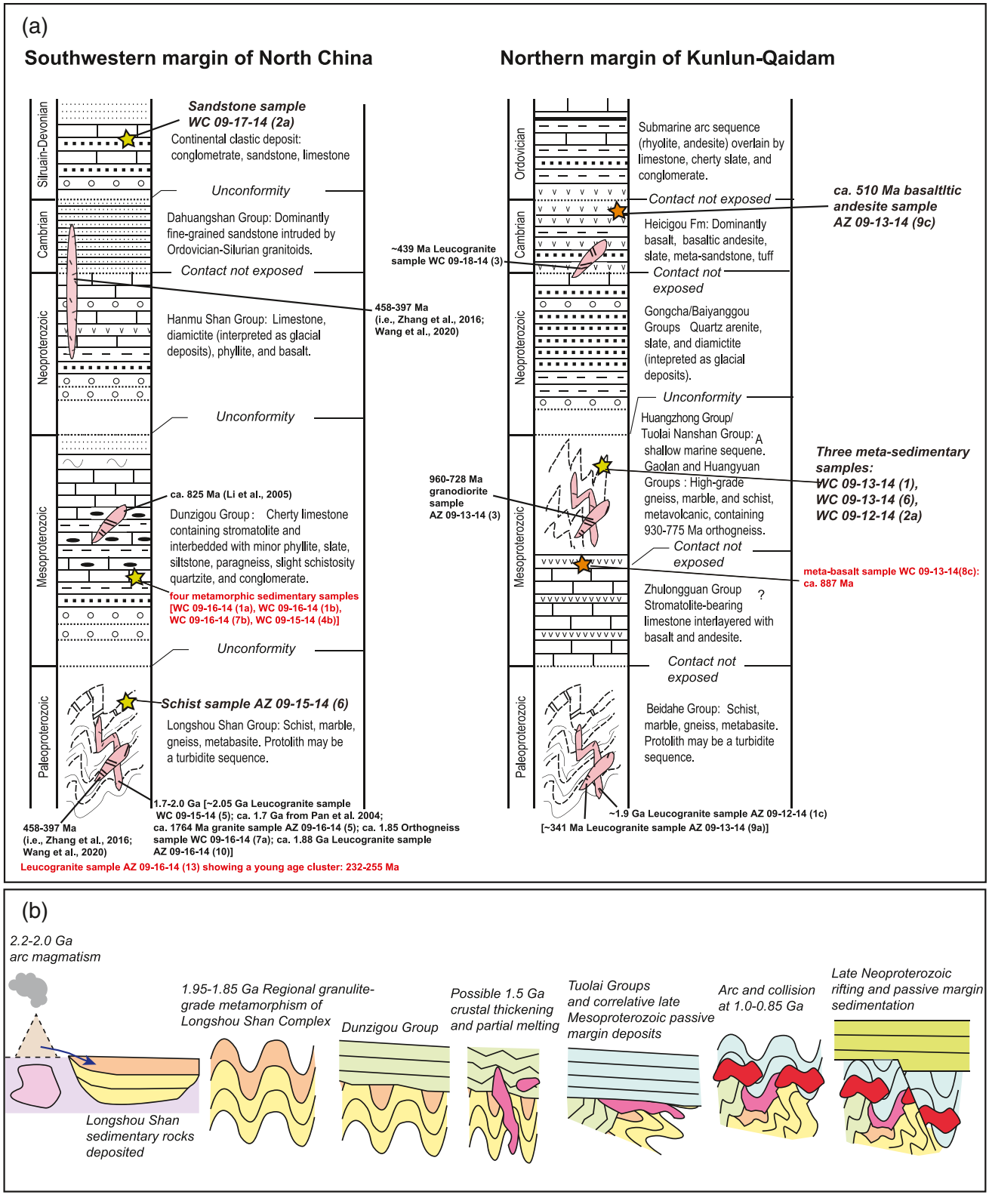

Figure 13. (a) Tectono-stratigraphic sections of the Longshou Shan and the eastern Qilian Shan, key references used for constructing these sections include: Pan et al. (2004), Li et al. (2005), Qinghai BGMR (1991), Gong et al. (2016), and Zhang et al. (2016); (b) schematic representation of the key tectonic relationships of samples and strata from the eastern Qilian Shan and Longshou Shan from the Mesoproterozoic to the Neoproterozoic.

1,908 ± 20 Ma; Figure 8a) zircon-age population from the leucogranite provides a more conservative minimum age for the Proterozoic gneiss. Geochemistry data suggests that the leucogranite is syn-collisional, and it probably was generated during orogen-related crustal melting (e.g., Noble & Searle, 1995) in the Mesoproterozoic (i.e., ca. 1.5 Ga). The Proterozoic gneiss is juxtaposed via a thrust contact over a meta-quartzite unit that yields detrital zircon ages spanning the Proterozoic (i.e., sample AZ 09-12-14 [2a]) (Figure 8l). The youngest three zircon ages suggest that the maximum depositional age of this quartzite was ca. 1.14 Ga (Figure 8l). We note that the detrital zircon age spectrum from this sample is very similar to other Mesoproterozoic rocks in the central Qilian Shan (e.g., G. E. Gehrels et al., 2003a; C. Wu et al., 2017; Zuza et al., 2018) (Figure 9). All four samples contain a youngest zircon population of ca. 1.15–1.25 Ga, distinct 1.4–1.5 Ga ages, and Paleoproterozoic to Archean zircons (except for Gehrels et al., 2003a sample GA206, which only had a total of 22 zircon analyses) (Figure 9). In addition, the Mesoproterozoic samples from Gehrels et al. (2003a), Wu et al. (2017), and Zuza et al. (2018) were all intruded by 900–950 Ma granitoids (Figure 9), which constrains their depositional ages between ca. 0.95 Ga and ca. 1.15 Ga. We assume that sample AZ 09-12-14 (2a) from this study was deposited in a similar timeframe, although we do not directly observe the cross-cutting ca. 0.95 Ga intrusions in this study of the eastern Qilian Shan.

The Proterozoic gneiss was thrust over the younger Mesoproterozoic quartzite (Figure 4a). The age of this thrusting is unconstrained, but the complete lack of a topographic expression of this fault suggests it probably occurred prior to the Cenozoic. Future thermochronology and cooling-history analysis of the thrust fault's hanging wall may better constrain the age of thrusting, but for now, we posit that thrusting may have occurred either in the early Paleozoic during the Qilian orogeny or during the early Neoproterozoic related to the enigmatic 0.9–1.0 Ga magmatic event (e.g., C. Wu et al., 2016a, 2017; Zuza & Yin, 2017).

About 80 km to the northwest, the same meta-quartzite unit (e.g., Pan et al., 2004, Figure 3) is intruded by foliated ca. 728 Ma granodiorite (sample AZ 09-13-14 [3]) (Figure 8b) that has an A-type within-plate geochemical signature (Figure 10), which probably indicates that the intrusion was generated in an extensional setting (Eby, 1990, 1992; S. P. Turner et al., 1992; Whalen et al., 1987). Wu et al. (2017) reported ca. 820 Ma extension-related A-type granitoids in the Qilian Shan that preceded continental rifting the opening of the Neoproterozoic-early Paleozoic Qilian orogen. The igneous rock is strongly foliated and folded with the quartzite rock (sample WC 09-13-14 [1]) that it intrudes, and older inherited zircons record Qilian enigmatic ca. 960 Ma tectonic event (e.g., G. E. Gehrels et al., 2003a; C. Wu et al., 2016a, 2017; Zuza & Yin, 2017) (Figure 8b). Thus, we suggest that the granodiorite intruded the quartzite, after ca. 1.19 Ga (i.e., the maximum depositional age) (Figure 8n), during an episode of regional extension, and was later deformed with the quartzite during contractional deformation, possibly related to the early Paleozoic Qilian orogen. Another phyllite sample WC 09-13-14 (6) was also collected from the Mesoproterozoic strata, together with the quartzite sample WC 09-13-14 (1) and above meta-quartzite sample AZ 09-12-14 (2a), show the similar age populations to other Mesoproterozoic rocks in the Qilian Shan as discussed above (e.g., G. E. Gehrels et al., 2003a; C. Wu et al., 2017; Zuza et al., 2018).

The youngest single concordant zircon from OIB-like type meta-basalt sample WC 09-13-14 (8c) yielded an age of ca. 887 Ma (Figures 8c and 12). The basalt was interbedded with Meso-to Neoproterozoic marble layers, and we therefore interpret that this rock unit was part of a Neoproterozoic rift and drift basin developed in the eastern Qilian Shan. Alternatively, if the meta-basalt is ca. 1.2 Ga, using the next youngest population of grains (Figure 8c), this unit could be interpreted as Mesoproterozoic in age.

Proterozoic strata in the Longshou Shan have been divided into the Paleoproterozoic Longshou Shan Group (or Complex), the Mesoproterozoic Dunzigou Group, and the Neoproterozoic Hanmushan Group (J. Gong et al., 2016; J. H. Gong et al., 2013). We analyzed detrital zircons from one Longshou Shan Group quartzite sample: AZ 09-15-14 (6) (Figure 9). Here we discuss these ages with additional ages from adjacent samples presented by Gong et al. (2016) (inset of Figure 9). Most samples have dominant age peaks ca. 1.9 and 2.1 Ga peaks and various minor older Paleoproterozoic zircon grains. Gong et al. (2016) inferred that the ca. 1.85 Ga zircon grains were metamorphic zircons, and our new age data support this inference; older >1.95 Ga zircon ages generally have Th/U ratios >0.15 whereas most of the younger <1.95 Ga grains have lower <0.15 Th/U ratios (Table S2). The shallow marine sediments of the Longshou Shan Group were suggested to have

been deposited between ca. 2.0–1.95 Ga (e.g., J. Gong et al., 2016; Pan et al., 2004; Xu et al., 2014; this study). However, our field observation shows that Paleoproterozoic (i.e., ca. 2.05 Ga) leucogranite dike intrudes into the Longshou Shan Group quartzite unit (Figure 7d), so we further constrain that the deposition age of the Longshou Shan Group should older than ca. 2.05 Ga. In additional, a 2.2–2.0 Ga magmatic arc may have developed in the Longshou Shan area (e.g., Fan et al., 2010; Dan, Li, Guo, Liu, & Wang, 2012; C. Y. Dong et al., 2007; J. Gong et al., 2016; Li et al., 2004; H. C. Wang et al., 1999; C. Wu et al., 2018; ca. 2.05 Ga leucogranite sample WC 09-15-14 [5] in this study), and Lu-Hf isotopes showed reworking of older crust, i.e., ca. 2.45–2.65 Ga basement of the North China (J. Gong et al., 2016; C. Wu et al., 2018). The entire Longshou Shan Group/complex was metamorphosed ca. 1.92–1.85 Ga (i.e., ca. 1.88 Ga A-type leucogranite sample AZ 09-16-14 [10] and ca. 1.85 Ga orthogneiss sample WC 09-16-14 [7a]), which is consistent with the reported tectonothermal events in the northern margin of the North China Craton (i.e., S. X. Han et al., 2020; Kusky & Li, 2003; Kusky et al., 2007, 2016; Wan, Windley, Xiao, Feng, & Zhang, 2015; C. Wu et al., 2018). Meso- to Neoproterozoic continental and/or passive margin deposits were deposited on top following orogeny, such as the Bayan Obo Group in the northern North China and Tuolai Group in the Qilian Shan (e.g., C. Wu et al., 2017, 2018; Zhou et al., 2018; A. V. Zuza et al., 2018).

The overlying Mesoproterozoic Dunzigou Group has been interpreted to be composed of unmetamorphosed sedimentary strata including conglomerate, limestone, and sandstone. However, our field observations suggest that these rocks have been transformed to phyllite, paraschist, quartzite, and bedding is often transposed by penetrative cleavage (Figure 7f). The strata are intruded by leucogranite and folded together. The nearby ca. 825 Ma Jinchuan intrusion, and related dikes, do not show signs of such foliation development and deformation (Figure 7j). Thus, our observations suggest that the Dunzigou Group was deformed between the Mesoproterozoic and ca. 825 Ma, possibly during the 1.0–0.9 Ga inferred orogen. We analyzed detrital zircons from four Dunzigou Group samples: quartzose schist sample WC 09-15-14 (4b), quartzite sample WC 09-16-14 (1a), quartzose schist sample WC 09-16-14 (1b), and paragneiss sample WC 09-16-14 (7b). These samples yielded dominant age peaks of ca. 1.85, 1.9, and 2.1 Ga and various minor younger Late Paleoproterozoic zircon grains (i.e., ca. 1.76–1.82 Ga). The younger zircon age population are widely distributed in North China, which are interpreted as being generated in an extensional setting (e.g., S. X. Han et al., 2020; P. Peng et al., 2008; granitoid sample AZ 09-16-14 [5] in this study) (Figure 10). The OIB-like mafic sample AZ 09-15-14 (3) was interbedded within the Neoproterozoic Hanmushan Group limestone layer, which probably indicates that Neoproterozoic rift-basin development in eastern Longshou Shan. The detrital zircon age populations of a meta-sandstone sample from the Hanmushan Group (Song et al., 2017; Figure 10) are similar to Qilian Shan Neoproterozoic sample GA209 from G. E. Gehrels et al. (2003a) (Figure 10).

5.1.2. Paleozoic Rocks

Near Menyuan city, lower Paleozoic slightly metamorphosed interbedded marbles and ca. 512 Ma meta-basaltic trachy-andesite (i.e., sample AZ 09-13-14 [9c]; Figure 8d) are crosscut by a leucogranite (i.e., sample AZ 09-13-14 [9a]). The volcanic rocks were mostly likely derived as part of the Cambrian Qilian arc. Interpretation of the crosscutting leucogranite is less straightforward due to its spread of Paleozoic zircon ages (Figure 8c). The youngest population of truly concordant analyses yields a weighted mean age of ca. 341 Ma, which implies that this leucogranite may have been generated from crustal melts in the latest Devonian-Carboniferous during the Qilian orogen (Figure 8c) (e.g., S. Song et al., 2013, 2014; C. Wu et al., 2017). This age may be too young for the Qilian orogen because by Carboniferous shallow marine sediments overly much of northern Tibet, suggesting that orogeny was complete by this time (A. V. Zuza et al., 2018). Alternatively, the younger, slightly discordant analyses from this sample are Permian in age, which would suggest that this leucogranite was generated during the Permian closure of the Paleo-Asian Ocean to the north (W. Xiao et al., 2003). Either way, a phase of Paleozoic anatexis appeared to have occurred in response to Paleozoic orogeny, generating leucogranite with complex zircon populations in the eastern Qilian Shan.

Early Paleozoic granites from the Haiyuan-fault restraining bend yield a U-Pb zircon age of ca. 460 Ma (sample AZ 09-14-14 [8]) (Zuza et al., 2018), together with a ca. 439 Ma leucogranite to the east (sample WC 09-18-14 [3]), which both intruded the Lower Paleozoic forearc strata (Figures 4 and 6). Our geochemistry characteristics from arc magmatism samples AZ 09-14-14 (7) and AZ 09-14-14 (13) supports the interpreta-

tion of northward slab rollback at the south-dipping Qilian arc subduction zone (Zuza et al., 2018). Paleozoic molasse deposition in Longshou Shan mainly occurs near Shandan city (Figure 4), our sandstone sample WC 09-17-14 (2a) has dominant age peaks ca. 1.7, 0.9 and 0.5 Ga peaks and the maximum depositional age of ca. 406 Ma. The two younger age populations are widely distributed in Qilian Shan and Longshou Shan, whereas the older age peak is widely distributed in North China-Tarim and Longshou Shan. We further suggest that the linkage again between the Qilian Shan and North China-Tarim corresponds to this time period.

5.2. Proterozoic Tectonic Configuration

Here, we first discuss a possible Proterozoic linkage between the North Tarim and North China continents. Permo-Triassic closure of the Paleo-Asian Ocean against their northern margins is broadly similar along strike (e.g., Windley et al., 1990; W. Xiao et al., 2003; Zuza & Yin, 2017), thus supporting their connection by the late Paleozoic. The early Paleozoic Qilian orogen affected both the southern margin of North China (e.g., S. Song et al., 2013; A. V. Zuza et al., 2018) and northern Tarim Basin, as evidenced by observations of an Ordovician-Silurian fold-thrust belt in the subsurface (e.g., Jia, 1997; Carroll et al., 2001; Yin & Nie, 1996) and early Paleozoic thermal pulses (e.g., P. Yang et al., 2020). Therefore, North China and North Tarim were contiguous at the start of the Paleozoic. Expanding on these lines of evidence, we suggest that Tarim and North China were linked in the Proterozoic time, and the belt of 1.0–0.9 Ga plutonic rocks stretching from the Tian Shan, through Tarim, to the Kunlun-Qaidam continent (Figure 1b) supports this was a continuous margin for Neoproterozoic subduction and arc magmatism. Without evidence for a Paleozoic-Mesozoic arc-subduction system between North China and Tarim and a reasonable explanation to resolve the aforementioned lines of evidence, we argue that models of their separation in the Phanerozoic are unjustified.

The detrital zircon spectra of samples from Tarim, Kunlun-Qaidam, and North China can be used to test a possible Proterozoic linkage between these continents. Mesoproterozoic quartzite and schist samples from these locations are remarkably similar (Figure 9; G. E. Gehrels et al., 2003a; J. Gong et al., 2016; S. Lu et al., 2008; Y. L. Li, Xiao et al., 2020; C. F. Liu et al., 2018; Peng et al., 2019; D. F. Song et al., 2017; K. Tung et al., 2007, 2012, 2013; Y. Wan et al., 2006; C. Wu et al., 2017; Yu et al., 2013; A. V. Zuza et al., 2018; this study): (1) Paleoproterozoic-Archean zircons (except for G. E. Gehrels et al., 2003a sample GA206), (2) dominant ca. 1.4–1.5 Ga zircon grains, (3) youngest zircon age populations of ca. 1.15–1.25 Ga, and (4) intrusions by 0.90–0.95 Ga granitoids. These resemblances highlight that the regionally widespread strata are of comparable ages (i.e., late Mesoproterozoic to early Neoproterozoic) and received sediments from broadly similar sources. Although the exact shape of the detrital zircon spectrum (i.e., the proportion of particular age populations) from each sample varies (Figure 9), these minor variations may be caused by variations in the individual drainage systems (e.g., Teng et al., 2020; C. L. Zhang et al., 2016, 2019). We acknowledge that detrital zircon correlations offer nonunique solutions, as many of these age signatures are important globally. However, these observations make our proposed North Tarim and North China correlation from the Archean to early Neoproterozoic permissible. The Kunlun-Qaidam microcontinent may have been partially or completely rifted away from combined North China-Tarim as a result of the opening of the Qilian ocean in the late Neoproterozoic (i.e., Yin & Harrison, 2000; C. Wu et al., 2016a, 2017; A. V. Zuza et al., 2018).

The early Paleozoic suture zone classically separates the Kunlun-Qaidam continent from the North China craton (e.g., Song et al., 2005; X. -Y. Song et al., 2006; S. Song et al. 2013; Yang et al., 2001; A. V. Zuza et al., 2018). The existence of this suture zone, and a contemporaneous-to-slightly-older arc system, is clear evidence that Kunlun-Qaidam continent collided with North China craton. This separation allows for ambiguity for the pre-suturing connection between Kunlun-Qaidam continent and North China craton, but also highlights how such a suture-arc belt is both (1) required to join continental fragments and (2) observable in the geologic record (see related discussion in A. V. Zuza & Yin, 2017). Therefore, the lack of identified suture-arc rocks separating northern Tarim and North China cratons makes their separation from the middle Proterozoic to present highly unlikely. In addition to the geologic similarities between the continents, their geologic history, and the sediments deposited over them, the lack of intervening suture complexes is a strong argument for their contiguous nature.

We note here that many of our samples from the southwestern margin of North China craton and northern margin of Kunlun-Qaidam continent contain detrital or inherited Paleoproterozoic and Archean zircon grains (Figures 7 and 9) (J. Gong et al., 2016; D. F. Song et al., 2017; C. Wu et al., 2017; A. V. Zuza et al., 2018; this study). For igneous samples, this suggests that the zircon-host plutons intruded through Archean-Paleoproterozoic crust, and for detrital metasedimentary samples, this suggests that there was Archean basement in the source region or sedimentary rocks with recycled Archean zircons. Although no Archean basement has been confirmed for the Qilian Shan and Longshou Shan, the detrital or inherited information improve the possibility for the Archean source basement. Four phases of Paleoproterozoic tectono-magmatic activity occurred in the Longshou Shan as observed via our geochronology and geochemistry analysis. This sequence of events is similar to what has been documented along the northern margin of the North China craton, including ca. 2.0 Ga arc, 1.88 and 1.85 Ga metamorphic, and 1.76 Ga extension events (e.g., J. Gong et al., 2016; S. X. Han et al., 2020; Kusky et al., 2016; C. Wu et al., 2018). The rock assemblages and age populations of the Mesoproterozoic Dunzigou Group in Longshou Shan and Qilian correlative strata are similar to coeval units in the northern margin of the North China craton (e.g., C. Wu et al., 2017; A. V. Zuza et al., 2018; Zhou et al., 2018; this study). The 1.0–0.9 Ga granitoid belt that is exposed throughout Qaidam, the Qilian Shan, and Tarim, also has sparse exposures in northern North China craton (Cowgill et al., 2003; G. E. Gehrels et al., 2003b; P. Peng et al., 2008; S. Song et al., 2013; K. Tung et al., 2007; C. Wu et al., 2016a, 2017, A. V. Zuza et al., 2018; this study). Leucogranites and metamorphic zircons have been reported with ages of ca. 0.9–0.85 Ga in the Tarim continent and Qilian Shan (G. E. Gehrels et al., 2003b; Kröner et al., 2013; H. Wang et al., 2014; C. Wu et al., 2017; Zhu et al., 2011; A. V. Zuza et al., 2018).

We document a ca. 887 Ma OIB-like basalt unit (sample WC 09-13-14 [8c]) in the eastern Qilian Shan. The ca. 825 Ma Jinchuan ultramafic intrusion (Li et al., 2005) and the Neoproterozoic Hanmushan Group passive margin deposition may have been associated with the opening of the Paleo-Asian Ocean, and A-type ca. 820 Ma granitoids in the Qilian Shan have been related to postorogenic extension (C. Wu et al., 2017; A. V. Zuza et al., 2018). Our ca. 728 Ma granodiorite in the eastern Qilian Shan may similarly been associated with the opening of the Qilian Ocean.

5.3. Early Paleozoic Geology in the Qilian Shan and Longshou Shan

The Qilian arc was active on the northern margin of the Kunlun-Qaidam continent during most of the Ordovician (D. Fu et al., 2019; C. L. Fu et al., 2018; C. Wu, Yin et al., 2016; C. Wu, Liu et al., 2016; C. Wu et al., 2017; Yan et al., 2019; A. V. Zuza et al., 2018). The nature of this subduction system and arc, including subduction polarity (i.e., north or south dipping), has been debated (e.g., D. Fu et al., 2019; S. Song et al., 2013; Xiao, Windley, Yuan et al., 2009; Xiao, Windley, Huang et al., 2009; Xiao, Windley, Yong et al., 2009; Yan et al., 2019; Yin, Dang et al., 2007; Yin, Manning et al., 2007; Zuza et al., 2018). Partly based on the prevalence of Ordovician arc granites throughout Qaidam, and the general lack of these plutons in the North China craton, Zuza et al. (2018) and Wen et al. (2017) recently presented tectonic models that involve a south-dipping Qilian arc, expanding upon previous suggestions by Sobel and Arnaud (1999) and G. E. Gehrels et al. (2003a, 2003b). In this study, we document an arc-related Cambrian basaltic trachy andesite (i.e., sample AZ 09-13-14 [9c]) near Menyuan that was subsequently intruded by ca. 341 Ma leucogranite (i.e., sample AZ 09-13-14 [9a]) (Figure 4). The location of these samples south of the Qilian suture trace(s) supports that the Cambrian Qilian arc developed within the Kunlun-Qaidam continent. The range of zircon ages in the leucogranites intrusion (Figure 8c) indicates that crustal melting, possibly due to crustal thickening during orogeny or underthrusting of hydrated sediments (e.g., Harrison & Weilicki, 2016), occurred in the Silurian to early Carboniferous. This timing generally corresponds to the protracted deformation during the Qilian orogen, although it is somewhat younger than the main phase of Silurian-Devonian orogeny (e.g., S. Song et al., 2013; Zuza et al., 2018). An alternative interpretation for this sample is that the rare younger zircons better reflect the age of this leucogranite sample, possible as Permo-Triassic crustal melting during closure of the Paleo-Asian Ocean (e.g., W. Xiao et al., 2003). The newly dated ca. 460 Ma arc granites and ca. 439 Ma leucogranite from the east Qilian Shan might have been associated with the subduction of Qilian oceanic crust and initial collision between the Tarim-North China and Kunlun-Qaidam continents, respectively (e.g., C. Wu et al., 2017; A. V. Zuza et al., 2018).

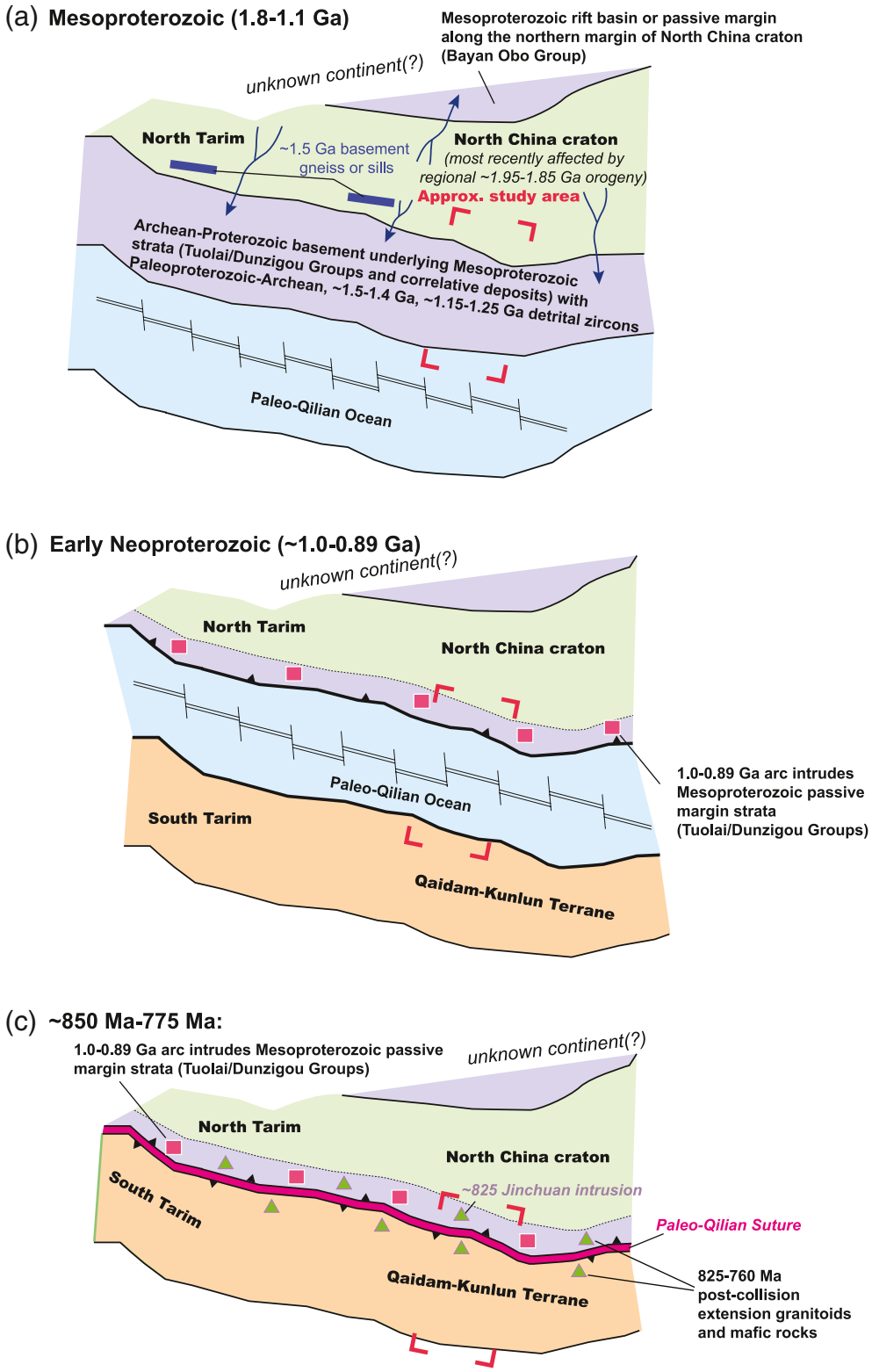

Figure 14. Models for the tectonic evolution of northern Tibet and the Tarim-North China from the Mesoproterozoic through the Silurian, see the text for the details. Note that the scale is relative and changes, adapted from C. Wu et al. (2017).

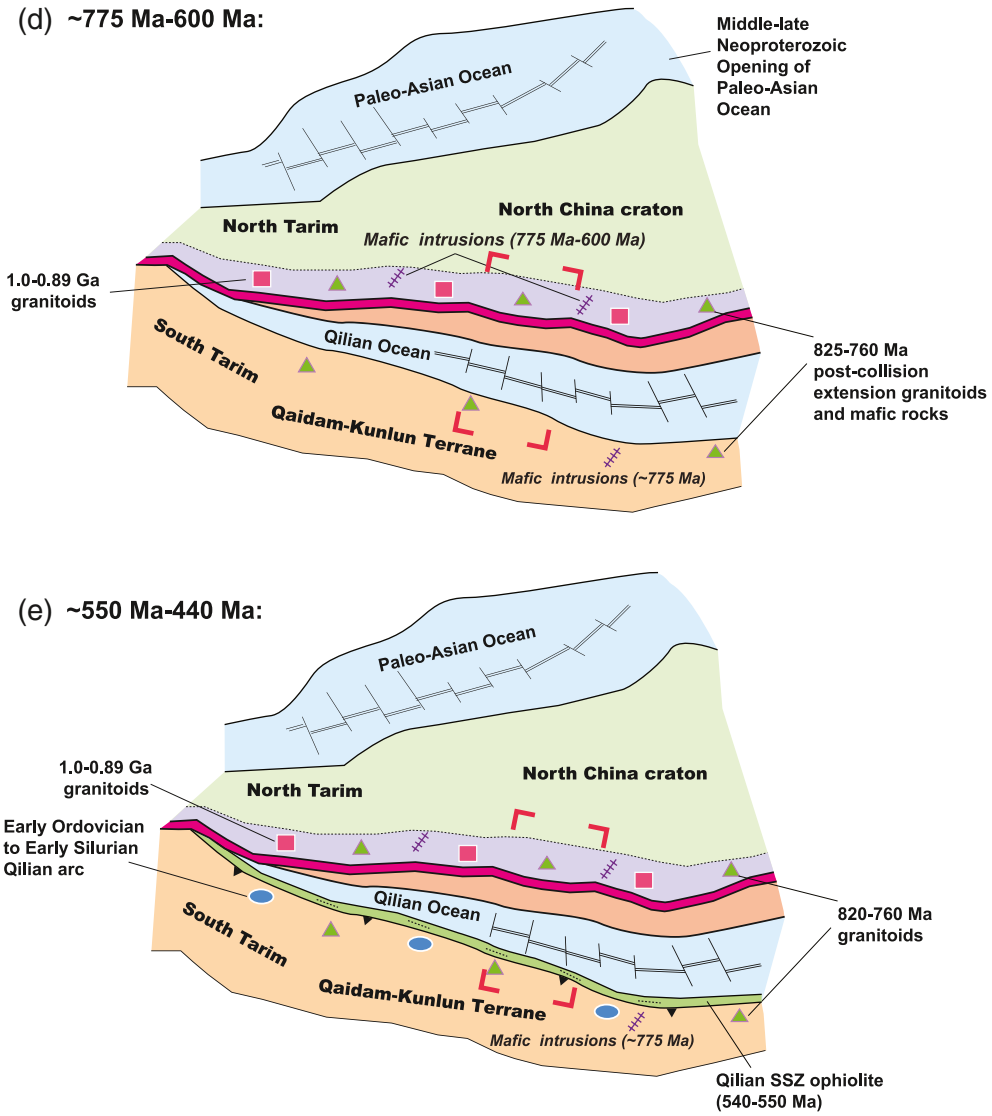

Figure 14. Continued

The lower Paleozoic Dahuangshan Group passive continent margin deposition occurred near Yongchang city, which was unconformity covered by the Devonian molasse sedimentary (e.g., C. L. Zhang et al., 2016). Early Paleozoic igneous rocks in the southern Longshou Shan consist of Silurian-Devonian granitoids (i.e., ca. 440–400 Ma), with some designated A-type granitoids (e.g., Z. Z. Wang et al., 2020). With respect to the early Paleozoic Qilian orogen, these intrusions are syn-to postcollisional (e.g., S. Song et al., 2013; A. V. Zuza et al., 2018) and may reflect crustal melting and/or postcollision extensional magmatism. The detrital zircon age populations from our Devonian sandstone sample in Longshou Shan (i.e., sample WC 09-17-14 [2a]) constrains that the provenance is similar to Qilian Shan, this suggests that the collision between North China and Kunlun-Qaidam continents was completed in this period (e.g., B. Li et al., 2020a).

5.4. Paleoproterozoic-Early Paleozoic Tectonic Evolution of Northern Tibet

Based on the field observations and analytical data presented in this study, we propose the following tectonic model for the Paleoproterozoic to early Paleozoic geologic history of northern Tibet, including the regions around the Qilian Shan, Longshou Shan, and North China (Figures 13b and 14). In the Paleoproterozoic, the protolith sediments of the Longshou Shan Complex were sourced predominately from the

North China craton and deposited along its southwestern margin (Figure 13b). These rocks experienced amphibolite-grade metamorphism during a regional 1.95–1.85 Ga orogenic event that affected much of the North China and Tarim cratons (Figure 13b), with 1.9 Ga and 1.85 Ga metamorphic zircons observed in the Qilian Shan-Qaidam continent. The 1.78–1.75 Ga intraplate extensional tectonic setting is generally considered in much of the North China craton, including Longshou Shan and Kunlun-Qaidam continents (e.g., S. X. Han et al., 2020; Kusky & Li, 2003; S. N. Lu et al., 2006; P. Peng et al., 2008; X. Yu et al., 2017; this study) (Figure 13b). Mesoproterozoic passive continent margin strata deposited along the northern margin of the North China, Longshou Shan, and Qilian Shan (Figures 13b and 14a), which shows the similar detrital zircon age populations, i.e., Tuolai Group in Qilian Shan, Dunzigou Group in Longshou Shan, and Bayan Obo in the northern North China craton (J. Gong et al., 2016; G. E. Gehrels et al., 2003a; C. F. Liu et al., 2018; C. Wu et al., 2017; J. X. Zhang et al., 2013; Zhou et al., 2018; A. V. Zuza et al., 2018) (Figure 14a). These ages are observed in the detrital zircon spectra of Mesoproterozoic strata, and some rocks of these ages are observed, such as sills in North Tarim as part of a poorly exposed large igneous province (LIP) (C. Z. Wu et al., 2014). However, the exact source for the large population of 1.5 Ga zircons remains unclear.

A 1.0–0.9 Ga arc intruded the Mesoproterozoic passive margin deposits widespread in the Qilian Shan and Tarim, potentially during north-dipping subduction, and eventual closure, of the Paleo-Qilian Ocean (e.g., G. E. Gehrels et al., 2003b, 2011; C. F. Liu et al., 2019; C. Wu et al., 2016a, 2017; A. V. Zuza et al., 2018) (Figures 13 and 14b). The configuration and kinematics of this ocean-closure event are poorly resolved. This configuration would involve contiguous South Tarim-Qaidam colliding against North Tarim-North China. A possible ca. 887 Ma rift-basin was developed in the eastern Qilian Shan as evidenced by contemporaneous OIB-like basalt. The opening of the Qilian Ocean was preceded by bimodal volcanism (ca. 830–600 Ma) observed throughout Qaidam, Qilian, and Tarim-North China and the deposition of Neoproterozoic passive margin deposits observed in the northern Qilian Shan (Tseng et al., 2006, 2007; X. Xu et al., 2015; C. Wu et al., 2017; A. V. Zuza et al., 2018) (Figures 13b and 14c). The ca. 825 Ma Jinchuan ultramafic intrusion (X. H. Li et al., 2005) and deposition of Neoproterozoic Hanmushan Group passive-margin strata in Longshou Shan may have been associated with the opening of the Qilian ocean to the south (e.g., C. Wu et al., 2016a; Zuza et al., 2018), and also possible Paleo-Asian Ocean to the north of the North China craton (Figures 13b and 14d).

A Cambrian-middle Ordovician Qilian arc sequence developed along the northern margin of the Qaidam, which suggests a south-dipping subduction of the Qilian oceanic crust (C. F. Liu et al., 2019; C. Wu et al., 2016a, 2017; A. V. Zuza et al., 2018) (Figure 14e). Silurian-Devonian plutonic intrusions along the southern margin of the Longshou Shan may be syn- to postcollisional after the closure of the Qilian Ocean occurred at ca. 445–440 Ma (e.g., C. F. Liu et al., 2019; Zuza et al., 2018) (Figure 14e). Alternatively, early Paleozoic plutons in the Longshou Shan may be evidence for bivergent subduction of the Qilian Ocean (e.g., X. H. Chen et al., 2019; B. Li et al., 2020a). The subsequent Silurian-early Devonian postcollision granitoids, Silurian flysch and Devonian molasse deposits occurred at the Longshou Shan and northern Qilian Shan (D. Fu et al., 2019; Z. Z. Wang et al., 2020; C. Wu, Yin, et al., 2016, 2017; C. L. Zhang et al., 2016; A. V. Zuza et al., 2018).

5.5. Implications for Proterozoic-Phanerozoic Paleogeographic Reconstructions of Eurasia

Herein, we have provided new geologic observations for evaluating the tectonic history of the Qilian Shan, Longshou Shan, and northwest North China regions of Eurasia. These data refine our knowledge of the tectonic evolution of the region, but also provides key constraints for important intercontinent relationships. First, as discussed above, we argue that available geologic evidence suggests that Tarim and North China cratons were contiguous since the Proterozoic, and the lack of appropriate Phanerozoic suture-arc structures separating these continents confirms this assertion. Accordingly, this continental strip separated the Paleo-Asian and Tethyan oceanic realms in the Neoproterozoic and Paleozoic, following global Neoproterozoic rifting. This rifting tectonically calved microcontents from Tarim-North China into the Paleo-Asian Ocean domain (e.g., Levashova et al., 2010, 2011) (Figure 14). The late Paleozoic counter-clockwise wrapping of this continent around continental arc fragments within the Paleo-Asian Ocean ultimately led to its closure as part of the last stages of the Central Asian Orogenic System (e.g., A. V. Zuza & Yin, 2017).

Second, our traverse and published literature are at odds with North China and Tarim being located along the northern margin of Gondwana. The potential Cambrian connection between North China and India was established on the basis of trilobite fossils and detrital zircon comparisons (McKenzie et al., 2011), which has been perpetuated in the literature (e.g., Y. Han et al., 2016; Myrow et al., 2015). However, these reconstructions do not allow for an ocean to exist south of North China and provide no space for the Qilian arc-orogen to exist along this margin (e.g., Figure 2). Our observations of the early Paleozoic Qilian orogen transitioning northward to the North China craton requires abandonment or reevaluation of North China-Gondwana reconstructions. Furthermore, recent reconstructions based on new paleomagnetic poles have placed the Tarim craton along the western margin of Laurentia in the Neoproterozoic (Wen et al., 2017, 2018). Based on our interpretations of a contiguous North Tarim-North China (A. V. Zuza & Yin, 2017; this study), one can extrapolate that North China may have also been adjacent to Laurentia in the Rodinian supercontinent (e.g., A. V. Zuza & Yin, 2013, 2017), which would provide a relatively long continental strip to be the conjugate of western Laurentia's classic linear rift margin (see discussion of Eyster et al., 2020). Our new detrital zircon analyses from Mesoproterozoic strata yielded zircon spectra similar to Mesoproterozoic rocks in western North American, including 1.5–1.6 Ga ages that are observed in Belt-Purcell Supergroup strata are otherwise rare in North American zircons (e.g., Link et al., 2007; Ross et al., 1992; Ross & Villeneuve, 2003). Further testing of this hypothesis is not within the scope of this study. The ca. 1.5 Ga basement gneiss or sills probably originated from North Tarim or western North China (e.g., Demoux et al., 2009; C. Z. Wu et al., 2014; C. Wu et al., 2017). Alternatively, we acknowledge that 1.5–1.6 Ga rocks and detrital zircon ages are reported in the Australia and South China cratons (e.g., Giles et al., 2004; Zhao & Cawood, 2012).

Last, the complex polyphase arc-collisional history in this region probably focused Cenozoic shortening and strike-slip faulting related to the India-Asia collision. This region occupies the northernmost margin of the Tibetan Plateau, and available thermochronology constraints suggest that exhumation and deformation here started shortly after initial India-Asia collision (i.e., Eocene; e.g., An et al., 2020; Dupont-Nivet et al., 2004; B. Li et al., 2020b; Qi et al., 2016). This relationship strongly suggests that orogeny since the Proterozoic weakened the crust and mantle lithosphere here to be reactivated in the Himalayan-Tibetan orogen (e.g., Bian et al., 2020; L. Chen et al., 2017), thus establishing the northern limit of the Tibetan Plateau.

5.6. Implications for Paleoproterozoic Supercontinent Reconstruction

Supercontinent configurations and paleogeography are partly based on spatial and temporal correlations of important geologic features, such as crystalline basement, arc magmatic events, and tectono-metamorphism. Two stages of Paleoproterozoic orogeny-related leucogranites were developed in the Longshou Shan region, i.e., ca. 1.88 Ga and ca. 2.05 Ga. A ca. 1.9–1.88 Ga mélange was reported along the northern margin of the North China craton, which was considered that the North China craton was beginning to the context of the Columbia supercontinent from ca. 1.9 Ga (e.g., Kusky et al., 2016; Rogers & Santosh, 2002; C. Wu et al., 2018; G. C. Zhao et al., 2002). The northern North China orogenic event between the North China craton and possible Siberia craton indicates the existence of ca. 2.0 Ga arc, which is supported by scattered 2.0–2.1 Ga magmatic ages in the northern North China craton (e.g., Fan et al., 2010; J. Gong et al., 2016; Kröner et al., 2005; C. Wu et al., 2018; R. F. Zhao et al., 2011, 2008). Our observed ca. 1.88 Ga leucogranite could be interpreted as part of the northern North China orogeny.

Orogeny at 2.0–2.05 Ga is relative rare on Earth and therefore may be a useful for reconstructing continental connections in the Paleoproterozoic. The Limpopo orogenic belt in southern Africa consists mostly of supracrustal assemblages intruded by ca. 3.2 Ga and 2.7–2.6 Ga felsic plutons modified by ductile folding, granulite-amphibolite facies metamorphism, and anatexis at 2.7–2.6 Ga and ca. 2.0 Ga (e.g., Brandt et al., 2018; Kramers & Mouri, 2011; Kröner et al., 2018; Yin et al., 2020), which were folded by north-south compression at ca. 1.97–1.88 Ga (Yin et al., 2020). In addition, ca. 2.05 Ga leucogranite was reported in the Limpopo belt (Zeh et al., 2010). Although the Archean basement is not reported in the Longshou Shan area, the Lu-Hf isotopes of amphibolite-grade folded Longshou Shan Group showed reworking of ca. 2.45–2.65 Ga basement of the North China craton (e.g., J. Gong et al., 2016). Undeformed ca. 1.88 Ga mafic dike intrusions are developed within the folded Paleoproterozoic strata in the South Africa and North China cratons (e.g., Hanson et al., 2004; C. Wu et al., 2018; Yin et al., 2020), which is also consistent with field observations

in Longshou Shan (Figure 7c). Although the age of the mafic dike in Longshou Shan is not constrained, the undeformed ca. 1.88 Ga leucogranite dike is exposed in the same outcrop (Figure 7d). We propose a possible connection between the Limpopo belt in South Africa and Longshou Shan along southwestern margin of the North China craton at ca. 2.05 Ga. In this regard, future detailed tectonic geology studies of the both South Africa and North China cratons should provide further tests of our proposed hypothesis.

6. Conclusions

In this study, we present detailed field, geochronological, and geochemical observations from several key locations in the Qilian Shan, Hexi Corridor, and Longshou Shan areas to decipher complex relationships between the Tarim, North China, and Kunlun-Qaidam continents. This region has been deformed during at least five phases of orogeny since the Proterozoic, including (1) regional granulite-facies metamorphism in the Paleoproterozoic, (2) an enigmatic Neoproterozoic arc-collision, (3) the early Paleozoic Qilian arc development and its amalgamation with the Kunlun-Qaidam continent and the North China, (4) Permian-Triassic magmatism and deformation related to the closure of the Paleo-Asian Ocean to the north, and (5) the most recent Cenozoic contractional deformation related to the India-Asia convergence. Furthermore, our updated geochronology and structural synthesis allows for us to consider a possible connection between the North China and southern Africa at ca. 2.05 Ga.

Data Availability Statement

All data supporting the interpretations and conclusions of this study can be found in the manuscript text, figures, and the supporting information file. Presented geochemistry data used in this study are available in the Interdisciplinary Earth Data Alliance (IEDA) (at https://doi.org/10.26022/IEDA/111780), and the U-Pb zircon geochronology data are available in the Interdisciplinary Earth Data Alliance (IEDA) (at https://doi.org/10.26022/IEDA/111781). There are no restrictions to the data usage.

Acknowledgments
This research was supported by grants from the Basic Science Center for Tibetan Plateau Earth System (CTPES, Grant 41988101-01), the Second Tibetan Plateau Scientific Expedition and Research Program (Grant no. 2019QZKK0708), National Natural Science Foundation of China (Grants nos. 41702232, 41941016, and 41661134049), the National Key Research and Development Project of China (Grant no. 2016YFC0600303), the Chinese Academy of Sciences, Strategic Priority Research Program (Grant no. XDA20070301), the China Geological Survey (DD20160083) and the NSF Tectonics program of the National Science Foundation (EAR 1914501). The authors thank Chief Editor Jonathan Aitchison, Associate Editor Zhen YAN, and three anonymous reviewers for their constructive comments that have led to significant improvements of the original draft of this manuscript; W.-C. Ding and W. Huang for field assistance.

References

An, K., Lin, X., Wu, L., Yang, R., Chen, H., Cheng, X., et al. (2020). An immediate response to the Indian-Eurasian collision along the northeastern Tibetan Plateau: Evidence from apatite fission track analysis in the Kuantan Shan-Hei Shan. *Tectonophysics*, *774*, 228–278.

Arculus, R. J. (2003). Use and abuse of the terms calcalkaline and calcalkalic. *Journal of Petrology*, *44*(5), 929–935. https://doi.org/10.1093/petrology/44.5.929

Badarch, G., Cunningham, W. D., & Windley, B. F. (2002). A new terrane subdivision for Mongolia: Implications for the Phanerozoic crustal growth of Central Asia. *Journal of Asian Earth Sciences*, *21*, 87–110.

Bai, J., & Dai, F. Y. (1996). The early Precambrian crustal evolution of China. *Journal of Southeast Asian Earth Sciences*, *13*(3–5), 205–214 (in Chinese with English Abstract).

Bian, S., Gong, J., Chen, L., Zuza, A. V., Chen, H., Lin, X., et al. (2020). Diachronous uplift in intra-continental orogeny: 2D thermo-mechanical modeling of the India-Asia collision. *Tectonophysics*, *775*, 228310. https://doi.org/10.1016/j.tecto.2019.228310

Biske, Y. S., & Seltmann, R. (2010). Paleozoic Tian-Shan as a transitional region between the Rheic and Urals-Turkestan oceans. *Gondwana Research*, *17*(2–3), 602–613. https://doi.org/10.1016/j.gr.2009.11.014

Boynton, W. V. (1984). Cosmochemistry of the rare earth elements: Meteorite studies, rare earth element. *Geochemistry*, 63–114.

Brandt, S., Klemd, R., Li, Q., Kröner, A., Brandl, G., Fischer, A., et al. (2018). Pressure-temperature evolution during two granulite-facies metamorphic events (2.62 and 2.02 Ga) in rocks from the Central zone of the Limpopo belt, *South Africa: Precambrian Research*, *310*, 471–506.

Carroll, A. R., Graham, S. A., Chang, E. Z., & McKnight, C. (2001). Sinian through Permian tectonostratigraphic evolution of the northwestern Tarim basin, China. In M. S. Hendrix, & G. A. Davis (Eds.), *Paleozoic and Mesozoic tectonic evolution of Central and Eastern Asia: From continental assembly to intracontinental deformation* (pp. 47–69). Geological Society of America Memoir, 194. https://doi.org/10.1130/0-8137-1194-0.47

Chang, S. Q. (1980). Subdivision and correlation of late Precambrian of southern Liaodong Peninsula. *Tianjin Institute of Geology and Mineral Resources Research on Precambrian Geology: Sinian Suberathem in China: Tianjin, China*. (pp. 266–287). Tianjin: Tianjin Science and Technology Press.

Chen, L., Capitanio, F. A., Liu, L. j., & Gerya, T. V. (2017). Crustal rheology controls on the Tibetan plateau formation during India-Asia convergence. *Nature Communications*, *8*, 15992. https://doi.org/10.1038/ncomms15992

Chen, L., Huang, B., Yi, Z., Zhao, J., & Yan, Y. (2013). Paleomagnetism of ca. 1.35 Ga sills in northern North China Craton and implications for paleogeographic reconstruction of the Mesoproterozoic supercontinent. *Precambrian Research*, *228*, 36–47. https://doi.org/10.1016/j.precamres.2013.01.011

Chen, X., Yin, A., Gehrels, G. E., Cowgill, E. S., Grove, M., Harrison, T. M., & Wang, X.-F. (2003). Two phases of Mesozoic north-south extension in the eastern Altyn Tagh range, northern Tibetan Plateau. *Tectonics*, *22*(5), P8–P22. https://doi.org/10.1029/2001tc001336

Chen, X. H., Gehrels, G., Yin, A., Li, L., & Jiang, R. B. (2012). Paleozoic and Mesozoic basement magmatisms of Eastern Qaidam Basin, Northern Qinghai-Tibet plateau: LA-ICP-MS zircon U-Pb geochronology and its geological significance. *Acta Geologica Sinica*, *86*(2), 350–369.

Chen, X. H., Gehrels, G. E., Yin, A., Zhou, Q., & Huang, P. H. (2014). Geochemical and Nd-Sr-Pb-O isotopic constraints on Permo–Triassic magmatism in eastern Qaidam Basin, Northern Qinghai–Tibetan Plateau: Implications for the evolution of the Paleo-Tethys. *Journal of Asian Earth Sciences*, *114*, 674–692. https://doi.org/10.1016/j.jseaes.2014.11.013

Chen, X. H., Shao, Z., Xiong, X., Gao, R., Liu, X., Wang, C., et al. (2019). Fault system, deep structure and tectonic evolution of the Qilian Orogenic Belt, Northwest China. *Geology in China*, *46*(5), 995–1020. https://doi.org/10.12029/gc20190504 (in Chinese with English abstract).

Chen, Y., Xu, B., Zhan, S., & Li, Y. (2004). First mid-Neoproterozoic paleomagnetic results from the Tarim Basin (NW China) and their geodynamic implications. *Precambrian Research*, *133*, 271–281. https://doi.org/10.1016/j.precamres.2004.05.002

Clark, M. K., Farley, K. A., Zheng, D., Wang, Z., & Duvall, A. R. (2010). Early Cenozoic faulting of the northern Tibetan Plateau margin from apatite (U–Th)/He ages. *Earth and Planetary Science Letters*, *296*(1–2), 78–88. http://doi.org/10.1016/j.epsl.2010.04.051

Cowgill, E., Yin, A., Harrison, T. M., & Wang, X. F. (2003). Reconstruction of the Altyn Tagh fault based on U–Pb geochronology: Role of back thrusts, mantle sutures, and heterogeneous crustal strength in forming the Tibetan Plateau. *Journal of Geophysical Research*, *108*(B7), 2346. https://doi.org/10.1029/2002JB002080

Dan, W., Li, X. H., Guo, J. H., Liu, Y., & Wang, X. C. (2012). Integrated in situ zircon U–Pb age and Hf–O isotopes for the Helanshan khondalites in North China Craton: Juvenile crustal materials deposited in active or passive continental margin? *Precambrian Research*, *222*(223), 143–158.

Dan, W., Li, X. H., Wang, Q., Wang, X. C., & Liu, Y. (2014). Neoproterozoic S-type granites in the Alxa Block, westernmost North China and tectonic implications: In situ zircon U-Pb–Hf-O isotopic and geochemical constraints. *American Journal of Science*, *314*, 110–153. https://doi.org/10.2475/01.2014.04

Demoux, A., Kröner, A., Badarch, G., Jian, P., Tomurhuu, D., & Wingate, M. T. (2009). Zircon ages from the Baydrag block and the Bayankhongor ophiolite zone: Time constraints on late Neoproterozoic to Cambrian subduction- and accretion-related magmatism in central Mongolia. *The Journal of Geology*, *117*, 377–397.

Dong, C. Y., Liu, D. Y., Li, J. J., Wan, Y. S., Zhou, H. Y., Li, C. D., et al. (2007). Paleoproterozoic Khondalite belt in the western North China Craton: New evidence from SHRIMP dating and Hf isotope composition of zircons from metamorphic rocks in the Bayan UI–Helan Mountains area. *Chinese Science Bulletin*, *52*, 2984–2994.

Dong, Y., He, D., Sun, S., Liu, X., Zhou, X., Zhang, F., & Li, J. (2018). Subduction and accretionary tectonics of the East Kunlun orogen, western segment of the Central China orogenic system. *Earth-Science Reviews*, *186*, 231–261. https://doi.org/10.1016/j.earscirev.2017.12.006

Dong, Y., Liu, X., Neubauer, F., Zhang, G., Tao, N., Zhang, Y., et al. (2013). Timing of Paleozoic amalgamation between the North China and South China blocks: Evidence from detrital zircon U–Pb ages. *Tectonophysics*, *586*, 173–191. https://doi.org/10.1016/j.tecto.2012.11.018

Dulski, P. (1994). Interferences of oxide, hydroxide and chloride analyte species in the determination of rare earth elements in geological samples by inductively coupled plasma-mass spectrometry. *Fresenius' Journal of Analytical Chemistry*, *350*, 194–203.

Dupont-Nivet, G., Horton, B. K., Butler, R. F., Wang, J., Zhou, J., & Waanders, G. L. (2004). Paleogene clockwise tectonic rotation of the Xining–Lanzhou region, northeastern Tibetan Plateau. *Journal of Geophysical Research*, *109*, B04401. https://doi.org/10.1029/2003JB002620

Duvall, A. R., Clark, M. K., Kirby, E., Farley, K. A., Craddock, W. H., Li, C., & Yuan, D.-Y. (2013). Low-temperature thermochronometry along the Kunlun and Haiyuan Faults, NE Tibetan Plateau: Evidence for kinematic change during late-stage orogenesis. *Tectonics*, *32*(5), 1190–1211. http://doi.org/10.1002/tect.20072

Duvall, A. R., Clark, M. K., van der Pluijm, B. A., & Li, C. (2011). Direct dating of Eocene reverse faulting in north-eastern Tibet using Ar-dating of fault clays and low-temperature thermochronometry. *Earth and Planetary Science Letters*, *304*(3–4), 520–526. https://doi.org/10.1016/j.epsl.2011.02.028

Eby, G. N. (1990). The A-type granitoids: A review of their occurrence and chemical characteristics and speculations on their petrogenesis. *Lithos*, *26*, 115–134.

Eby, G. N. (1992). Chemical subdivision of the A-type granitoids: Petrogenetic and tectonic implications. *Geology*, *20*, 641–644.

Eizenhöfer, P. R., Zhao, G., Zhang, J., & Sun, M. (2014). Final closure of the Paleo-Asian Ocean along the Solonker suture zone: Constraints from geochronological and geochemical data of Permian volcanic and sedimentary rocks. *Tectonics*, *33*(4), 441–463. https://doi.org/10.1002/2013tc003357

Eyster, A., Weiss, B. P., Karlstrom, K., & Macdonald, F. A. (2020). Paleomagnetism of the Chuar Group and evaluation of the late Tonian Laurentian apparent polar wander path with implications for the makeup and breakup of Rodinia. *Geological Society of America Bulletin*, *132*(3–4), 710–738

Fan, H. R., Yang, K. F., Hu, F. F., Wang, K. Y., & Zhai, M. G. (2010). Zircon geochronology of basement rocks from the BayanObo area, Inner Mongolia, and tectonic implications. *Acta Petrologica Sinica*, *26*, 1342–1350 (in Chinese with English abstract).

Faure, M., Trap, P., Lin, W., Monie, P., & Bruguier, O. (2007). Polyorogenic evolution of the paleoproterozoic Trans-north China belt—New insights from the Luliangshan-Hengshan-Wutaishan and Fuping massifs. *Episodes*, *30*(2), 96–107.

Fu, C. L., Yan, Z., Wang, Z. Q., Buckman, S., Aitchison, J. C., Niu, M. L., et al. (2018). Lajishankou ophiolite complex: Implications for Paleozoic multiple accretionary and collisional events in the South Qilian belt. *Tectonics*, *37*, 1321–1346. https://doi.org/10.1029/2017TC004740

Fu, D., Kusky, T., Wilde, S. A., Polat, A., Huang, B., & Zhou, Z. P. (2019). Early Paleozoic collision-related magmatism in the eastern North Qilian orogen, northern Tibet: A linkage between accretionary and collisional orogenesis. *Geological Society of America Bulletin*, *131*(5–6), 1031–1056.

Gaudemer, Y., Tapponnier, P., Meyer, B., Peltzer, G., Shunmin, G., Zhitai, C., et al. (1995). Partitioning of crustal slip between linked, active faults in the eastern Qilian Shan, and evidence for a major seismic gap, the "Tianzhu gap," on the western Haiyuan fault, Gansu (China). *Geophysical Journal International*, *120*(3), 599–645. https://doi.org/10.1111/j.1365-246X.1995.tb01842.x

Gehrels, G., Kapp, P., DeCelles, P., Pullen, A., Blakey, R., Weislogel, A., et al. (2011). Detrital zircon geochronology of pre-Tertiary strata in the Tibetan-Himalayan orogen. *Tectonics*, *30*(5), TC5016. https://doi.org/10.1029/2011tc002868

Gehrels, G. E., DeCelles, P. G., Ojha, T. P., & Upreti, B. N. (2006). Geologic and U-Th-Pb geochronologic evidence for early Paleozoic tectonism in the Kathmandu thrust sheet, central Nepal Himalaya. *Geological Society of America Bulletin*, *118*(1–2), 185–198. https://doi.org/10.1130/b25753.1

Gehrels, G. E., Yin, A., & Wang, X.-F. (2003a). Detrital-zircon geochronology of the northeastern Tibetan plateau. *Geological Society of America Bulletin*, *115*(7), 881–896. https://doi.org/10.1130/0016-7606(2003)115<0881:dgotnt>2.0.co;2

Gehrels, G. E., Yin, A., & Wang, X.-F. (2003b). Magmatic history of the northeastern Tibetan Plateau. *Journal of Geophysical Research*, *108*(B9). https://doi.org/10.1029/2002jb001876

Ge, R. F., Wilde, S. A., Kemp, A. I. S., Jeon, H., Martin, L. A. J., Zhu, W. B., & Wu, H. L. (2020). Generation of Eoarchean continental crust from altered mafic rocks derived from a chondritic mantle: The ~3.72 Ga Aktash gneisses, Tarim Craton (NW China). *Earth and Planetary Science Letters*, *538*, 116225. https://doi.org/10.1016/j.epsl.2020.116225

Ge, R. F., Zhu, W. B., Wilde, S. A., He, J. W., Cui, X., Wang, X., & Zheng, B. (2014). Neoproterozoic to Paleozoic long-lived accretionary orogeny in the northern Tarim Craton. *Tectonics*, *33*, 302–329.

Ge, R. F., Zhu, W. B., Wilde, S. A., & Wu, H. L. (2018). Remnants of Eoarchean continental crust derived from a subducted proto-arc. *Science Advances*, *4*, eaao3159. https://doi.org/10.1126/sciadv.aao3159

Ge, R., Zhu, W., & Wilde, S. A. (2016). Mid-Neoproterozoic (ca. 830–800 Ma) metamorphic P-T paths link Tarim to the circum-Rodinia subduction-accretion system. *Tectonics*, *35*(6), 1465–1488.

Ge, R., Zhu, W., Wilde, S. A., He, J., & Cui, X. (2015). Synchronous crustal growth and reworking recorded in late Paleoproterozoic granitoids in the northern Tarim craton: In situ zircon U-Pb-Hf-O isotopic and geochemical constraints and tectonic implications: *Geological Society of America Bulletin*, *127*, 781–803, https://doi.org/10.1130/B31050.1

Giles, D., Betts, P. G., & Lister, G. S. (2004). 1.8–1.5-Ga links between the north and south Australian cratons and the early–middle Proterozoic configuration of Australia. *Tectonophysics*, *380*(1–2), 27–41.

Gong, S., Chen, N., Wang, Q., Kusky, T. M., Wang, L., Zhang, L., et al. (2012). Early Paleoproterozoic magmatism in the Quanji Massif, northeastern margin of the Qinghai–Tibet Plateau and its tectonic significance: LA-ICPMS U-Pb zircon geochronology and geochemistry: *Gondwana Research*, *21*, 152–166. https://doi.org/10.1016/j.gr.2011.07.011

Gong, J., Zhang, J., Wang, Z., Yu, S., Li, H., & Li, Y. (2016). Origin of the Alxa block, western China: New evidence from zircon U-Pb geochronology and Hf isotopes of the Longshoushan complex. *Gondwana Research*, *36*, 359–375.

Gong, J., Zhang, J., Yu, S., Li, H., & Hou, K. (2012). Ca. 2.5 Ga TTG rocks in the western Alxa Block and their implications. *Chinese Science Bulletin*, *57*, 4064–4076.

Gong, J. H., Zhang, J. X., & Yu, S. Y. (2013). Redefinition of the Longshoushan group outcropped in the eastern segment of Longshoushan on the southern margin of Alxa block: Evidence from detrital zircon U-Pb dating results. *Acta Petrologica et Minerlogica*, *32*(1), 1–22 (in Chinese with English Abstract).

Guo, K. Y., Zhang, C. L., Shen, J. L., Ye, H., Wang, A. G., & Li, C. (2004). Chemistry of Statherian volcanic rocks in the western Kunlun Mountains. *Geological Bulletin of China*, *23*, 130–135 (in Chinese).

Guo, Z. J., Yin, A., Robinson, A., & Jia, C. Z. (2005). Geochronology and geochemistry of deep-drill-core samples from the basement of the central Tarim basin. *Journal of Asian Earth Sciences*, *25*(1), 45–56.

Hacker, B. R., Ratschbacher, L., & Liou, J. G. (2004). Subduction, collision, and exhumation in the Qinling-Dabie orogeny. In J. Malpas et al. (Eds.), Aspects of the tectonic evolution of China (Vol. 226, pp. 157–175). Geological Society of London Special Publication. https://doi.org/10.1144/GSL.SP.2004.226.01.09

Hacker, B. R., Wallis, S. R., Ratschbacher, L., Grove, M., & Gehrels, G. (2006). High-temperature geochronology constraints on the tectonic history and architecture of the ultrahigh-pressure Dabie-Sulu orogen. *Tectonics*, *25*, TC5006. https://doi.org/10.1029/2005TC001937

Han, S. X., Wu, C., Zhou, Z. G., & Wang, G. S. (2020). Geology, geochemistry, and geochronology of the paleoproterozoic Donggouzi mafic-ultramafic complex: Implications for the evolution of the North China craton. *Lithos*, 366–367. https://doi.org/10.1016/j.lithos.2020.105567

Han, Y., Zhao, G., Cawood, P. A., Sun, M., Eizenhöfer, P. R., Hou, W., et al. (2016). Tarim and North China cratons linked to northern Gondwana through switching accretionary tectonics and collisional orogenesis. *Geology*, *44*(2), 95–98. https://doi.org/10.1130/g37399.1

Hanson, R. E., Gose, W. A., Crowley, J. L., Ramezani, J., Bowring, S. A., Bullen, D. S., et al. (2004). Paleoproterozoic intraplate magmatism and basin development on the Kaapvaal craton: Age, paleomagnetism and geochemistry of ~1.93 to ~1.87 Ga post-Waterberg dolerites: *South African Journal of Geology*, *107*, 233–254.

Harrison, T. M., & Wielicki, M. M. (2016). From the Hadean to the Himalaya: 4.4 Ga of felsic terrestrial magmatism. *American Mineralogist*, *101*(6), 1348–1359.

He, Z. Y., Zhang, Z. M., Zong, K. Q., Wang, W., & Santosh, M. (2012). Neoproterozoic granulites from the northeastern margin of the Tarim Craton: Petrology, zircon U-Pb ages and implications for the Rodinia assembly. *Precambrian Research*, *212–213*, 21–33. https://doi.org/10.1016/j.precamres.2012.04.014

Heubeck, C. (2001). Assembly of central Asia during the middle and late Paleozoic. In M. S. Hendrix, & G. A. Davis (Eds.), *Paleozoic and Mesozoic tectonic evolution of central Asia: From continental assembly to intracontinental deformation*. (pp. 1–22). Boulder, CO: Geological Society of America Memoir 194.

Irvine, T. N., & Baragar, W. R. A. (1971). A guide to the chemical classification of the common volcanic rocks. *Canadian Journal of Earth Sciences*, *8*(5), 523–548. https://doi.org/10.1139/e71-055

Jackson, S. E., Pearson, N. J., Griffin, W. L., & Belousova, E. A. (2004). The application of laser ablation-inductively coupled plasma-mass spectrometry to in situ U–Pb zircon geochronology. *Chemical Geology*, *211*(1–2), 47–69. https://doi.org/10.1016/j.chemgeo.2004.06.017

Jia, C. Z. (1997). *Tectonic characteristics and petroleum, Tarim basin* (p. 439). Beijing: Petroleum Industry Press (in Chinese).

Jian, P., Kröner, A., Shi, Y., Zhang, W., Liu, Y., Windley, B. F., et al. (2016). Age and provenance constraints on seismically-determined crustal layers beneath the Paleozoic southern Central Asian Orogen, Inner Mongolia, China. *Journal of Asian Earth Sciences*, *123*, 119–141. https://doi.org/10.1016/j.jseaes.2016.04.001

Jiang, C. F., Yang, J. S., Feng, B. G., Zhu, Z. Z., Zhao, M., Chai, Y. C., et al. (1992). *Opening closing tectonics of Kunlun Mountains* (p. 224). Beijing: Geological Publishing House. (in Chinese with English abstract).

Kröner, A., Alexeiev, D. V., Rojas-Agramonte, Y., Hegner, E., Wong, J., Xia, X., et al. (2013). Mesoproterozoic (Grenville-age) terranes in the Kyrgyz North Tianshan: Zircon ages and Nd-Hf isotopic constraints on the origin and evolution of basement blocks in the southern Central Asian Orogen. *Gondwana Research*, *23*, 272–295. https://doi.org/10.1016/j.gr.2012.05.004

Kröner, A., Brandl, G., Brandt, S., Klemd, R., & Xie, H. (2018). Geochronological evidence for Archaean and Palaeoproterozoic polymetamorphism in the central zone of the Limpopo belt, South Africa. *Precambrian Research*, *310*, 320–347.

Kramers, J. D., & Mouri, H. (2011). The geochronology of the Limpopo Complex: A controversy solved. *Geological Society of America Memoirs*, *207*(11), 85.

Kröner, A., Wilde, S. A., Li, J. H., & Wang, K. Y. (2005). Age and evolution of a late Archean to Paleoproterozoic upper to lower crustal section in the Wutaishan/Hengshan/Fuping terrain of northern China. *Journal of Asian Earth Sciences*, *24*(5), 577–595. https://doi.org/10.1016/j.jseaes.2004.01.001

Kuno, H. (1968). Origin of andesite and its bearing on the Island arc structure. *Bulletin of Volcanology*, *32*(1), 141–176.

Kusky, T. M., & Li, J. (2003). Paleoproterozoic tectonic evolution of the North China craton. *Journal of Asian Earth Sciences*, *22*(4), 383–397. https://doi.org/10.1016/s1367-9120(03)00071-3

Kusky, T. M., Li, J. H., & Santosh, M. (2007). The Paleoproterozoic North Hebei orogen: North China craton's collisional suture with the Columbia supercontinent. *Gondwana Research*, *12*(1–2), 4–28. https://doi.org/10.1016/j.gr.2006.11.012

Kusky, T. M., Polat, A., Windley, B. F., Burke, K. C., Dewey, J. F., Kidd, W. S. F., et al. (2016). Insights into the tectonic evolution of the North China Craton through comparative tectonic analysis: A record of outward growth of Precambrian continents. *Earth-Science Reviews*, *162*, 387–432. https://doi.org/10.1016/j.earscirev.2016.09.002

Le Maitre, R. W. B., Dudek, P., Keller, A., Lameyre, J., Le Bas, J., Sabine, M. J., et al. (1989). *A classification of igneous rocks and Glossary of terms: Recommendations of the International Union of Geological Sciences, Subcommission on the Systematics of igneous rocks (No. 552.3 CLA)* (p. 193). Oxford: International Union of Geological Sciences, Blackwell.

Lehmann, J., Arndt, N., Windley, B., Zhou, M., Wang, C. Y., & Harris, C. (2007). Field relationships and geochemical constraints on the emplacement of the Jinchuan intrusion and its Ni-Cu-PGE sulfide deposit, Gansu, China. *Economic Geology*, *102*, 75–94.

Levashova, N. M., Kalugin, V. M., Gibsher, A. S., Yff, J., Ryabinin, A. B., Meert, J. G., & Malone, S. J. (2010). The origin of the Baydaric microcontinent, Mongolia: Constraints from paleomagnetism and geochronology: *Tectonophysics*, *485*, 306–320.

Levashova, N. M., Meert, J. G., Gibsher, A. S., Grice, W. C., & Bazhenov, M. L. (2011). The origin of microcontinents in the Central Asian orogenic belt: Constraints from paleomagnetism and geochronology. *Precambrian Research*, *185*, 37–54.

Li, B., Chen, X., Zuza, A. V., Hu, D., Ding,W., Huang, P., & Xu, S. (2019). Cenozoic cooling history of the North Qilian Shan, northern Tibetan Plateau, and the initiation of the Haiyuan fault: Constraints from apatite-and zircon-fission track thermochronology. *Tectonophysics*, *751*,109–124.

Li, B., Zuza, A. V., Chen, X., Hu, D., Shao, Z., Qi, B., et al. (2020b). Cenozoic multi-phase deformation in the Qilian Shan and out-of-sequence development of the northern Tibetan Plateau. *Tectonophysics*, *228423*, 782–783.

Li, B., Zuza, A. V., Chen, X. H., Wang, Z. Z., Shao, Z. G., Levy, D. A., et al. (2020a). Pre-cenozoic evolution of the northern Qilian Orogen from zircon geochronology: Framework for early growth of the northern Tibetan Plateau. *Palaeogeography, Palaeoclimatology, Palaeoecology*, *11091*. https://doi.org/10.1016/j.palaeo.2020.110091

Li, S., Zhao, S., Liu, X., Cao, H., Yu, S., Li, X., & Suo, Y. (2018). Closure of the Proto-Tethys Ocean and Early Paleozoic amalgamation of microcontinental blocks in East Asia. *Earth-Science Reviews*, *186*, 37–75.

Li, X. H., Su, L., Chung, S. L., Li, Z. X., Liu, Y., Song, B., & Liu, D. Y. (2005). Formation of the Jinchuan ultramafic intrusion and the world's third largest Ni-Cu sulfide deposit: Associated with the ~825 Ma south China mantle plume? *Geochemistry, Geophysics, Geosystems*, *6*(11). https://doi.org/10.1029/2005gc001006

Li, X. H., Su, L., Song, B., & Liu, D. Y. (2004). SHRIMP U-Pb zircon age of the Jinchuan ultramafic intrusion and its geological significance. *Chinese Science Bulletin*, *49*(4), 420–422. https://doi.org/10.1360/04wd0041

Li, Y. L., Xiao, W. J., Li, Z. Y., Wang, K., Zheng, J. P., & Brouwer, F. M. (2020). Early Neoproterozoic magmatism in the Central Qilian block, NW China: Geochronological and petrogenetic constraints for Rodinia assembly. *GSA Bulletin*, *132*(11/12), 2415–2431. https://doi.org/10.1130/B35637.1

Li, Z. X., Bogdanova, S. V., Collins, A. S., Davidson, A., De Waele, B., Ernst, R. E., et al. (2008). Assembly, configuration, and break-up history of Rodinia: A synthesis. *Precambrian Research*, *160*, 179–210.

Li, Z. X., Qiu, N., Chang, J., & Yang, X. (2015). Precambrian evolution of the Tarim Block and its tectonic affinity to other major continental blocks in China: New clues from U-Pb geochronology and Lu-Hf isotopes of detrital zircons: *Precambrian Research*, *270*, 1–21. https://doi.org/10.1016/j.precamres.2015.09.011

Lin, C., Yang, H., Liu, J., Rui, Z., Cai, Z., & Zhu, Y. (2012). Distribution and erosion of the Paleozoic tectonic unconformities in the Tarim Basin, Northwest China: Significance for the evolution of paleo-uplifts and tectonic geography during deformation. *Journal of Asian Earth Sciences*, *46*, 1–19.

Link, P. K., Fanning, C. M., Lund, K. I., & Aleinikoff, J. N. (2007). Detrital zircons, correlation and provenance of Mesoproterozoic Belt Supergroup and correlative strata of east-central Idaho and southwest Montana. In P. K. Link, & R. S. Lewis (Eds.), Proterozoic geology of western North America and Siberia (Vol. 86, pp. 101–128). SEPM (Society for Sedimentary Geology) Special Publication.

Liu, C. F., Wu, C., Song, Z., Liu, W., & Zhang, H. (2019). Petrogenesis and tectonic significance of Early Paleozoic magmatism in the northern margin of the Qilian block, northeastern Tibetan Plateau. *Lithosphere*, *11*(3), 365–385. https://doi.org/10.1130/l1047.1

Liu, C. F., Wu, C., Zhou, Z. G., Zhu, Y., Jiang, T., Song, Z. J., et al. (2018). U–Pb detrital zircon geochronology from the basement of the Central Qilian terrane: Implications for tectonic evolution of northeastern Tibetan Plateau. *International Journal of Earth Sciences*, *107*, 673–686. https://doi.org/10.1007/s00531-017-1522-5

Liu, J. N., Yin, C. Q., Zhang, J., Qian, J. H., Li, S., Xu, K. Y., et al. (2020). Tectonic evolution of the Alxa Block and its affinity: Evidence from the U-Pb geochronology and Lu-Hf isotopes of detrital zircons from the Longshoushan Belt. *Precambrian Research*, *344*, 105733. https://doi.org/10.1016/j.precamres.2020.105733

Liu, S., Hu, R., Gao, S., Feng, C., Coulson, I. M., Feng, G., et al. (2012). U-Pb zircon age, geochemical and Sr-Nd isotopic data as constraints on the petrogenesis and emplacement time of the Precambrian mafic dyke swarms in the North China Craton (NCC). *Lithos*, *140*, 38–52. https://doi.org/10.1016/j.lithos.2012.01.002

Lu, S., Li, H., Zhang, C., & Niu, G. (2008). Geological and geochronological evidence for the Precambrian evolution of the Tarim Craton and surrounding continental fragments. *Precambrian Research*, *160*, 94–107. https://doi.org/10.1016/j.precamres.2007.04.025

Lu, S. N. (1992). *Geological evolution of Proterozoic in Kuruktage* (Vols. 26–27, pp. 279–292). Xinjiang: Bulletin of the Tianjin Institute of Geology and Mineral Resources, CAGS (in Chinese).

Lu, S. N. (2002). *Preliminary study of Precambrian geology in the North Tibet-Qinghai Plateau* (p. 125). Beijing: Geological Publishing House (in Chinese).

Lu, S. N., Yu, H. F., & Li, H. K. (2006). *Research on Precambrian major problems in China* (p. 206). Beijing: Geological Publishing Press (in Chinese).

Lu, S. N., & Yuan, G. B. (2003). Geochronology of early Precambrian magmatic Activities in Aketashiage, East Altyn Tagh. *Acta Geologica Sinica*, *77*(1), 61–68 (in Chinese with English Abstract).

McKenzie, N. R., Hughes, N. C., Myrow, P. M., Choi, D. K., & Park, T.-Y. (2011). Trilobites and zircons link north China with the eastern Himalaya during the Cambrian. *Geology*, *39*(6), 591–594. https://doi.org/10.1130/g31838.1

Mei, H., Yu, H., Lu, S., & Li, H. (1998). The Archean tonalite in Dunhuang, Gansu province: Single-zircon U-Pb age and Nd isotope. *Progress in Precambrian Research*, *21*, 41–45 (in Chinese with English abstract).

Menold, C. A., Grove, M., Sievers, N. E., Manning, C. E., Yin, A., Young, E. D., & Ziegler, K. (2016). Argon, oxygen, and boron isotopic evidence documenting $^{40}Ar_E$ accumulation in phengite during water-rich high-pressure subduction metasomatism of continental crust. *Earth and Planetary Science Letters*, *446*, 56–67. https://doi.org/10.1016/j.epsl.2016.04.010

Menold, C. A., Manning, C. E., Yin, A., Tropper, P., Chen, X. H., & Wang, X. F. (2009). Metamorphic evolution, mineral chemistry and thermobarometry of orthogneiss hosting ultrahigh-pressure eclogites in the North Qaidam metamorphic belt, Western China. *Journal of Asian Earth Sciences*, *35*(3–4), 273–284. https://doi.org/10.1016/j.jseaes.2008.12.008

Middlemost, E. A. K. (1994). Naming materials in the magma/igneous rock system. *Earth-Science Reviews*, *37*, 215–224.

Myrow, P. M., Chen, J., Snyder, Z., Leslie, S., Fike, D. A., Fanning, C. M., et al. (2015). Depositional history, tectonics, and provenance of the Cambrian-Ordovician boundary interval in the western margin of the North China block. *The Geological Society of America Bulletin*, *127*(9–10), 1174–1193. https://doi.org/10.1130/b31228.1

Noble, S. R., & Searle, M. P. (1995). Age of crustal melting and leucogranite formation from U-Pb zircon and monazite dating in the western Himalaya, Zanskar, India. *Geology*, *23*(12), 1135–1138. https://doi.org/10.1130/0091-7613(1995)023<1135:aocmal>2.3.co;2

Norrish, K., & Chappel, B. W. (1977). X-ray fluorescence spectrometry. In J. Zussman (Ed.), *Physical Methods in Determinative Mineralogy*, 235–237.

Pan, G. T., Ding, J., Yao, D., & Wang, L. (2004). Geological map of Qinghai-Xiang (Tibet) Plateau and adjacent areas: Chengdu Institute of geology and mineral Resources. *China Geological Survey*. Chengdu: Chengdu Cartographic Publishing House. Scale 1:1,500,000.

Pearce, J. A. (1996). Sources and settings of granitic rocks. *Episodes*, *19*, 120–125.

Pearce, J. A., Harris, N. B. W., & Tindle, A. G. (1984). Trace element discrimination diagrams for the tectonic interpretation of granitic rocks. *Journal of Petrology*, *25*(4), 956–983.

Peccerillo, A., & Taylor, S. R. (1976). Geochemistry of Eocene calc-alkaline volcanic rocks from the Kastamonu area. *Northern Turkey Contributions to Mineralogy and Petrology*, *58*(1), 63–81. https://doi.org/10.1007/BF00384745

Peltzer, G., & Tapponnier, P. (1988). Formation and evolution of strike-slip faults, rifts, and basins during the India-Asia collision: An experimental approach. *Journal of Geophysical Research*, *93*(B12), 15085–15117.

Peng, P., Bleeker, W., Ernst, R. E., Söderlund, U., & McNicoll, V. (2011). U-Pb baddeleyite ages, distribution and geochemistry of 925 Ma mafic dykes and 900 Ma sills in the North China Craton: Evidence for a Neoproterozoic mantle plume. *Lithos*, *127*, 210–221. https://doi.org/10.1016/j.lithos.2011.08.018

Peng, P., Zhai, M., Ernst, R. E., Guo, J., Liu, F., & Hu, B. (2008). A 1.78 Ga large igneous province in the North China craton: The Xiong'er Volcanic Province and the North China dyke swarm. *Lithos*, *101*(3–4), 260–280. https://doi.org/10.1016/j.lithos.2007.07.006

Peng, Y. B., Yu, S. Y., Li, S. Z., Zhang, J. X., Liu, Y. J., Li, Y. S., & Santosh, M. (2019). Early Neoproterozoic magmatic imprints in the Altun-Qilian-Kunlun region of the Qinghai-Tibet plateau: Response to the assembly and breakup of Rodinia supercontinent. *Earth-Science Reviews*, *199*, 102954. https://doi.org/10.1016/j.earscirev.2019.102954

Polat, A., Kusky, T., Li, J., Fryer, B., Kerrich, R., & Patrick, K. (2005). Geochemistry of Neoarchean (ca. 2.55–2.50 Ga) volcanic and ophiolitic rocks in the Wutaishan greenstone belt, central orogenic belt, North China craton: Implications for geodynamic setting and continental growth. *Geological Society of America Bulletin*, *117*(11/12), 1387–1399. https://doi.org/10.1130/b25724.1

Porter, T. M. (2016). Regional tectonics, geology, magma chamber processes and mineralization of the Jinchuan nickel-copper-PGE deposit, Gansu Province, China: A review. *Geoscience Frontiers*, *7*(3), 431–451. https://doi.org/10.1016/j.gsf.2015.10.005

Pullen, A., Ibáñez-Mejia, M., Gehrels, G. E., Giesler, D., & Pecha, M. (2018). Optimization of a laser ablation-single Collector-inductively coupled plasma-mass spectrometer (thermo element 2) for Accurate, Precise, and Efficient zircon U-Th-Pb geochronology. *Geochemistry, Geophysics, Geosystems*, *19*(10), 3689–3705. https://doi.org/10.1029/2018gc007889

Qi, B., Hu, D., Yang, X., Zhang, Y., Tan, C., Zhang, P., & Feng, C. (2016). Apatite fission track evidence for the Cretaceous-Cenozoic cooling history of the Qilian Shan (NW China) and for stepwise northeastward growth of the northeastern Tibetan Plateau since early Eocene. *Journal of Asian Earth Sciences*, *124*, 28–41.

Qinghai BGMR (Bureau of Geology and Mineral Resources). (1991). *Regional geology of Qinghai province* (p. 662). Beijing: Geological Publishing House.

Ratschbacher, L., Hacker, B. R., Calvert, A., Webb, L. E., Grimmer, J. C., McWilliams, M. O., et al. (2003). Tectonics of the Qinling (Central China): Tectonostratigraphy, geochronology, and deformation history. *Tectonophysics*, *366*(1–2), 1–53. https://doi.org/10.1016/s0040-1951(03)00053-2

Rickwood, P. C. (1989). Boundary lines within petrologic diagrams which use oxides of major and minor elements. *Lithos*, *22*, 247–263.

Rogers, J. J. W., & Santosh, M. (2002). Configuration of Columbia, a mesoproterozoic supercontinent. *Gondwana Research*, *5*(1), 5–22.

Rollinson, H. (2014). Plagiogranites from the mantle section of the Oman Ophiolite: Models for early crustal evolution. *Geological Society, London, Special Publications*, *392*(1), 247–261. https://doi.org/10.1144/sp392.13

Ross, G. M., Parrish, R. R., & Winston, D. (1992). Provenance and U-Pb geochronology of the Mesoproterozoic Belt Supergroup (northwestern United States): Implications for age of deposition and pre-Panthalassa plate reconstructions: *Earth and Planetary Science Letters*, *113*, 57–76.

Ross, G. M., & Villeneuve, M. (2003). Provenance of the Mesoproterozoic (1.45 Ga) Belt basin (western North America): Another piece in the pre-Rodinia paleogeographic puzzle. *Geological Society of America Bulletin*, *115*, 1191–1217.

Santosh, M., Sajeev, K., & Li, J. H. (2006). Extreme crustal metamorphism during Columbia supercontinent assembly: Evidence from North China Craton. *Gondwana Research*, *10*(3–4), 256–266. https://doi.org/10.1016/j.gr.2006.06.005

Santosh, M., Wilde, S., & Li, J. (2007). Timing of Paleoproterozoic ultrahigh-temperature metamorphism in the North China craton: Evidence from SHRIMP U–Pb zircon geochronology. *Precambrian Research*, *159*(3–4), 178–196. https://doi.org/10.1016/j.precamres.2007.06.006

Scotese, C. R., & McKerrow, W. S. (1990). Revised World maps and introduction. In W. S. McKerrow, & C. R. Scotese (Eds.), Palaeozoic paleogeography and biogeography (Vol. 12, pp. 1–21). Boulder, CO: Geological Society of America Memoir.

Şengör, A. M. C., & Natal'in, B. A. (1996). Turkic-type orogeny and its role in the making of the continental crust. *Annual Review of Earth and Planetary Sciences*, *24*, 263–337.

Sláma, J., Košler, J., Condon, D. J., Crowley, J. L., Gerdes, A., Hanchar, J. M., et al. (2008). Plešovice zircon—A new natural reference material for U–Pb and Hf isotopic microanalysis. *Chemical Geology*, *249*(1–2), 1–35. https://doi.org/10.1016/j.chemgeo.2007.11.005

Sobel, E. R., & Arnaud, N. (1999). A possible middle Paleozoic suture in the Altyn Tagh, NW China. *Tectonics*, *18*(1), 64–74. https://doi.org/10.1029/1998tc900023

Sone, M., & Metcalfe, I. (2008). Parallel Tethyan sutures in mainland Southeast Asia: New insights for Palaeo-Tethys closure and implications for the Indosinian orogeny. *Comptes Rendus Geoscience*, *340*(2–3), 166–179. https://doi.org/10.1016/j.crte.2007.09.008

Song, D. F., Xiao, W. J., Collins, A. S., Glorie, S., Han, C. M., & Li, Y. C. (2017). New chronological constrains on the tectonic affinity of the Alxa Block, NW China. *Precambrian Research*, *299*(2017), 230–243.
Song, S., Niu, Y., Su, L., & Xia, X. (2013). Tectonics of the North Qilian orogen, NW China. *Gondwana Research*, *23*(4), 1378–1401. https://doi.org/10.1016/j.gr.2012.02.004
Song, S., Niu, Y., Su, L., Zhang, C., & Zhang, L. F. (2014). Continental orogenesis from ocean subduction, continent collision/subduction, to orogen collapse, and orogen recycling: The example of the North Qaidam UHPM belt, NW China. *Earth-Science Reviews*, *129*, 59–84. https://doi.org/10.1016/j.earscirev.2013.11.010
Song, S. G., Niu, Y. L., Zhang, G. B., & Zhang, L. F. (2019). Two epochs of eclogite metamorphism link 'cold' oceanic subduction and 'hot' continental subduction, the North Qaidam UHP belt, NW China. *Geological Society, London, Special Publications*, *474*, 275–289. https://doi.org/10.1144/SP474.2
Song, S., Zhang, L., Niu, Y., Su, L., Jian, P., & Liu, D. (2005). Geochronology of diamond-bearing zircons from garnet peridotite in the North Qaidam UHPM belt, Northern Tibetan Plateau: A record of complex histories from oceanic lithosphere subduction to continental collision. *Earth and Planetary Science Letters*, *234*(1–2), 99–118.
Song, X.-Y., Zhou, M.-F., Wang, C. Y., Qi, L., & Zhang, C.-J. (2006). Role of crustal contamination in formation of the Jinchuan intrusion and its world-Class Ni-Cu-(PGE) sulfide deposit, Northwest China. *International Geology Review*, *48*(12), 1113–1132. https://doi.org/10.2747/0020-6814.48.12.1113
Stacey, J. S., & Kramers, J. D. (1975). Approximation of terrestrial lead isotope evolution by a two-stage model. *Earth and Planetary Science Letters*, *26*, 207–221.
Stampfli, G. M., & Borel, G. D. (2002). A plate tectonic model for the Paleozoic and Mesozoic constrained by dynamic plate boundaries and restored synthetic oceanic isochrons. *Earth and Planetary Science Letters*, *196*, 17–33.
Sun, J. F., Yang, J. H., Wu, F. Y., & Wilde, S. A. (2012). Precambrian crustal evolution of the eastern North China craton as revealed by U-Pb ages and Hf isotopes of detrital zircons from the Proterozoic Jing'eryu Formation. *Precambrian Research*, *200*, 184–208.
Sun, J. P., Dong, Y. P., Ma, L. C., Peng, Y., Chen, S. Y., Du, J. J., & Jiang, W. (2019). Late Paleoproterozoic tectonic evolution of the Olongbuluke Terrane, northern Qaidam, China: Constraints from stratigraphy and detrital zircon geochronology. *Precambrian Research*, *331*, 105349. https://doi.org/10.1016/j.precamres.2019.105349
Sun, S. S., & McDonough, W. F. (1989). Chemical and isotopic systematics of oceanic basalts: Implications for mantle composition and processes. *Geological Society, London, Special Publications*, *42*(1), 313–345. https://doi.org/10.1144/gsl.sp.1989.042.01.19
Tang, Q., Li, C., Zhang, M., Ripley, E. M., & Wang, Q. (2014). Detrital zircon constraint on the timing of amalgamation between Alxa and Ordos, with exploration implications for Jinchuan-type Ni–Cu ore deposit in China. *Precambrian Research*, *255*, 748–755.
Tang, Z. L., & Bai, Y. L. (2000). The geotectonic setting of the large and superlange mineral deposits in the southwest margin of NorthChina Paleoplate. *Acta Geologica Gansu*, *9*(1), 1–14 (in Chinese with English Abstract).
Teng, X., Zhang, J., Mao, X., Lu, Z., & Zhou, G. (2020). The earliest Cambrian UHT metamorphism in the Qaidam block, western China: A record of the final assembly of Greater Gondwana? *Gondwana Research*, *87*, 118–137.
Trap, P., Faure, M., Lin, W., & Monié, P. (2007). Late paleoproterozoic (1900–1800Ma) nappe stacking and polyphase deformation in the Hengshan–Wutaishan area: Implications for the understanding of the Trans-North-China belt, North China Craton. *Precambrian Research*, *156*(1–2), 85–106. https://doi.org/10.1016/j.precamres.2007.03.001
Tseng, C.-Y., Yang, H.-Y., Yusheng, W., Dunyi, L., Wen, D.-J., Lin, T.-C., & Tung, K.-A. (2006). Finding of Neoproterozoic (~775 Ma) magmatism recorded in metamorphic complexes from the North Qilian orogen: Evidence from SHRIMP zircon U-Pb dating. *Chinese Science Bulletin*, *51*(8), 963–970. https://doi.org/10.1007/s11434-006-0963-1
Tung, K., Yang, H.-J., Yang, H.-Y., Liu, D., Zhang, J., Wan, Y., & Tseng, C.-Y. (2007). SHRIMP U-Pb geochronology of the zircons from the Precambrian basement of the Qilian Block and its geological significances. *Chinese Science Bulletin*, *52*(19), 2687–2701. https://doi.org/10.1007/s11434-007-0356-0
Tung, K. A., Yang, H. Y., Liu, D. Y., Zhang, J. X., Yang, H. J., Shau, Y. H., & Tseng, C. Y. (2012). The amphibolitefacies metamorphosed mafic rocks from the Maxianshan area, Qilian block, NW China: A record of early Neoproterozoic arc magmatism. *Journal of Asian Earth Sciences*, *46*, 177–189. https://doi.org/10.1016/j.jseaes.2011.12.006
Tung, K.-A., Yang, H.-Y., Liu, D.-Y., Zhang, J.-X., Yang, H.-J., Shau, Y.-H., & Tseng, C.-Y. (2013). The Neoproterozoic granitoids from the Qilian block, NW China: Evidence for a link between the Qilian and South China blocks. *Precambrian Research*, *235*, 163–189. https://doi.org/10.1016/j.precamres.2013.06.016
Turner, S. A. (2010). Sedimentary record of Late Neoproterozoic rifting in the NW Tarim Basin, China. *Precambrian Research*, *181*(1–4), 85–96. https://doi.org/10.1016/j.precamres.2010.05.015
Turner, S. P., Foden, J. D., & Morrison, R. S. (1992). Derivation of some A-type magmas by fractionation of basaltic magma—An example from the Padthaway Ridge, South Australia. *Lithos*, *28*, 151–179.
Vincent, S. J., & Allen, M. B. (1999). Evolution of the Minle and Chaoshui Basins, China: Implications for Mesozoic strike-slip basin formation in Central Asia. *The Geological Society of America Bulletin*, *111*(5), 725–742. https://doi.org/10.1130/0016-7606(1999)111<0725:EOTMAC>2.3.CO;2
Wan, B., Windley, B. F., Xiao, W., Feng, J., & Zhang, J. (2015). Paleoproterozoic high-pressure metamorphism in the northern North China craton and implications for the Nuna supercontinent. *Nature Communications*, *6*(1), 8344. https://doi.org/10.1038/ncomms9344
Wan, Y., Liu, D., Wang, W., Song, T., Kroner, A., Dong, C., et al. (2011). Provenance of Meso- to Neoproterozoic cover sediments at the Ming tombs, Beijing, North China craton: An integrated study of U-Pb dating and Hf isotopic measurement of detrital zircons and whole-rock geochemistry. *Gondwana Research*, *20*(1), 219–242. https://doi.org/10.1016/j.gr.2011.02.009
Wan, Y., Song, B., Liu, D., Wilde, S. A., Wu, J., Shi, Y., et al., et al. (2006). SHRIMP U-Pb zircon geochronology of Palaeoproterozoic metasedimentary rocks in the North China Craton: Evidence for a major late Palaeoproterozoic tectonothermal event: *Precambrian Research*, *149*, 249–271. https://doi.org/10.1016/j.precamres.2006.06.006
Wang, A. G., Zhang, C. L., & Guo, K. Y. (2004). Depositional types and its tectonic significance of lower member of Nanhuan System in North margin of West Kunlun: *Journal of Stratigraphy*, *28*, 248–256 (in Chinese with English abstract).
Wang, C., Liu, L., Wang, Y. H., He, S. P., Li, R. S., Li, M., et al. (2015). Recognition and tectonic implications of an extensive Neoproterozoic volcanosedimentary rift basin along the southwestern margin of the Tarim Craton, northwestern China. *Precambrian Research*, *257*, 65–82.
Wang, H., Gao, R., Zeng, L., Kuang, Z., Xue, A., Li, W., et al. (2014). Crustal structure and Moho geometry of the northeastern Tibetan plateau as revealed by SinoProbe-02 deep seismic-reflection profiling. *Tectonophysics*, *636*, 32–39. https://doi.org/10.1016/j.tecto.2014.08.010

Wang, H. C., Xiu, Q. Y., & Yuan, G. B. (1999). Metamorphic evolution of paleoproterozoic Erdaowa Group in North Hohhot, Inner Mongolia. *Progress in Precambrian Research*, *22*, 39–49 (in Chinese with English abstract).

Wang, J. P., Kusky, T., Wang, L., Polat, A., Deng, H., Wang, C., & Wang, S. (2017). Structural relationships along a Neoarchean arc-continent collision zone, North China craton. *The Geological Society of America Bulletin*, *129*(1–2), 59–75. https://doi.org/10.1130/b31479.1

Wang, J. P., Li, X. W., Ning, W. B., Kusky, T. M., Wang, L., Polat, A., & Deng, H. (2019). Geology of a Neoarchean suture: Evidence from the Zunhua ophiolitic melange of the Eastern Hebei province, North China Craton. *The Geological Society of America Bulletin*, *131*(11/12), 1943–1964. https://doi.org/10.1130/B35138.1

Wang, Q., Chen, N., Li, X., Hao, S., & Chen, H. (2008). LA-ICPMS zircon U-Pb geochronological constraints on the tectonothermal evolution of the early Paleoproterozoic Dakendaban Group in the Quanji Block, NW China. *Chinese Science Bulletin*, *53*, 2849–2858.

Wang, Q., Pan, Y., Chen, N., Li, X., & Chen, H. (2009). Proterozoic polymetamorphism in the Quanji Block, northwestern China: Evidence from microtextures, garnet compositions and monazite CHIME ages. *Journal of Asian Earth Sciences*, *34*, 686–698. https://doi.org/10.1016/j.jseaes.2008.10.008

Wang, Q., Yang, D., & Xu, W. (2012). Neoproterozoic basic magmatism in the southeast margin of North China Craton: Evidence from whole-rock geochemistry, U-Pb and Hf isotopic study of zircons from diabase swarms in the Xuzhou-Huaibei area of China. *Science China Earth Sciences*, *55*, 1461–1479. https://doi.org/10.1007/s11430-011-4237-7

Wang, X. L., Jiang, S. Y., Dai, B. Z., Griffin, W. L., Dai, M. N., & Yang, Y. H. (2011). Age, geochemistry and tectonic setting of the Neoproterozoic (ca 830 Ma) gabbros on the southern margin of the North China Craton. *Precambrian Research*, *190*, 35–47. https://doi.org/10.1016/j.precamres.2011.08.004

Wang, Z. Z., Chen, X. H., Shao, Z. G., Li, B., Ding, W. C., Zhang, Y. P., et al. (2020). Petrogenesis of the late Silurian-early Devonian granites in the Longshoushan-Helishan area, Gansu province, and its tectonic implications for the early Paleozoic evolution of the southwestern Alxa block. *Acta Geologica Sinica*, *94*(8), 2243–2261 (in Chinese with English Abstract).

Wen, B., Evans, D. A. D., & Li, Y. X. (2017). Neoproterozoic paleogeography of the Tarim Block: An extended or alternative "missing-link" model for Rodinia? *Earth and Planetary Science Letters*, *458*, 92–106.

Wen, B., Evans, D. A. D., Wang, C., Li, Y. X., & Jing, X. Q. (2018). A positive test for the Greater Tarim Block at the heart of Rodinia: Mega-dextral suturing of supercontinent assembly. *Geology*, *46*(8), 687–690.

Whalen, J. B., Currie, K. L., & Chappell, B. W. (1987). A-type granites: Geochemical characteristics, discrimination and petrogenesis. *Contributions to Mineralogy and Petrology*, *95*, 407–419.

Wiedenbeck, M., Alle, P., Corfu, F., Griffin, W. L., Meier, M., Oberli, F., et al. (1995). Three natural zircon standards for U-Th-Pb, Lu-Hf, trace element and REE analyses. *Geostandards Newsletter*, *19*(1), 1–23. https://doi.org/10.1111/j.1751-908X.1995.tb00147.x

Wu, C., Liu, C. F., Fan, S. F., Zuza, A. V., Ding, L., Liu, W. C., et al. (2020). Structural analysis and tectonic evolution of the western domain of the Eastern Kunlun Range, northwest Tibet. *GSA Bulletin*, *132*(5/6), 1291–1315. https://doi.org/10.1130/B35388.1

Wu, C., Liu, C. F., Zhu, Y., Zhou, Z. G., Jiang, T., Liu, W. C., et al. (2016). Early Paleozoic magmatic history of central Inner Mongolia, China: Implications for the tectonic evolution of the Southeast Central Asian Orogenic belt. *International Journal of Earth Sciences*, *105*(5), 1307–1327.

Wu, C., Yin, A., Zuza, A. V., Zhang, J., Liu, W., & Ding, L. (2016). Pre-Cenozoic geologic history of the central and northern Tibetan Plateau and the role of Wilson cycles in constructing the Tethyan orogenic system. *Lithosphere*, *8*(3), 254–292. https://doi.org/10.1130/l494.1

Wu, C., Zhou, Z., Zuza, A. V., Wang, G., Liu, C., & Jiang, T. (2018). A 1.9-Ga mélange along the Northern margin of the north China craton: Implications for the assembly of Columbia supercontinent. *Tectonics*, *37*(10), 3610–3646. https://doi.org/10.1029/2018tc005103

Wu, C., Zuza, A. V., Chen, X. H., Ding, L., Levy, D. A., Liu, C. F., et al. (2019). Tectonics of the eastern Kunlun range: Cenozoic reactivation of a Paleozoic–early Mesozoic orogen. *Tectonics*, *38*(5), 1609–1650.

Wu, C., Zuza, A. V., Yin, A., Liu, C., Reith, R. C., Zhang, J., et al. (2017). Geochronology and geochemistry of Neoproterozoic granitoids in the central Qilian Shan of northern Tibet: Reconstructing the amalgamation processes and tectonic history of Asia. *Lithosphere*, *L640*, 641. https://doi.org/10.1130/l640.1

Wu, C., Zuza, A. V., Zhou, Z. G., Yin, A., McRivette, M. W., Chen, X. H., et al. (2019). Mesozoic–Cenozoic evolution of the eastern Kunlun range, central Tibet, and implications for basin evolution within the Indo-Asian collision. *Lithosphere*, *11*(4), 524–550.

Wu, C. Z., Santosh, M., Chen, Y. J., Samson, I. M., Lei, R. X., Dong, L. H., et al. (2014). Geochronology and geochemistry of Early Mesoproterozoic meta-diabase sills from Quruqtagh in the northeastern Tarim Craton: Implications for breakup of the Columbia supercontinent. *Precambrian Research*, *241*, 29–43.

Xiao, L.-L., Wu, C.-M., Zhao, G.-C., Guo, J.-H., & Ren, L.-D. (2011). Metamorphic P–T paths of the Zanhuang amphibolites and metapelites: Constraints on the tectonic evolution of the paleoproterozoic Trans-North China Orogen. *International Journal of Earth Sciences*, *100*(4), 717–739. https://doi.org/10.1007/s00531-010-0522-5

Xiao, S., Shen, B., Tang, Q., Kaufman, A. J., Yuan, X., Li, J., & Qian, M. (2014). Biostratigraphic and chemostratigraphic constraints on the age of early Neoproterozoic carbonate successions in North China. *Precambrian Research*, *246*, 208–225. https://doi.org/10.1016/j.precamres.2014.03.004

Xiao, W., Windley, B. F., Hao, J., & Zhai, M. (2003). Accretion leading to collision and the Permian Solonker suture, Inner Mongolia, China: Termination of the central Asian orogenic belt. *Tectonics*, *22*(6), 1069. https://doi.org/10.1029/2002tc001484

Xiao, W., Windley, B. F., Yong, Y., Yan, Z., Yuan, C., Liu, C., & Li, J. (2009). Early Paleozoic to Devonian multiple-accretionary model for the Qilian Shan, NW China. *Journal of Asian Earth Sciences*, *35*, 323–333. https://doi.org/10.1016/j.jseaes.2008.10.001

Xiao, W. J., Windley, B. F., Huang, B. C., Han, C. M., Yuan, C., Chen, H. L., & Li, J. L. (2009). End-permian to mid-Triassic termination of the accretionary processes of the southern Altaids: Implications for the geodynamic evolution, Phanerozoic continental growth, and metallogeny of central Asia. *International Journal of Earth Sciences*, *98*(6), 1189–1217. https://doi.org/10.1007/s00531-008-0407-z

Xiao, W. J., Windley, B. F., Liu, D. Y., Jian, P., Liu, C. Z., Yuan, C., & Sun, M. (2005). Accretionary tectonics of the western Kunlun Orogen, China: A Paleozoic–early Mesozoic, long-lived active continental margin with implications for the growth of southern Eurasia. *The Journal of Geology*, *113*, 687–705. https://doi.org/10.1086/449326

Xiao, W. J., Windley, B. F., Yuan, C., Sun, M., Han, C. M., Lin, S. F., et al. (2009). Paleozoic multiple subduction-accretion processes of the southern Altaids. *American Journal of Science*, *309*, 221–270. https://doi.org/10.2475/03.2009.02

Xu, X., Song, S., Su, L., Li, Z., Niu, Y., & Allen, M. B. (2015). The 600–580 Ma continental rift basalts in north Qilian Shan, northwest China: Links between the Qilian-Qaidam block and SE Australia, and the reconstruction of east Gondwana. *Precambrian Research*, *257*, 47–64. https://doi.org/10.1016/j.precamres.2014.11.017

Xu, Z. Q., He, B. Z., Zhang, C. L., Zhang, J. X., Wang, Z. M., & Cai, Z. H. (2013). Tectonic framework and crustal evolution of the Precambrian basement of the Tarim block in NW China: New geochronological evidence from deep drilling samples. *Precambrian Research*, *235*, 150–162.

Yan, Z., Fu, C., Aitchison, J. C., Buckman, S., Niu, M., Cao, B., et al. (2019). Retro-foreland basin in the NE Tibet plateau. *Tectonics*, *38*. https://doi.org/10.1029/2019TC005560

Yang, H., Wu, G., Kusky, T. M., Chen, Y., & Xiao, Y. (2018). Paleoproterozoic assembly of the North and South Tarim terranes: New insights from deep seismic profiles and Precambrian granite cores. *Precambrian Research*, *305*, 151–165.

Yang, J. S., Xu, Z. Q., Zhang, J. X., Chu, C. Y., Zhang, R., & Liou, J. G. (2001). Tectonic significance of early Paleozoic high-pressure rocks in Altun-Qaidam-Qilian Mountains, northwest China. In M. S. Hendrix & G. A. Davis (Eds.), *Paleozoic and Mesozoic Tectonic Evolution of Central Asia: From Continental Assembly to Intracontinental Deformation: Geological Society of America Memoir* (Vol. 194 pp. 151–170). https://doi.org/10.1130/0-8137-1194-0.151

Yang, P., Wu, G., Ren, Z., Zhou, R., Zhao, J., & Zhang, L. (2020). Tectono-thermal evolution of Cambrian–Ordovician source rocks and implications for hydrocarbon generation in the eastern Tarim Basin, NW China. *Journal of Asian Earth Sciences*, 104267. https://doi.org/10.1016/j.jseaes.2020.104267

Ye, X. T., Zhang, C. L., Santosh, M., Zhang, J., Fan, X. K., & Zhang, J. J. (2016). Growth and evolution of Precambrian continental crust in the southwestern Tarim terrane: New evidence from the ca. 1.4 Ga A-type granites and Paleoproterozoic intrusive complex. *Precambrian Research*, *275*, 18–34. https://doi.org/10.1016/j.precamres.2015.12.017

Yin, A., Brandl, G., & Kröner, A. (2020). Plate-tectonic processes at ca. 2.0 Ga: Evidence from >600 km of plate convergence. *Geology*, *48*, 103–107.

Yin, A., Dang, Y., Zhang, M., McRivette, M. W., Burgess, W. P., & Chen, X. (2007). Cenozoic tectonic evolution of Qaidam basin and its surrounding regions (part 2): Wedge tectonics in southern Qaidam basin and the Eastern Kunlun Range. *433*, 369–390. https://doi.org/10.1130/2007.2433(18)

Yin, A., Dang, Y.-Q., Wang, L.-C., Jiang, W.-M., Zhou, S.-P., Chen, X.-H., et al. (2008a). Cenozoic tectonic evolution of Qaidam basin and its surrounding regions (Part 1): The southern Qilian Shan-Nan Shan thrust belt and northern Qaidam basin. *Geological Society of America Bulletin*, *120*(7–8), 813–846. https://doi.org/10.1130/B26180.1

Yin, A., Dang, Y. Q., Zhang, M., Chen, X. H., & McRivette, M. W. (2008b). Cenozoic tectonic evolution of the Qaidam basin and its surrounding regions (Part 3): Structural geology, sedimentation, and regional tectonic reconstruction. *Geological Society of America Bulletin*, *120*(7–8), 847–876. https://doi.org/10.1130/b26232.1

Yin, A., & Harrison, T. M. (2000). Geologic evolution of the Himalayan-Tibetan orogen. *Annual Review of Earth and Planetary Sciences*, *28*, 211–280.

Yin, A., Manning, C. E., Lovera, O., Menold, C. A., Chen, X., & Gehrels, G. E. (2007). Early Paleozoic tectonic and thermomechanical evolution of ultrahigh-pressure (UHP) metamorphic rocks in the Northern Tibetan Plateau, Northwest China. *International Geology Review*, *49*(8), 681–716. https://doi.org/10.2747/0020-6814.49.8.681

Yin, A., & Nie, S. (1996). A Phanerozoic palinspastic reconstruction of China and its neighboring regions. In A. Yin, & T. M. Harrison (Eds.), *The tectonic evolution of Asia* (pp. 442–485). New York, NY: Cambridge University Press.

Yu, S. Y., Li, S. Z., Zhang, J. X., Peng, Y. B., Somerville, I., Liu, Y. J., et al. (2019). Multistage anatexis during tectonic evolution from oceanic subduction to continental collision: A review of the North Qaidam UHP belt, NW China. *Earth-Science Reviews*, *191*, 190–211. https://doi.org/10.1016/j.earscirev.2019.02.016

Yu, S. Y., Zhang, J. X., Real, P. G. D., Zhao, X. L., Hou, K. J., Gong, J. H., & Li, Y. S. (2013). The Grenvillian orogeny in the Altun–Qilian–North Qaidam mountain belts of northern Tibet Plateau: Constraints from geochemical and zircon U–Pb age and Hf isotopic study of magmatic rocks. *Journal of Asian Earth Sciences*, *73*, 372–395. https://doi.org/10.1016/j.jseaes.2013.04.042

Yu, X., Fu, S., Wang, Z., Li, Q., & Guo, Z. (2017). The discovery of early Paleoproterozoic high-Na trondhjemite in the northeastern Qaidam basin: Evidence from the drilling core samples. *Precambrian Research*, *298*, 615–628. https://doi.org/10.1016/j.precamres.2017.04.002

Zeh, A., Gerdes, A., Barton, J., & Klemd, R. (2010). U-Th-Pb and Lu-Hf systematics of zircons from TTG's, leucosomes, meta-anorthosite and quartzites of the Limpopo Belt (South Africa): Constraints for the formation, recycling and metamorphism of Paleoarchaean crust. *Precambrian Research*, *179*, 50–68.

Zhang, C. L., Li, Z. X., Li, X. H., Ye, H., Wang, A., & Guo, K. Y. (2006). Neoproterozoic bimodal intrusive complex in the southwestern Tarim Block, northwest China: Age, geochemistry, and implications for the rifting of Rodinia. *International Geology Review*, *48*, 112–128. https://doi.org/10.2747/0020-6814.48.2.112

Zhang, C. L., Ye, X. T., Zou, H. B., & Chen, X. Y. (2016). Neoproterozoic sedimentary basin evolution in southwestern Tarim, NW China: New evidence from field observations, detrital zircon U-Pb ages and Hf isotope compositions. *Precambrian Research*, *280*, 31–45. https://doi.org/10.1016/j.precamres.2016.04.011

Zhang, F. Q., Dilek, Y., Cheng, X. G., Wu, H. X., Lin, X. B., & Chen, H. L. (2019a). Late Neoproterozoic–early Paleozoic seismic structure–stratigraphy of the SW Tarim Block (China), its passive margin evolution and the Tarim–Rodinia breakup. *Precambrian Research*, *334*, 105456. https://doi.org/10.1016/j.precamres.2019.105456

Zhang, H. F., Zhou, Z. G., Liu, W. C., Li, Z. Z., Zhang, Y. M., & Liu, C. F. (2009). Grenvill tectono-thermal event record in the Bainaimiao area, Inner Mongolia, China: Evidence from zircon LA-ICP-MS U-Pb dating of quart monzodiorite dike. *Acta Petrologica Sinica*, *25*(6), 1512–1518.

Zhang, K. J. (1997). North and South China collision along the eastern and southern North China margins. *Tectonophysics*, *270*, 145–156. https://doi.org/10.1016/S0040-1951(96)00208-9

Zhang, J. X., Gong, J. H., Yu, S. Y., Li, H. K., & Hou, K. J. (2013). Neoarchean–Paleoproterozoic multiple tectonothermal events in the western Alxa block, North China Craton and their geological implication: Evidence from zircon U–Pb ages and Hf isotopic composition. *Precambrian Research*, *235*, 36–57.

Zhang, J. X., Mattinson, C. G., Meng, F. C., Wan, Y. S., & Tung, K. (2008). Polyphase tectonothermal history recorded in granulitized gneisses from the North Qaidam HP/UHP metamorphic terrane, western China: Evidence from zircon U-Pb geochronology. *The Geological Society of America Bulletin*, *120*(5–6), 732–749.

Zhang, J. X., Mattinson, C., Yu, S., Li, Y., Yu, X., Mao, X., & Peng, Y. (2019). Two contrasting accretion v. collision orogenies: Insights from Early Paleozoic polyphase metamorphism in the Altun–Qilian–North Qaidam orogenic system, NW China. *Geological Society, London, Special Publications*, *474*(1), 153–181.

Zhang, J. X., Yang, J. S., Mattinson, C. G., Xu, Z. Q., Meng, F. C., & Shi, R. D. (2005). Two contrasting eclogite cooling histories, North Qaidam HP/UHP terrane, western China: Petrological and isotopic constraints. *Lithos*, *84*(1–2), 51–76.

Zhang, L., Wang, Q., Chen, N., Sun, M., Santosh, M., & Ba, J. (2014). Geochemistry and detrital zircon U-Pb and Hf isotopes of the paragneiss suite from the Quanji massif, SE Tarim Craton: Implications for Paleoproterozoic tectonics in NW China. *Journal of Asian Earth Sciences*, *95*, 33–50. https://doi.org/10.1016/j.jseaes.2014.05.014

Zhang, M., Kamo, S. L., Li, C., Hu, P., & Ripley, E. M. (2010). Precise U–Pb zircon–baddeleyite age of the Jinchuan sulfide ore-bearing ultramafic intrusion, western China. *Mineralium Deposita*, *45*(1), 3–9. https://doi.org/10.1007/s00126-009-0259-x

Zhao, G. (2009). Metamorphic evolution of major tectonic units in the basement of the North China Craton: Key issues and discussion. *Yanshi Xuebao*, *25*, 1772–1792 (in Chinese with English Abstract).

Zhao, G. C., & Cawood, P. A. (2012). Precambrian geology of China. *Precambrian Research*, *222–223*, 13–54.

Zhao, G. C., Cawood, P. A., Wilde, S. A., & Sun, M. (2002). Review of the global 2.1–1.8 Ga orogens: Implications for a pre-Rodinian supercontinent. *Earth-Science Reviews*, *59*(1–4), 125–162.

Zhao, G. C., Sun, M., Wilde, S. A., & Sanzhong, L. (2005). Late Archean to Paleoproterozoic evolution of the North China Craton: Key issues revisited. *Precambrian Research*, *136*(2), 177–202.

Zhao, G. C., Wang, Y., Huang, B., Dong, Y., Li, S., Zhang, G., & Yu, S. (2018). Geological reconstructions of the East Asian blocks: From the breakup of Rodinia to the assembly of Pangea. *Earth-Science Reviews*, *186*, 262–286.

Zhao, G. C., Wilde, S. A., Cawood, P. A., & Sun, M. (2001). Archean blocks and their boundaries in the North China Craton: Lithological, geochemical, structural and P-T path constraints and tectonic evolution. *Precambrian Research*, *107*, 45–73.

Zhao, G. C., Wilde, S. A., Sun, M., Guo, J. H., Kröner, A., Li, S. Z., et al. (2008). SHRIMP U–Pb zircon geochronology of the Huaian complex: Constraints on late Archean to paleoproterozoic crustal accretion and collision of the Trans-north China orogen. *American Journal of Science*, *308*, 270–303.

Zhao, R. F., Guo, J. H., Peng, P., & Liu, F. (2011). 2.1 Ga crustal remelting event in Hengshan complex: Evidence from zircon U–Pb dating and Hf–Nd isotopic study on potassic granites. *Acta Petrologica Sinica*, *27*, 1607–1623 (in Chinese with English abstract).

Zhao, X. X., & Coe, R. S. (1987). Paleomagnetic constraints on the collision and rotation of North and South China. *Nature*, *327*, 141–144.

Zheng, B., Zhu, W., Jahn, B. M., Shu, L., Zhang, Z., & Su, J. (2010). Subducted Precambrian oceanic crust: Geochemical and Sr-Nd isotopic evidence from metabasalts of the Aksu blueschist, NW China. *Journal of the Geological Society [London]*, *167*, 1161–1170. https://doi.org/10.1144/0016-76492010-001

Zhou, Z., Hu, M., Wu, C., Wang, G., Liu, C., Cai, A., & Jiang, T. (2018). Coupled U–Pb dating and Hf isotopic analysis of detrital zircons from Bayan Obo Group in Inner Mongolia: Constraints on the evolution of the Bayan Obo rift belt. *Geological Journal*, *53*, 2649–2664. https://doi.org/10.1002/gj.3102

Zhu, W., Zheng, B., Shu, L., Ma, D., Wu, H., Li, Y., et al. (2011). Neoproterozoic tectonic evolution of the Precambrian Aksu blueschist terrane, northwestern Tarim, China: Insights from LA-ICP-MS zircon U-Pb ages and geochemical data. *Precambrian Research*, *185*, 215–230. https://doi.org/10.1016/j.precamres.2011.01.012

Zuza, A. V., Cheng, X., & Yin, A. (2016). Testing models of Tibetan Plateau formation with Cenozoic shortening estimates across the Qilian Shan–Nan Shan thrust belt. *Geosphere*, *12*(2), 501–532. https://doi.org/10.1130/GES01254.1

Zuza, A. V., Wu, C., Reith, R. C., Yin, A., Li, J. H., Zhang, J. Y., et al. (2018). Tectonic evolution of the Qilian Shan: An early Paleozoic orogen reactivated in the Cenozoic. *Geological Society of America Bulletin*, *130*(5–6), 881–925. https://doi.org/10.1130/B31721.1

Zuza, A. V., Wu, C., Wang, Z., Levy, D. A., Li, B., Xiong, X., & Chen, X. (2019). Underthrusting and duplexing beneath the northern Tibetan Plateau and the evolution of the Himalayan–Tibetan orogen. *Lithosphere*, *11*(2), 209–231.

Zuza, A. V., & Yin, A. (2013). Testing the TWINS hypothesis: Were Greater North China and Western Laurentia linked in the Archean and Proterozoic? *Geological Society of America Abstracts with Programs*, *45*(7), 463.

Zuza, A. V., & Yin, A. (2017). Balkatach hypothesis: A new model for the evolution of the Pacific, Tethyan, and Paleo-Asian oceanic domains. *Geosphere*, *13*(5), 1664–1712. https://doi.org/10.1130/ges01463.1